A PATH TOWARD AN EFFECTIVE SCALING APPROACH FOR AXIAL PISTON MACHINES

A Dissertation

Submitted to the Faculty

of

Purdue University

by

Lizhi Shang

In Partial Fulfillment of the

Requirements for the Degree

of

Doctor of Philosophy

December 2018

Purdue University

West Lafayette, Indiana

THE PURDUE UNIVERSITY GRADUATE SCHOOL
STATEMENT OF DISSERTATION APPROVAL

Dr. Monika Ivantysynova, Chair

Department of Agricultural and Biological Engineering

Dr. Andrea Vacca, Chair

Department of Agricultural and Biological Engineering

Dr. Farshid Sadeghi

School of Mechanical Engineering

Dr. John Lumkes

Department of Agricultural and Biological Engineering

Dr. Sadegh Dabiri

Department of Agricultural and Biological Engineering

Approved by:

Dr. Bernard Engel

Head of the School Graduate Program

To Glorify God.

ACKNOWLEDGMENTS

I would like to first thank my major professor Dr. Monika Ivantysynova, who gave me the opportunity as being a graduate student at Maha fluid power research center, who provided me guidance and financial support through the time I pursue my Ph.D. degree, who encouraged me through her own hardworking and dedication, who inspired me by demonstrating how the world can be changed through research and education. I also would like to thank Dr. Andrea Vacca who provided necessary advice toward my Ph.D. thesis and defense.

I also want to thank my colleges who had work with me. I want to thank Dan Mizell, and Ashley Busquets, and Shanmukh Sarode, who were working on the piston/cylinder interface with me. I want to thank Jeremy Beale and Ashkan Darbani who were working on the slipper/swashplate interface with me. I want to thank Swarnava Mukherjee who was working on the cylinder block/valve plate interface with me. I want to thank Paul Kalbfleisch, Meike Ernst, and Rene Chacon who were working late with me.

The person who I must thank the most is my wife Fazhi, who trusts and supports me, loves me and forgives me. Fazhi, thank you for embarking on this exciting adventure with me.

TABLE OF CONTENTS

Page

Page

LIST OF TABLES

LIST OF FIGURES

Figure Page

Figure Page

Figure Page

Figure Page

Figure Page

Figure Page

Figure Page

SYMBOLS

A	area
b	width
$\mathbf{C}$	constitutive matrix
c_p	heat capacity
d	diameter
E	elastic modulus
F	force
F_{aK}	axial inertia force
F_B	external force on block
F_{DB}	displacement chamber pressure force on block
F_{DK}	displacement chamber pressure force on piston
F_G	slipper axial load
F_{HD}	slipper hold down force
F_K	piston external force
F_{KB}	force from piston to cylinder block
F_{RK}	total resultant force from slipper
F_{SB}	reaction force on block
F_{SK}	reaction force on piston
F_{TB}	piston axial friction on block
F_{TG}	slipper friction
F_{TK}	piston axial friction
$F_{\omega G}$	slipper centrifugal force
$F_{\omega K}$	piston-slipper assembly centrifugal force
H	enthalpy

H_K	piston maximum stroke
h	specific enthalpy
h_g	gap height
l	length
l_G	distance from slipper running surface to ball joint center
l_{SG}	distance from slipper COM to ball joint center
M_B	external moment on block
M_{DB}	moment due to displacement chamber pressure force on block
M_G	slipper external moment
M_K	piston external moment
M_{KB}	moment from piston to cylinder block
M_{SB}	reaction moment on block
M_{TB}	moment due to piston axial friction on block
$M_{\omega G}$	moment due to slipper centrifugal force
$\dot{m}$	mass flow rate
m	mass
$\mathbf{M}$	heat transfer matrix
n	rotational speed
P	power
p	pressure
Q	volumetric flow rate
q	heat flux
$\dot{q}$	rate of heat flux
$\mathbf{q}$	vector of heat flux
S	entropy
s_K	piston stroke
s	specific entropy
T	temperature
t	time

$\mathbf{T}$	vector of temperature
U	strain energy
V	volume
$\mathbf{u}$	nodal displacement
V_{NF}	applied load potential energy
v	velocity
$\mathbf{V}$	velocity vector
v_{fluid}	specific volume
w	normal velocity
wt	weighting factor
β	swashplate angle
Γ	diffusion coefficient
ϵ	strain
κ	heat transfer coefficient
λ	linear scaling factor
μ	viscosity
ν	Poisson's ratio
Π	potential energy
ρ	viscosity
σ	stress
Φ_D	dissipation
ϕ	shaft angle
ω	shaft speed

ABBREVIATIONS

avg	average
B	block
b	bottom surface
DC	displacement chamber
E	east neighbor cell
e	east cell wall
EHD	elasto-hydrodynamic
FVM	finite volume method
G	slipper
IDC	inner dead center
K	piston
N	north neighbor cell
n	north cell wall
ODC	outer dead center
S	south neighbor cell
s	south cell wall
t	top surface
W	west neighbor cell
w	west cell wall
0	original size

ABSTRACT

Shang, Lizhi Ph.D., Purdue University, December 2018. A Path Toward an Effective Scaling Approach for Axial Piston Machines. Major Professor: Monika Ivantysynova.

Lacking reliable scaling rules, hydraulic pump and motor manufactures pay a high monetary and temporal price for attempting to expand their production lines by scaling their existing swashplate type axial piston machines to other sizes. The challenge is that the lubricating interfaces, which are the key elements in determining the performance of a positive displacement machine, namely the piston/cylinder interface, the cylinder block/valve plate interface, and the slipper/swashplate interface, are not easily scalable.

The aim of this work is not to find an effective scaling rule, but rather to propose a path toward an effective scaling approach that allows axial piston machine scaling research to advance; the establishment of this new scaling approach entails developing a multi-physics and multi-domain simulation model for evaluating the performance of the virtually scaled pumps and motors, analyzing the size-dependence of the fundamental physics of the elastohydrodynamic lubricating interfaces, and providing a guide to scaling an axial piston machine to another size with minimum redesign effort while upholding the same energy efficiency and life expectancy.

This work includes a novel swashplate type axial piston machine performance prediction model. This simulation tool is the first of its kind to allow for the virtual scaling of an axial piston pump or motor to a different size, and an examination of its performance that compares the scaled unit against the pre-scaled baseline using a semi-empirical temperature prediction model that negates the need for measured thermal boundaries. The accuracy of the simulation proposed in this work is vastly improved thanks to the next-generation piston/cylinder interface model.

The challenge of scaling an axial piston machine while upholding its efficiency is the size-dependence of the machine performance with regards to significant physical phenomena that describe the behavior of its three most critical lubricating interfaces. The phenomena, including non-isothermal elasto-hydrodynamic effects in the fluid domain, and heat transfer and thermal elastic deflection in the solid domain, is analyzed and explained through fundamental physics in this work. Based on the findings, a guide to scaling swashplate type axial piston machines such as to uphold their efficiency is proposed.

The proposed guideline is applied to a design study focusing on the effective scaling rules for the lubricating interfaces in swashplate type axial piston machine. Different clearances, piston guide lengths, and materials of the piston/cylinder interface are studied for different unit sizes, and a nonlinear clearance scaling method with a groove profile is found effective in maintaining the efficiency of the piston/cylinder interface while scaling the baseline a size eight time larger and a size eight time smaller. The same scaling range is applied to the cylinder block/valve plate interface study and slipper/swashplate interface study. For the cylinder block/valve plate interface, a nonlinear scaling rule for the sealing land dimensions is found to improve the energy efficiency of the scaled interface. Furthermore, it is found that the balance factor in the slipper/swashplate interface, which determines the ratio between the hydrostatic pressure force and the external load, should be scaled nonlinearly in order to achieve the same energy efficiency as the pre-scaled baseline.

1. INTRODUCTION

1.1 Background

Fluid power actuation and driving systems are widely utilized in industrial applications. Thanks to their high power density in comparison to other systems, great compactness of high-performance hydraulic systems is achievable. Among different types of hydrostatic pumps and motors, swashplate type axial piston machines are dominating the market of high pressure applications such as agriculture, construction, forestry, mining, aerospace and manufacturing due to their high operating pressure, variable displacement operation, great efficiency, superior compactness, and good reliability.

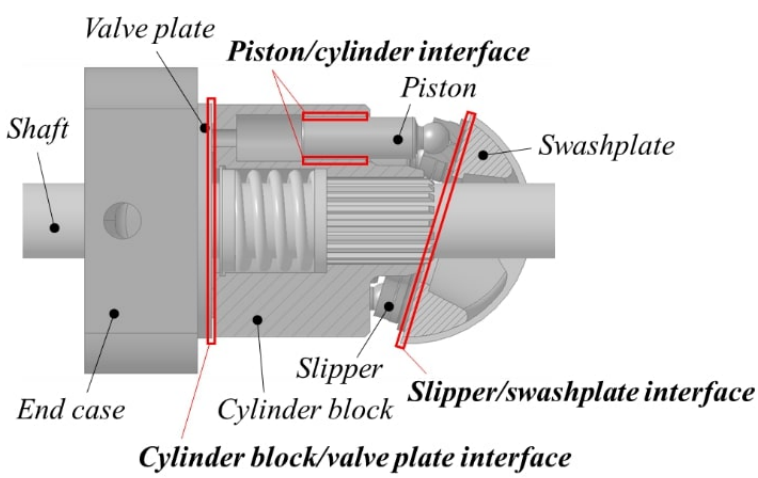

Fig. 1.1. Three lubricating interfaces in swashplate type axial piston machines.

The overall efficiency of a swashplate type axial piston machine is mainly determined by the energy dissipation in three tribological interfaces, shown in Fig. 1.1: namely, the piston/cylinder interface, the cylinder block/valve plate interface, and

the slipper/swashplate interface. The energy dissipation of these three main lubricating interfaces is due to the viscous shear of the working fluid, which takes on two forms.

- The pressure difference across the gap pushes the fluid through the interface, generates fluid shear and energy dissipation following Poiseuille's law. In this way, the energy dissipation has a positive correlation with the gap height as well as with the gap flow rate.

- The relative motion of the solid boundaries forming the lubricating gap causes the fluid to shear, and dissipate energy into heat following Couette's law. In this way, the energy dissipation has a negative correlation with the gap height.

Unfortunately, due to the nature of these two opposing physical phenomena, a design that benefits one can be harmful to the other.

According to Ivantysyn and Ivantysynova [1], the power loss of the lubricating gaps due to these two phenomena in a parallel gap as shown in Fig. 1.2(a) and Fig. 1.2(b), yields:

$$\begin{aligned} P_{Poiseuille} &= \frac{1}{12\mu} \cdot \frac{\Delta p^2}{l} \cdot b \cdot h^3 \\ P_{Couette} &= \mu \cdot \frac{v^2}{h} \cdot b \cdot l \end{aligned} \tag{1.1}$$

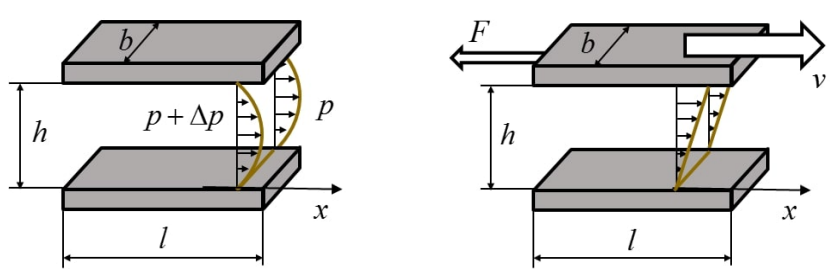

(a) Poiseuille flow in a paralleled gap.

(b) Viscous friction in a paralleled gap.

Fig. 1.2. The two opposing physical phenomena.

They also suggested an optimal gap height for minimizing the total power loss:

$$\frac{d\left(P_{Poiseuille} + P_{Couette}\right)}{dh} = 0 \Rightarrow h_{opt} = \sqrt{\frac{2\mu \cdot v \cdot l}{\Delta p}} \tag{1.2}$$

However, research has shown that the behavior of the lubrication interfaces in swashplate type axial piston machines is far from the behavior of a simple fixed-height parallel gap [2–4]. The gap height in the lubricating interfaces of these pumps and motors is determined by a force balance [5,6], and the elastic deformation and position of the solid bodies bounding the three lubricating interfaces [7,8]. Therefore, the gap height of the lubricating interfaces is not directly controllable through nominal design parameters, but must be determined from a series of complicated fluid-structure and thermal interactions.

Not only are the three interfaces required to fulfill a sealing function they also have a bearing function. The hydrostatic and hydrodynamic pressures generated in the gap have to bear the external load. A design failing to carry the load will result in unfavorable fluid film behavior, extreme gap heights, mixed or solid friction, or even damage to the parts [9].

The force balance between the external loads and the hydrostatic-hydrodynamic pressure field in the lubricating gaps is impossible to alculate analytically due to the complicated motions and the irregular gap shapes caused by elastic deformation. Due to this, properly designing these three lubricating interfaces is a huge challenge, especially when the design process is not supported by computational design tools.

On the system level, from the electro-hydraulic actuator (EHA) system in aviation to the hydraulic shovel system in the mining industry, the size of swashplate type axial piston machines varies from under one cc (cubic centimeter) to over a thousand cc. For manufacturers of hydraulic pumps and motors, this generates a demand for wide production lines spanning vastly different unit sizes. Even though axial piston machines of different sizes share the same working principles, finding rules for scaling an existing pump/motor design to a different size while retaining its efficiency has proven difficult.

1.2 State-of-the-art

Series of pumps and motors that differ in size but share the same design do exist in the axial piston machine categories. Designers and manufacturers found that the maximum shaft speed of pumps and motors of any size is restricted by the maximum viscous shear, which is generated by the relative sliding velocity in the tribological interfaces. Ivantysyn and Ivantysynova [1] suggested the sliding velocity between the cylinder block and the valve plate should be kept between three to five meter per second for any size of pumps and motors.

By maintaining the sliding velocity between the moving parts while scaling, the scaled swashplate type axial piston machine follows the linear scaling rule:

$$\begin{aligned} V(\lambda) &= \lambda^3 \cdot V_o \\ m(\lambda) &= \lambda^3 \cdot m_o \end{aligned} \tag{1.3}$$

where λ is the linear scaling factor. The rotational speed, as mentioned before, scales by the reciprocal of the linear scaling factor λ:

$$n(\lambda) = \lambda^{-1} \cdot n_o \tag{1.4}$$

Via this rule of thumb, well-designed units are often scaled to other sizes in order to extend the market range. However, to achieve the pre-scaled performance in terms of the energy efficiency and the service lifetime, the required trial-and-error design process is both financially and temporally expensive.

In order to understand the size-dependent performance of the swashplate type axial piston machine, a tool that allow for evaluating the efficiency of the pumps and motors is required.

Merritt [10] parameterized the energy efficiency of hydraulic pumps and motors through an empirical model, which uses the operating pressure and operating speed as input variables. However, the coefficients used in his model vary with different unit designs and unit sizes, and are therefore not scalable. The friction and leakage losses of the three major lubricating interfaces of such units were calculated analytically

under the assumption of rigid body and fixed gap height by Manring, Ivantysyn, and Ivantysynova [1, 3, 4, 11, 12]. On the basis of these analyses, their work also suggests an optimal gap height for these interfaces with regards to minimizing losses [1]. However, the scaling rule that was derived from these loss models is limited by its failure to account for fundamental physical phenomena, including the non-isothermal fluid properties, hydrodynamic effects, elastic deformations, heat transfer, and the interactions between all of the above. In order to find a more effective scaling rule for swashplate type axial piston machines, a detailed model is required one that allows for analyzing the performance of the three lubricating interfaces.

The discovery of the thermoelastohydrodynamics of the three lubricating interfaces all starts from the Reynolds equation [13], which was derived from the Navier-Stokes equations and the conservation of mass. Nevertheless, since the kinematics and dynamics of the three lubricating interfaces are different, the modeling researches of the three lubricating interfaces were divided into three branches.

Piston/cylinder interface modeling study starts since van der Kolk [15], who conducted the first numerical fluid pressure distribution simulation in the piston/cylinder gap. The piston/cylinder interface was simplified into a tilt journal bearing in his model. The piston motion was firstly considered in the pressure distribution calculation by Yamaguchi [16]. Ivantysynova [17] firstly introduced a non-isothermal fluid model for the piston/cylinder interface. She coupled the Reynolds equation with the energy equation, to calculate the temperature field in the piston/cylinder interface according to energy dissipation from viscous shear. The fluid viscosity in her model is a function of pressure and temperature. Fang and Shirahashi [18] firstly presented a methodology to determine the piston position inside of the cylinder bore by looking for a position that fulfills the equilibrium between the fluid pressure force and the external load. Olem [19] proposed an iterative method to solve the piston micro motion, which allows the external load to be balanced by the fluid film considering the additional hydrodynamic pressure force from the piston micro motion. The first elastohydrodynamic gap flow simulation for the piston/cylinder interface was proposed

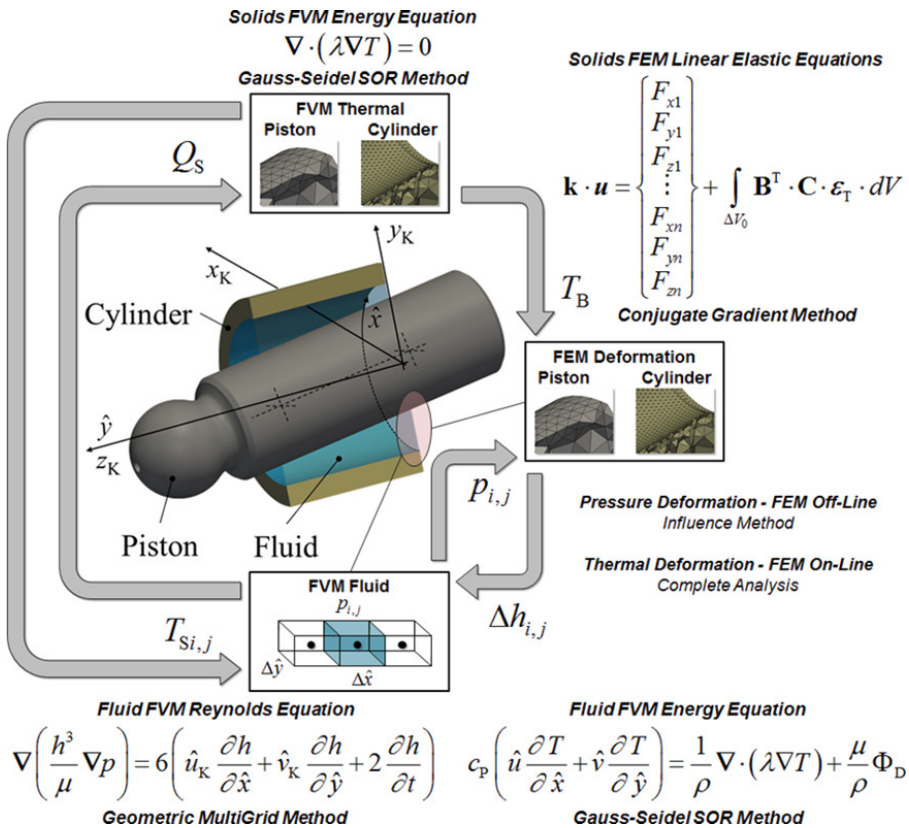

Fig. 1.3. The piston/cylinder fluid-structure and thermal fully coupled model [14].

by Ivantysynova and Huang [20]. They used an influence matrix method to calculate the solid bodies deformation due to the pressure load. The resulting deformation then was included in the gap height. Pelosi and Ivantysynova [21], and Pelosi [22] develop a fluid-structure and thermal interaction model for the piston/cylinder interface as shown in Fig. 1.3, Their model couples the fluid pressure and temperature distribution calculation with the elastic deformation of the piston and the cylinder block under both the pressure and the thermal load, and a three-dimensional solid body heat transfer model.

The modeling study of the cylinder block/valve plate is started by Franco [6], who derived the pressure distribution in the lubricating gap between the cylinder block and the valve plate using an analytical hydrostatic theory. His model assumes a constant and uniform gap height between the cylinder block and the valve plate. The

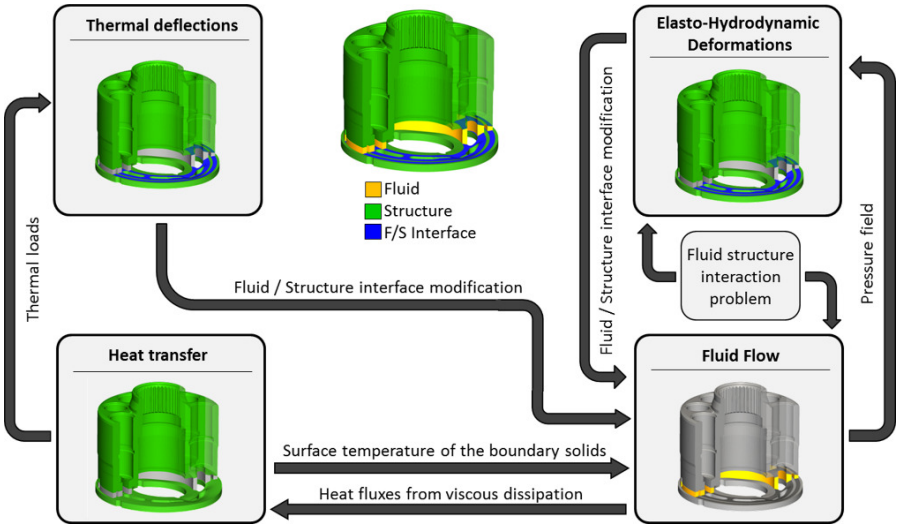

Fig. 1.4. The cylinder block/valve plate interface fluid-structure and thermal fully coupled model [23].

hydrodynamic effect was neglected in his model. After few decades, Wieczorek and Ivantysynova [24] firstly proposed a methodology to solve the micromotion and the position (tilting and lifting) of the cylinder block that fulfills the equilibrium between the external loads and the gap pressure force. The gap pressure force is calculated considering both the hydrostatic and the hydrodynamic effects. The micromotion of the cylinder block further adjusts the hydrodynamic element of the gap fluid pressure distribution. The elastohydrodynamic model of cylinder block/valve plate interface was firstly modeled by Huang and Ivantysynova [25]. Similarly to the piston/cylinder interface, the elastic deformation due to the pressure was solved off-line using an influence matrix method. The elastohydrodynamic solution then solved through an iterative way. Most recently, a multi-domain numerical model for the cylinder block/valve plate interface was developed by Zecchi and Ivantysynova [26] [27] and Zecchi [23]. In their model, the fluid behavior was calculated based on the boundary conditions from the solid domain such as the surface deformation and the surface temperature. The surface deformation was calculated based on not only the pressure load but also the thermal load. The thermal load (solid body temperature distribution) and the

surface temperature were solved through a three-dimensional heat transfer model. As shown in Fig. 1.4, their model solves the fluid-structure and thermal interaction problem in iterative scheme.

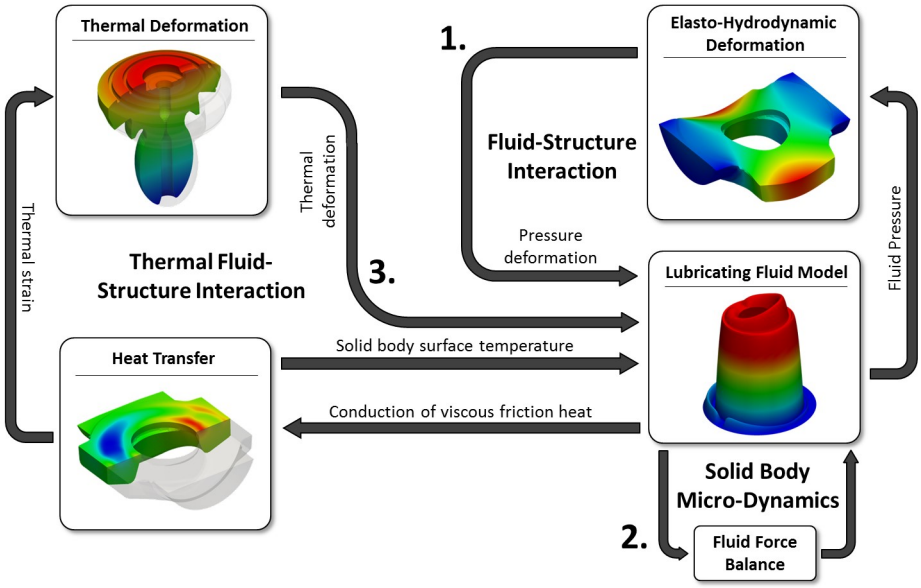

Fig. 1.5. The slipper/swashplate interface fluid-structure and thermal fully coupled model [28].

The study of the analytical modeling of the slipper/swashplate interface was stated by Shute and Turnbull [29] [30]. They calculated the pressure distribution analytically based on a purely hydrostatic bearing assumption. Hook and Li [31] [32] solved the pressure distribution between the slipper and swashplate numerically using the polar form Reynolds equation. Their model allows simulating the slipper with a non-flat surface profile. A non-isothermal fluid flow model was developed by Wieczorek and Ivantysynova [24] that solves the pressure distribution in the slipper/swashplate lubricating gap considering the micromotion of the slipper body and the resulted squeeze effect. The slipper position in their model was determined to fulfill the balance between the external load and the fluid force. Schenk and Ivantysynova [33] [34] [28] brought the slipper/swashplate interface modeling approach into a new level. As Fig. 1.5 shows, they considered the slipper and the swashplate deformation due to both the pressure and the thermal load. Their model solves the three-dimensional

solid body temperature distribution of the slipper and the swashplate in a heat transfer model.

1.3 Aims

Motivated by the inefficiencies of the current scaling methods, the great computational and experimental cost of the current scaling process, as well as the huge potential of a more effective scaling procedure, the aim of this work is to propose a path toward a novel scaling approach that allows axial piston machine scaling research to advance through the development of a multi-physics multi-domain simulation model for evaluating the performance of the virtually scaled pumps and motors, through analysis of the size-dependent performance of the elastohydrodynamic lubricating interfaces via fundamental physics, and through providing a guide axial piston machine scaling with minimum redesign effort while upholding the energy efficiency and life expectancy of the unit.

This global aim leads to the formulation of the following research objectives:

- Creation of an accurate multi-physics multi-domain swashplate type axial piston machine performance prediction tool which can be used without the need for steady state measurement data.
- Analysis of the size-dependence of non-isothermal elasto-hydrodynamic effects in the lubricating interface fluid domain, and of heat transfer and elastic deformation in the solid domain.
- Guide on how to scale a swashplate type axial piston machine such as to uphold its efficiency.

These objectives are met by:

- Developing a next-generation piston/cylinder interface simulation model via high-fidelity implementation of physical effects using a robust numerical algorithm (Chapter 3). The simulation results of the proposed model are compared

to the previous model, and to measurement. The comparison proves the significant improvement on model accuracy the proposed simulation tool has to offer.

- Proposing a semi-empirical thermal boundaries prediction model which calculates the temperature in the outlet flow and case flow from the pump and motor design, and from the simulated efficiency of the lubricating gap model. Unlike the previous model, the proposed model calculates the temperature change due to compression/expansion separately from the heat generation/transfer (Chapter 4). This proposed model is validated against over three hundred steady-state measurements.

- Analyzing fundamental physical effects as they pertain to scaling. Each physical phenomenon, such as the hydrostatic/hydrodynamic effects in lubricating interfaces, the elastic deformation under both pressure and thermal loads, and the heat transfer/generation in both fluid and solid domain, is found to be either scalable (follows the linear scaling rule, i.e. does not contribute to efficiency changes of the unit when scaling), or non-scalable (does not follow the linear scaling rule, and modifies the unit's efficiency). The findings are also demonstrated using the proposed multi-physics, multi-domain axial piston pump model (Chapter 5).

- Proposing a general guide for scaling a swashplate type axial piston machine in order to compensate for the non-scalable physical effects. (Chapter 5).

- Conducting case studies of all three lubricating interfaces for three different unit sizes at multiple operating conditions to demonstrate the potential of the proposed scaling guide, and to propose a preliminary nonlinear scaling rule that is proven to be more effective than the conventional approach. (Chapter 6, Chapter 7, and Chapter 8)

2. THE SWASHPLATE TYPE AXIAL PISTON MACHINES

The kinematics and the dynamics of swashplate type axial piston machines must be defined precisely in order to study the behavior of the three lubricating interfaces in term of the piston/cylinder interface, the cylinder block/valve plate interface, and the slipper/swashplate interface.

In this chapter, the kinematics of swashplate type axial piston machines is derived from the geometrical dimensions. Furthermore, the dynamic loading conditions for each lubricating interface are also explained in detail.

2.1 Kinematics

As the core component of the fluid power system, the swashplate type axial piston machine converts the mechanic power and the fluid power in both directions depends on its working mode. In pumping mode, the shaft torque rotates the cylinder block against the opposing torque due to the pressure force in the displacement chambers applying on the inclined swashplate through the piston/slipper assembly. The fluid, therefore, is displaced from the low-pressure input port to the high-pressure output port. In motoring mode, the pressure force in the displacement chambers applies on the inclined swashplate as a driving torque, drive the cylinder block together with the shaft rotating against the torque load on the shaft.

The kinematic relationship for the swashplate type axial piston machine is shown in Fig. 2.1. A global Cartesian coordinate system is used in Fig. 2.1. The origin of the coordinate system locates at where the shaft axis crosses the virtual plane which all the ball joint centers lay on. The positive z pointing along the shaft axis toward the swashplate, the positive y pointing toward the outer dead center (ODC),

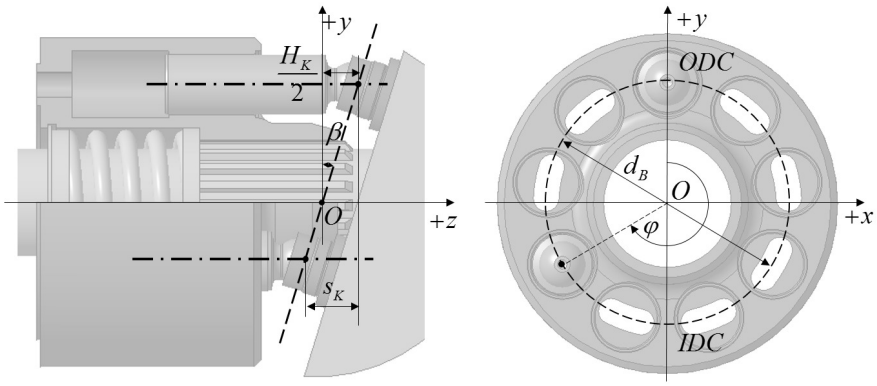

Fig. 2.1. Kinematic relationship for the swashplate type axial piston machine.

and the positive x-direction is defined according to the right-hand rule. According to the research of Ivantysyn and Ivantysynova [1], the maximum stroke H_K, or the maximum piston axial travel distance between the outer dead center (ODC) and the inner dead center (IDC), is dependent on the pitch diameter d_B, and the swash plate angle β:

$$H_K = d_B \cdot \tan\beta \tag{2.1}$$

And the piston stroke is dependent not only on the pitch diameter d_B and the swash-plate angle β, but also on the piston angular position φ:

$$s_K = -1 \cdot d_B \cdot \tan\beta \cdot \frac{1-\cos\varphi}{2} \tag{2.2}$$

The piston axial velocity can be derived from the derivative of the piston stroke:

$$v_K = \frac{ds_K}{d\varphi}\omega = -\frac{1}{2} \cdot d_B \cdot \tan\beta \cdot \sin\varphi \cdot \omega \tag{2.3}$$

where ω is the shaft angular speed.

Then, the piston acceleration can be derived from the derivative of the piston velocity:

$$a_K = \frac{ds_K}{d\varphi}\omega = -\frac{1}{2} \cdot d_B \cdot \tan\beta \cdot \cos\varphi \cdot \omega^2 \tag{2.4}$$

Besides of the axial motion, the piston also subjects to spinning motion about its own axis. The spinning motion of the piston depends on the circumferential friction between the piston and cylinder bore and the friction in the piston ball joint.

This relative spinning motion is discovered by a series of experimental measurements conducted by Renius [35] and confirmed by Lasaar [36] using a specially designed swashplate type axial piston machine which allows directly measuring the axial and circumferential friction between piston and cylinder bore. A value of $speed_K$ is used to describe the piston relative spinning motion, which has a range from 0 to 1. As the Fig. 2.2 shows, $speed_K = 0$ indicates that there is no relative spinning motion between piston and cylinder bore, in the other end, $speed_K = 1$ indicates that the relative spinning speed equals and opposes to the shaft speed, results in zero relative rotation with respect to the global coordinate system.

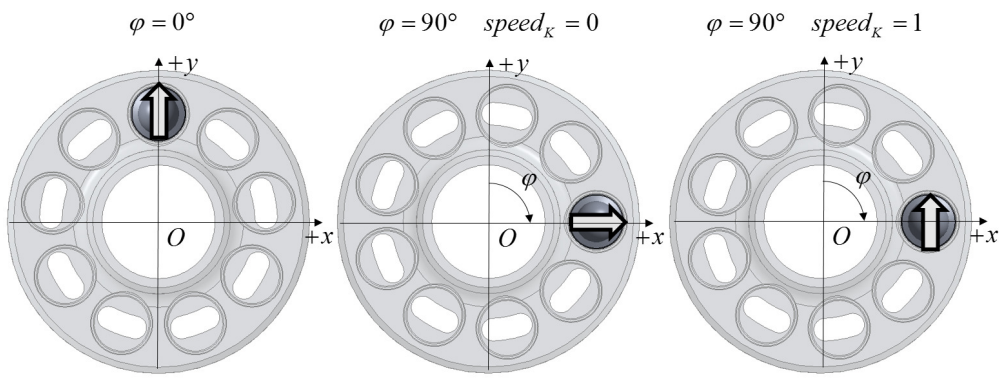

Fig. 2.2. Illustration of piston spinning motion.

2.2 Slipper/swashplate interface

The slipper, as a free body, subjects to numbers of forces and moments. The balancing of the external force and moment applying on the slipper body is achieved through a complicated pressure distribution in the lubricating gap between the slipper and the swashplate which is generated in both hydrostatical way and hydrodynamical way. The dominant external force applies on the slipper socket through the piston ball joint. Due to the nature of the joint and the limited degree of the freedom of the piston in a cylinder bore, only the axial component of the force from the piston contributes to the external force on slipper body.

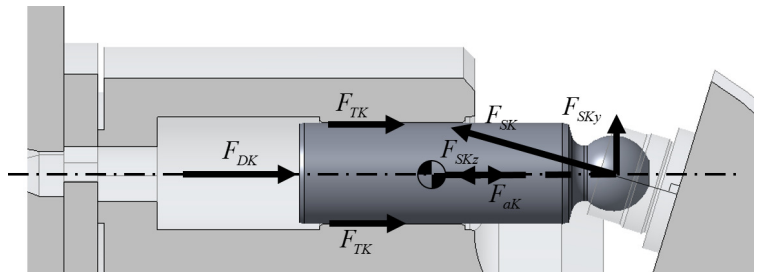

Fig. 2.3. Components of the total axial force from the piston.

The total axial force from the piston F_{SKz} contents the displacement pressure force F_{DK}, the piston/slipper assembly axial inertia force F_{aK} due to the mass of the piston/slipper assembly and the axial acceleration, and the axial friction force F_{TK} between the piston and cylinder bore.

$$F_{SKz} = F_{DK} + F_{aK} + F_{TK} \tag{2.5}$$

The displacement pressure force F_{DK} is dependent on the displacement chamber pressure P_{DC} and the piston diameter d_K:

$$F_{DK} = \frac{\pi d_K^2}{4} \left(p_{DC} - p_{Case}\right) \tag{2.6}$$

The piston/cylinder assembly axial inertia force F_{aK} can be derived from the piston acceleration and the total mass of the piston and the slipper:

$$F_{aK} = (m_K + m_G) \cdot \frac{1}{2} \cdot d_B \cdot \tan\beta \cdot \cos\varphi \cdot \omega^2 \tag{2.7}$$

The magnitude of the axial friction force F_{TK} between the piston and cylinder bore is the integral of the friction distribution in the gap area, and rather difficult to express analytically due to the un-uniform gap height, fluid velocity, and fluid viscosity.

When the swashplate is at a non-orthogonal position, the total axial force from the piston presses the slipper against the inclined swashplate, therefore, F_{SKz} must be decomposed. Due to the fact that the friction in between the slipper and the swashplate is impossible to hold the slipper from sliding away, besides the reaction force from the swashplate which is normal to the swashplate surface, there must be

an additional force holding the slipper at the position, which is the fluid pressure distribution in the piston/cylinder lubricating gap. Therefore, the total axial force from piston F_{SKz} can be decomposed into two components, F_{SK}, which is normal to the swashplate surface, and F_{SKy}, which is perpendicular to the piston axis. Since the direction of both components of F_{SKz} are fixed, the magnitude of both forces can be derived from the swashplate angle.

$$\begin{aligned} F_{SK} &= \frac{F_{SKz}}{\cos\beta} \\ F_{SKy} &= F_{SKz} \cdot \tan\beta \end{aligned} \tag{2.8}$$

Thanks to the slipper mass and its rotational motion around the shaft axis, an inertia force is applied at the slippers center-of-gravity. And the magnitude of the inertia force depends on the mass of slipper m_G, the pitch diameter d_B, and the shaft rotational speed ω.

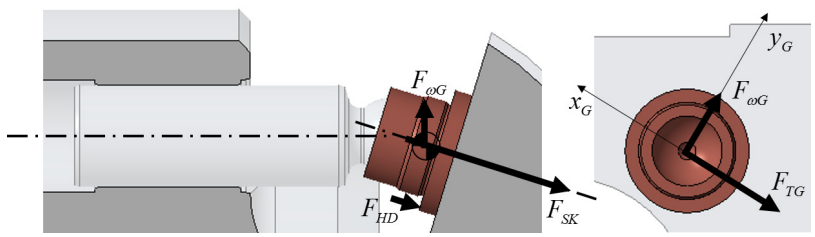

Fig. 2.4. Slipper free body diagram.

$$F_{\omega G} = \frac{d_B}{2} \cdot m_G \cdot \omega^2 \tag{2.9}$$

The radial inertia force of the slipper generates a tilting moment pushes the slipper to tilt outward. This slipper tilting moment is balanced by the asymmetric fluid pressure distribution in the slipper/swashplate gap. The tilting moment controlled by the slipper inertia force $F_{\omega G}$ and the moment lever length l_{SG}. l_{SG} is the distance from the slipper center of mass to the center of the ball joint.

$$M_{\omega G} = F_{\omega G} \cdot l_{SG} \tag{2.10}$$

F_{HD} is the slipper hold-down force that prevents the slipper from lifting up. This lifting up tendency often occurs when slipper is running at low swashplate angle,

low pressure, and high speed. At this situation, the hydrodynamic pressure in the gap together with the slipper inertia tilting moment overbalances the low pressure force in the displacement chamber. An additional assistance is necessary to limit the slipper gap height to prevent large leakage. The slipper hold-down force F_{HD} can be provided by a spring that located between the slipper retainer and the cylinder block, or a fixed slipper hold down mechanism, which provided the hold-down force only when the slipper and swashplate exceeds the nominal design clearance.

The viscous friction between the slipper and swashplate F_{TG} also acts as an external load on the slipper body. The magnitude of the friction, however, is the integral of the local viscous shear over the slipper running surface area, and is rather difficult to express analytically due to the un-uniform gap height, fluid velocity, and fluid viscosity. The slipper/swashplate friction is always parallel to the slipper surface. The friction induces another tilting moment that can be calculated from the friction F_{TG}, and the distance between the piston/slipper ball joint center to the slipper running surface l_G.

$$M_{TG} = F_{TG} \cdot l_G \tag{2.11}$$

The total external load on slipper body discussed above can be expressed as a force F_{Gz} acts on the ball joint center pointing toward the swashplate, and two moments M_{Gx} and M_{Gy} around the ball joint center about both x_G and y_G axis.

$$\begin{cases} F_{Gz} = F_{SK} + F_{HD} \\ M_{Gx} = M_{\omega G} + M_{TGx} \\ M_{Gy} = M_{TGy} \end{cases} \tag{2.12}$$

2.3 Piston/cylinder interface

Similar to the slipper, piston itself can be considered as a free body. The external loads are balanced by the pressure distribution in the piston/cylinder lubricating gap. As described in the previous section, the displacement pressure force F_{DK}, together with the axial inertia force of the piston/slipper assembly F_{aK}, and the

axial friction F_{TK} between piston and cylinder bore, push the piston/slipper assembly axially against the inclined swashplate. This total axial force $F_{SKx} = F_{DK}+F_{aK}+F_{TK}$ is decomposed into two components $F_{SK}$and F_{SKy}. $F_{SK}$is balanced by the pressure distribution in slipper/swashplate interface through the piston slipper ball joint. Since F_{SKy} cannot be balanced from the slipper side, it is considered as an external force applies at the piston slipper ball joint center, pointing to the positive y-direction in the global Cartesian coordinate system.

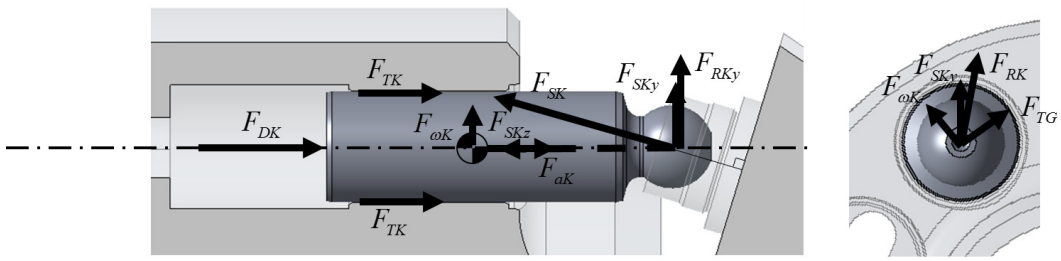

Fig. 2.5. Piston free body diagram.

There are two more forces applies at the center of the ball joint. The radial inertia force of slipper $F_{\omega G}$ applies at the ball joint center with the same direction and magnitude.

$$F_{\omega G} = \frac{d_B}{2} \cdot m_G \cdot \omega^2 \tag{2.13}$$

The viscous friction force between the slipper and the swashplate F_{TG} applies at the ball joint center with the same direction and magnitude as well.

The total resultant external force acts on the center of the ball joint yields:

$$\begin{aligned} F_{RK} &= \sqrt{{F_{RKy}}^2 + {F_{RKx}}^2} \\ &= \sqrt{\left(F_{SKy} + F_{\omega Gy} + F_{TGy}\right)^2 + \left(F_{\omega Gx} + F_{TGx}\right)^2} \end{aligned} \tag{2.14}$$

The radial inertia force of the piston applies at the center of the mass of the piston body with a magnitude which is dependent on the shaft rotational speed ω, the piston mass m_K, and the pitch diameter d_B.

$$F_{\omega K} = m_K \cdot \omega^2 \cdot \frac{d_B}{2} \tag{2.15}$$

Then, the total external load on the piston body can be expressed by two forces acts on the center of the ball joint on x and y direction (F_{Kx} and F_{Ky}), and two moments around the center of the ball joint about x and y axis (M_{Kx} and M_{Ky}):

$$\begin{cases} F_{Kx} = F_{RKx} + F_{\omega Kx} \\ F_{Ky} = F_{RKy} + F_{\omega Ky} \\ M_{Kx} = l_{SK} \cdot F_{\omega Ky} \\ M_{Ky} = -l_{SK} \cdot F_{\omega Kx} \end{cases} \tag{2.16}$$

2.4 Cylinder block/valve plate interface

The cylinder block is assembled on the driving shaft through a crown shaped spline joint, which allows the cylinder block move along the z-axis, and tilt around the crowning point freely. Therefore, the external force applies on the cylinder block on z-direction F_{Bz}, as well as the external moment around x-axis and y-axis $M_{Bx}$and M_{By} are balanced by the fluid pressure distribution between the cylinder block and the valve plate.

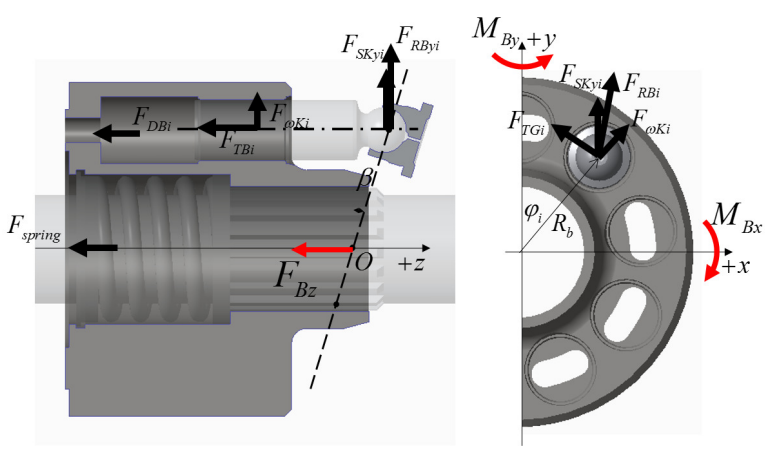

Fig. 2.6. Cylinder block free body diagram.

Firstly, the external forces and moments apply on piston body are balanced by the piston/cylinder interface. Hence, the external loads on all the pistons transmit

through the piston/cylinder interfaces to the cylinder block body. The total forces and moments from all pistons can be expressed using the global coordinate system:

$$\begin{cases} F_{KBx} = \sum_{i=1}^{z} (F_{RKxi} + F_{\omega Kxi}) \\ F_{KBy} = \sum_{i=1}^{z} (F_{RKyi} + F_{\omega Kyi}) \\ M_{KBx} = \sum_{i=1}^{z} \left(\left(l_{SK} - \frac{H_K}{2} + s_{Ki} \right) \cdot F_{\omega Kyi} + \left(s_K - \frac{H_K}{2} \right) F_{RKyi} \right) \\ M_{KBy} = -\sum_{i=1}^{z} \left(\left(l_{SK} - \frac{H_K}{2} + s_{Ki} \right) \cdot F_{\omega Kxi} + \left(s_K - \frac{H_K}{2} \right) F_{RKxi} \right) \end{cases} \tag{2.17}$$

Besides of the forces and moments from all pistons, cylinder block itself also subjects to the displacement pressure force from all the displacement chambers.

For a single displacement chamber, the pressure force can be calculated from the displacement pressure p_{DCi}, piston diameter d_K, and the kidney opening area A_{kidney}.

$$F_{DBi} = p_{DCi} \left(\frac{\pi \cdot {d_K}^2}{4} - A_{kidney} \right) \tag{2.18}$$

The pressure force induced moment then yields:

$$\begin{cases} M_{DBxi} = p_{DCi} \cdot \left(y_{piston\_i} \cdot \frac{\pi \cdot {d_K}^2}{4} - y_{kidney\_i} \cdot A_{kidney} \right) \\ M_{DByi} = -p_{DCi} \cdot \left(x_{piston\_i} \cdot \frac{\pi \cdot {d_K}^2}{4} - x_{kidney\_i} \cdot A_{kidney} \right) \end{cases} \tag{2.19}$$

Above equations to calculate the displacement chamber pressure force and moment are correct only for the common axial piston machine design which fulfills two limitations:

- The cylinder block running surface must be flat
- The pistons must be arranged parallelly to the shaft

Any axial piston machine design which does not fulfill these two limitations is out of the scope of this dissertation.

The total force and moments due to the displacement chamber pressure yields:

$$\begin{cases} F_{DB} = \sum_{i=1}^{z} \left(p_{DCi} \cdot \left(\frac{\pi \cdot {d_K}^2}{4} - A_{kidney} \right) \right) \\ M_{DBx} = \sum_{i=1}^{z} \left(p_{DCi} \cdot \left(y_{piston\_i} \cdot \frac{\pi \cdot {d_K}^2}{4} - y_{kidney\_i} \cdot A_{kidney} \right) \right) \\ M_{DBy} = \sum_{i=1}^{z} \left(-p_{DCi} \cdot \left(x_{piston\_i} \cdot \frac{\pi \cdot {d_K}^2}{4} - x_{kidney\_i} \cdot A_{kidney} \right) \right) \end{cases} \tag{2.20}$$

At most of the operating conditions, the displacement pressure force dominates the external force on z-direction. However, there are two more forces are necessary to be considered when the unit runs under very low pressure.

The shaft spring that locates between the shaft and the cylinder block to pushes the cylinder block toward the valve plate to keep the cylinder block at the desired position when runs under very low pressure. This spring force F_{spring} acts as an external force on the negative z-direction.

The force and moments from the viscous friction from all piston/cylinder interfaces yields:

$$\begin{cases} F_{TB} = \sum_{i=1}^{z} (F_{TBi}) \\ M_{TBx} = \sum_{i=1}^{z} (y_{piston\_i} \cdot F_{TBi}) \\ M_{TBy} = \sum_{i=1}^{z} (-x_{piston\_i} \cdot F_{TBi}) \end{cases} \tag{2.21}$$

The external forces applies on the cylinder block in x and y direction is balanced by the reaction force from the shaft through the crown shape spline joint. Therefore, moments about the global origin are generated when the tipping point of the spline joint is not located exactly at the global origin.

The reaction force from the shaft follows the following equation:

$$\begin{cases} F_{SBx} = -\sum_{i=1}^{z} (F_{RKxi} + F_{\omega Kxi}) \\ F_{SBy} = -\sum_{i=1}^{z} (F_{RKyi} + F_{\omega Kyi}) \end{cases} \tag{2.22}$$

The moment then can be derived using the location of the tipping point relative to the global origin $z_{tipping}$:

$$\begin{cases} M_{SBx} = z_{tipping} \cdot \sum_{i=1}^{z} (F_{RKxi} + F_{\omega Kxi}) \\ M_{SBy} = -z_{tipping} \cdot \sum_{i=1}^{z} (F_{RKyi} + F_{\omega Kyi}) \end{cases} \tag{2.23}$$

The total external load that is balanced by the pressure distribution between the cylinder block and the valve plate then can be expressed as:

$$\begin{cases} F_B = F_{DB} + F_{spring} + F_{TB} \\ M_{Bx} = M_{KBx} + M_{DBx} + M_{TBx} + M_{SBx} \\ M_{By} = M_{KBy} + M_{DBy} + M_{TBy} + M_{SBy} \end{cases} \tag{2.24}$$

3. THE PROPOSED PISTON/CYLINDER INTERFACE MODEL

The state-of-the-art piston/cylinder lubricating interface model is developed by Pelosi [14] (cited as Pelosi's model in this chapter). In this chapter, A multi-physics and multi-domain piston/cylinder lubricating interface model is proposed which based on Pelosi's model with greatly improved accuracy and robustness. Comparing to Pelosi's base model, the proposed model advances at the following points:

- A backward difference squeeze term in the Reynolds equation.
- Improved FVM fluid domain discretion scheme.
- Physics-based boundaries for fluid film thickness.
- Advanced integrated solid body heat transfer model.
- Heat transfer model for compressible fluid.

3.1 Introduction to piston/cylinder interface modeling

Pelosi's piston/cylinder interface structure and thermal interaction model solves the fluid behavior in a discretized finite volume fluid domain. The two-dimensional pressure distribution is solved using the Reynolds equation considering the gap surface deformation, fluid properties, and piston kinematics and micromotion, and the three-dimensional temperature distribution is solved using the energy equation considering the conduction, convection, and the viscous energy dissipation. A pressure deformation model uses an off-line influence matrix method to solve the piston and the cylinder block solid body deformation due to the fluid pressure. The fluid behavior, the pressure deformation, and the fluid properties influence each other in-

stantaneously, therefore, are solved in an iterative loop at each time step, as shown in Fig. 3.1 where referred as the fluid-structure interaction loop. In each simulated shaft revolution, there are 1500 time steps, which are 0.1 degrees apart when the displacement chamber pressure is shifting between high and low port pressure, and 0.25 degrees apart when the displacement chamber connects to either of the ports and achieves a stable pressure. The rate of heat flux from the gap fluid to both the piston and the cylinder block solid bodies is derived from the fluid domain temperature gradient in each time step. The time-weighted averaged gap heat flux rate over each revolution is used as the thermal boundary to solve the three-dimensional heat transfer in the solid bodies. The resulting solid body temperature distribution then induces the thermal deformation, which further changes the fluid domain boundary condition. Another iterative loop is used to solve the fluid structure and thermal interaction, as shown in Fig. 3.1, for each shaft revolution. The simulation finishes when the thermal convergence is achieved.

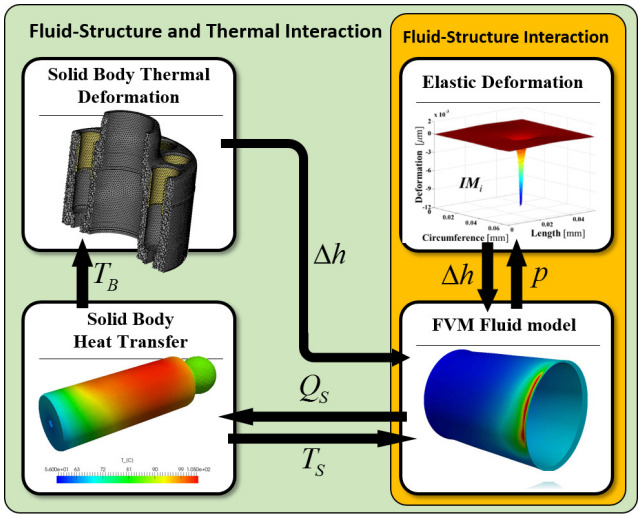

Fig. 3.1. The structure of the piston/cylinder interface fluid structure and thermal interaction model.

3.2 A backward difference squeeze term in the Reynolds equation

The Reynolds equation is used to describe the pressure distribution in a thin lubricating fluid film separating the piston from the cylinder bore. A general form of the Reynolds equation can be expressed as:

$$\nabla \cdot \left(-\frac{\rho {h_g}^3}{12\mu} \nabla p \right) + \frac{(\vec{v}_t + \vec{v}_b)}{2} \cdot \nabla \left(\rho h_g \right) - \rho \vec{v}_t \cdot \nabla h_{gt} + \rho \vec{v}_b \cdot \nabla h_{gb} + \rho \left(w_t - w_b \right) = 0 \tag{3.1}$$

where $-\rho \vec{v}_t \cdot \nabla h_{gt} + \rho \vec{v}_b \cdot \nabla h_{gb}$ is the translational squeeze term and $\rho \left(w_t - w_b \right)$ is the normal squeeze term. t and b stand for the top and bottom surfaces as shown in Fig. 3.2.

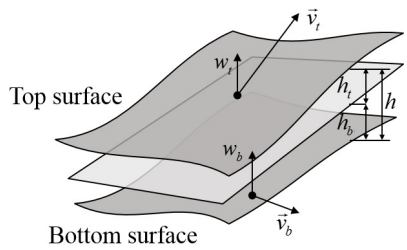

Fig. 3.2. Generalized piston/cylinder lubricating gap

There are two types of squeezing term in Eq. 3.1, namely, the translational squeeze term and the normal squeeze term. Both, the translational squeeze term and the normal squeeze term, describe the change of the local gap height. Therefore, they contribute to the source of the hydrodynamic pressure. In Pelosis piston/cylinder interface model, as mentioned in the state-of-the-art, the normal squeeze term is derived from the piston micromotion, and, the translational squeeze term is derived from the gap geometry, including the piston eccentricity, piston inclination, and the solid bodies deformation, and the piston kinematics. This two-part squeeze term limits the accuracy of the pressure distribution calculation in the piston/cylinder interface in two aspects.

One limitation comes from the missing squeezing effect due to the changing solid bodies elastic deformation. Due to the rapidly changing pressure in the lubricating gap, the piston and the cylinder block are constantly re-deforming, which results in the changing gap height. This changing gap height is not considered in Pelosis two-part squeeze term, therefore, does not contribute to the pressure distribution. This missing source term of the hydrodynamic pressure results in an underestimated the piston/cylinder interface load carrying capacity.

The simulation calculates the position of the piston which fulfills the piston force balance. The calculated fluid force without considering the squeeze term of the changing elastic deformation leads the piston move toward the cylinder bore more to squeeze the fluid film for the adequate hydrodynamic pressure to balance the side load on the piston body. In the simulation, when the gap height is lower than the level of the surface roughness, to keep the numerical calculation from divergence, the fluid film thickness is numerically saturated to the surface roughness. This situation is defined as penetration, and the area where the film thickness is lower than the surface roughness is defined as the penetration area. Fig. 3.3 shows an example of the percentage of the penetration area over the gap area in a simulated revolution of a commercial swashplate type axial piston pump (Sauer-Danfoss S90) when using Pelosis two-part squeeze term. In Fig. 3.3, the x-axis shows the shaft angle ϕ of the piston of interests as shown in Fig. 2.1. In order to demonstrate the push the model to the limitation, the operating condition is selected as the maximum displacement, maximum rated speed, and 450 bar operating pressure with a cylinder bore surface profile as shown in Fig. 3.4. The cylinder bore surface profile was measured after the pump past its run-in phase and reached a stable performance.

Due to the fact that the piston/cylinder interface, in this case, was already run in and achieved stable performance, the fluid film thickness must be higher than the surface roughness during the operation. Otherwise, more material will be worn out because of the solid or mixed friction and will result in a difference pump performance. In Fig. 3.4, the simulation result indicates an example of the underestimated load

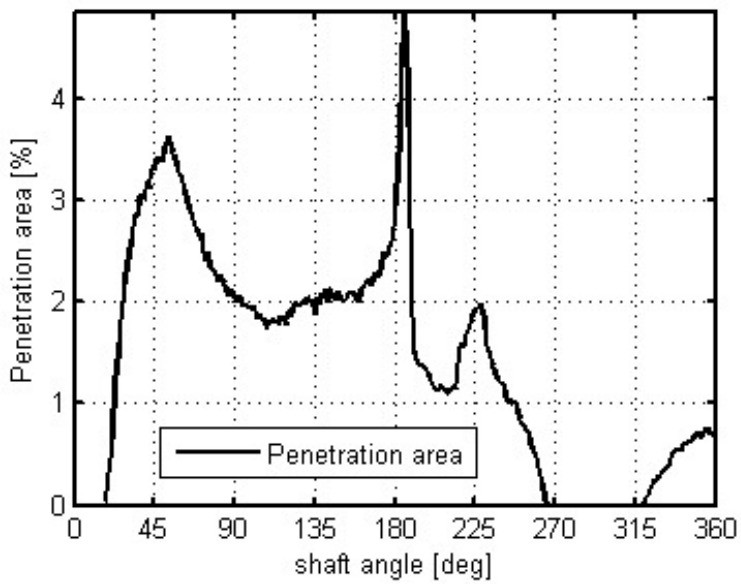

Fig. 3.3. Percentage of penetration area.

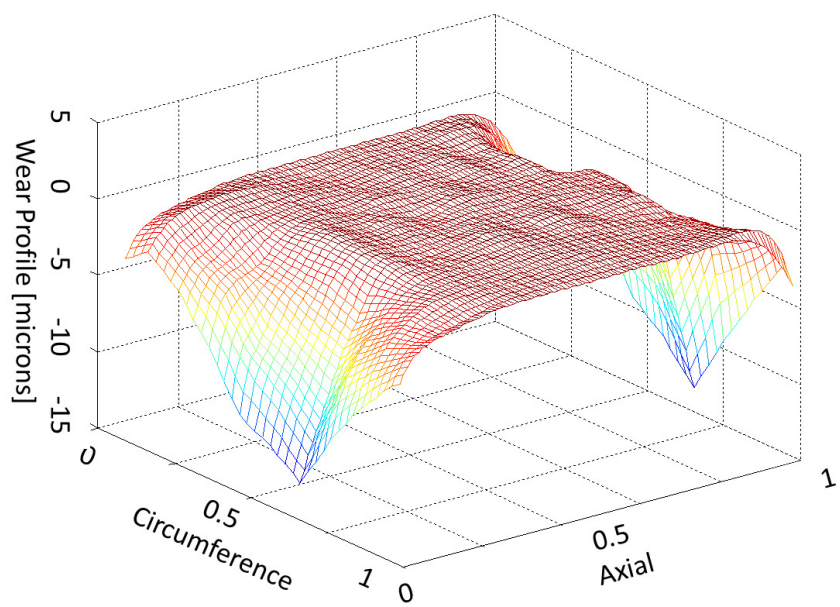

Fig. 3.4. Measured cylinder bore surface profile.

carrying capacity due to the limitation of Pelosis two-parts squeeze term. There are in average more than two percents penetration area in the high-pressure stroke, which

in this case is from 0 to 180 degrees shaft angle. In the low-pressure stroke, which is from 180 to 360 degrees, there is around one percent of penetration. The surface roughness, in this case, is measured at 0.1 microns.

One proposed solution is using a backward difference elasto-hydrodynamic (EHD) squeeze term including the squeeze effect due to the changing elastic deformation to the pressure distribution calculation. The Reynolds equation utilizing this backward EHD squeeze term can be constructed as:

$$\nabla \cdot \left(-\frac{\rho {h_g}^3}{12\mu} \nabla p \right) + \frac{(\vec{v}_t + \vec{v}_b)}{2} \cdot \nabla \left(\rho h_g \right) - \rho \vec{v}_t \cdot \nabla h_{gt} + \rho \vec{v}_b \cdot \nabla h_{gb} \\ + \rho \left(w_t - w_b \right) + \rho \left(\frac{dh_{EHD}}{dt} \right) = 0 \tag{3.2}$$

where the backward difference EHD squeeze term is derived from:

$$\frac{dh_{gEHD}}{dt} = \frac{h_{gEHD\_current} - h_{gEHD\_previous}}{t_{current} - t_{previous}} \tag{3.3}$$

By including the EHD squeezing effect, the penetration area is smaller compared to Pelosis version as shown in Fig. 3.5, which, as discussed before, is an indication of more accurate pressure distribution, fluid force, and load carrying capacity calculation. According to the calculated penetration area that in Fig. 3.5, adding the additional backward difference EHD squeeze term improves the load carrying capability calculation accuracy. However, the simulation still missing part of the load carrying capacity due to another limitation of Pelosis squeeze term.

In the Pelosis piston/cylinder interface simulation, the position of the piston is solved to fulfill the force balance using the Newton-Raphson method as shown in Fig. 3.6. The Jacobian matrix describing how the fluid force responds to the piston position is solved using a forward and backward difference that requires the fluid pressure distribution to be solved with the piston position numerically moved forwards and backward from it physical position. When the piston is heavily inclined, and the minimum film thickness is approaching the level of the surface roughness, the temporary numeric movement of the piston position which is required to construct the Jacobian matrix can result in a penetration situation.

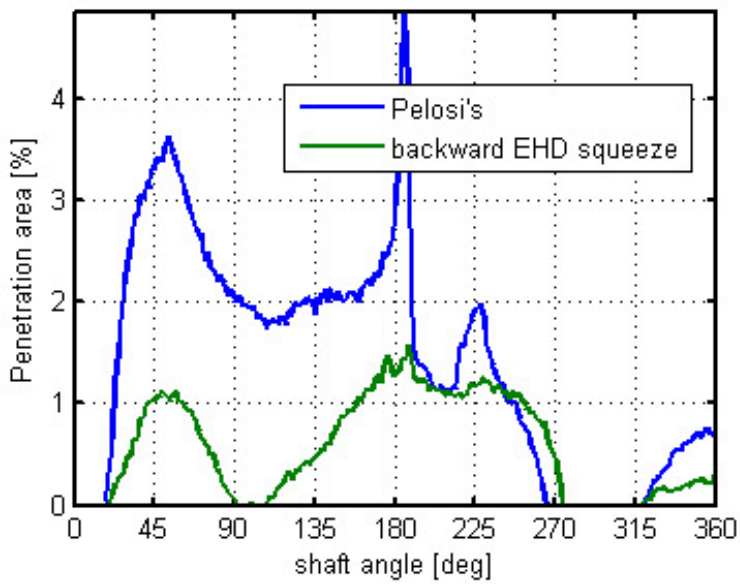

Fig. 3.5. EHD squeeze impacts on bearing function.

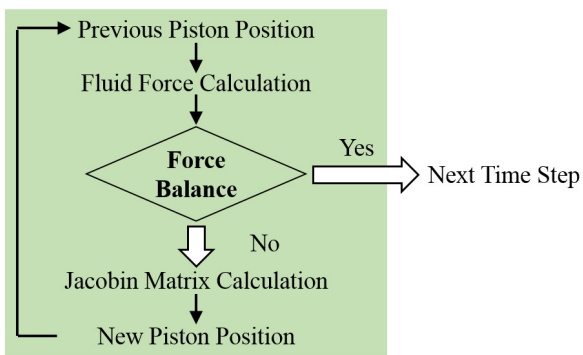

Fig. 3.6. Newton-Raphson method to find piston position that fulfills the force balance.

Where the penetration occurs, the fluid film thickness is numerically saturated, therefore, is not able to further decrease, or further squeezed. However, Pelosis squeeze term considers only the piston kinematics, and the backward EHD squeeze term adds the changing of the pressure deformation into the consideration. Both of the methods still calculate positive squeezing source term from the piston movement even though the film thickness is no longer decreasing. This disagreement between

the calculated film thickness and its changing rate results in an unrealistic pressure distribution in the Jacobian matrix calculation, which then leads to an unrealistic fluid force piston position response, and an unrealistic piston micromotion.

The proposed solution is a backward difference method to quantify the squeeze term in the pressure distribution calculation from the current gap height, the previous gap height, and the time difference between the current and the previous time step. The Reynolds equation containing the proposed backward difference squeeze term is:

$$\nabla \cdot \left(-\frac{\rho h_g^3}{12\mu} \nabla p \right) + \frac{(\vec{v}_t + \vec{v}_b)}{2} \cdot \nabla \left(\rho h_g \right) - \rho \left(\frac{h_{gcurrent} - h_{gprevious}}{t_{current} - t_{previous}} \right) = 0 \tag{3.4}$$

The proposed backward difference squeeze term covers all the physical and numerical phenomena that impact the changing fluid film thickness completely since both the current gap height and the previous gap height contain the rigid piston body position, the pressure and the thermal deformation, and the film thickness numerical saturation in the penetration area.

Fig. 3.7 shows the piston/cylinder interface simulation scheme using the proposed backward difference squeeze term. The previous gap height as written as $h_{gprevious}$ in Eq. 3.5 is updated after the fluid-structure interaction (FSI) loop and before the force balance loop in each time step since the piston position is calculated using the implicit Newton-Raphson method in the force balance loop.

As explained before, this penetration area is resulted from the unbalanced load, which can be considered as the error between the calculated and the real load carrying capacity. Fig. 3.8 shows the penetration area comparison between Pelosis squeeze term, the backward EHD squeeze term, and the proposed backward difference squeeze term. This comparison result demonstrates that the proposed backward difference squeeze term significantly improves the piston/cylinder interface simulation accuracy, especially in term of the load carrying capability calculation, from Pelosis baseline simulation.

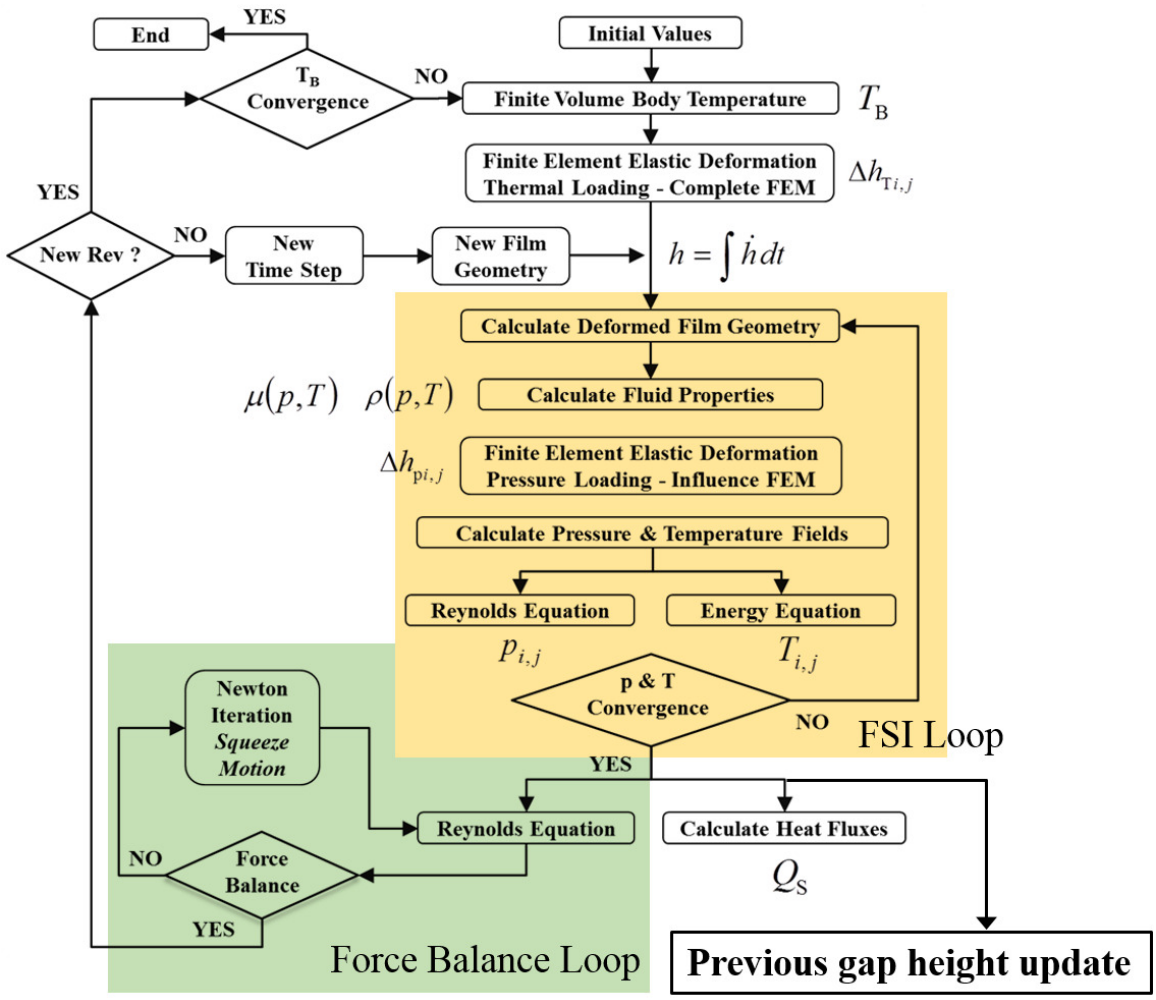

Fig. 3.7. Piston/cylinder interface simulation scheme using the proposed backward difference squeeze term.

3.3 Improved FVM fluid domain discretion scheme

Pelosis Gauss-Seidel pressure distribution model solves the Reynolds equation in a two dimensional Cartesian discretized fluid domain assuming no pressure gradient across the third dimension which is in the fluid film thickness direction. As figure 4.9 shows, in the discretized fluid grid, the north is defined as the direction of the ball joint, and the south is defined as the direction of the pistons flat end. Each fluid cell P connects to its north, south, east, and west neighbor cells N, S, E, and W through

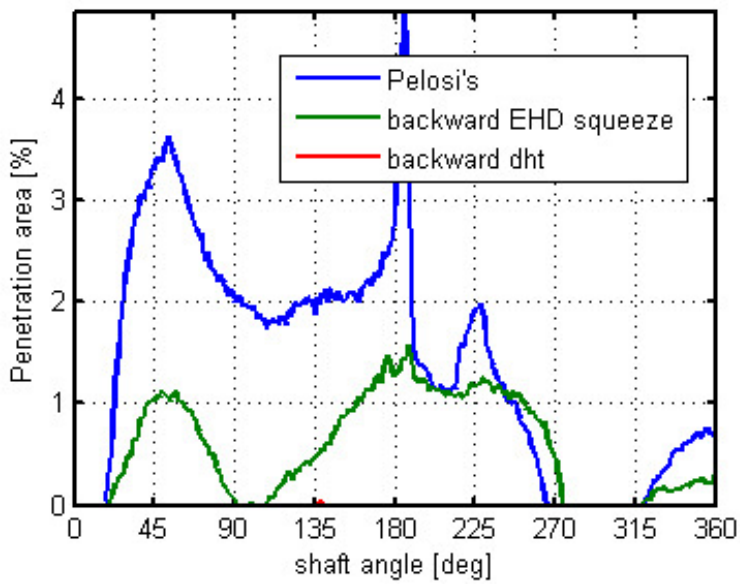

Fig. 3.8. Bearing function simulation comparison.

the wall n, s, e, and w. In order to solve the Reynolds equation using the finite volume method, the mass flow rate through the wall, which is the function of the gap height, the fluid viscosity and the density on the wall is required to form the diffusive terms in the partial differential equation. The discretization over a fluid domain cell yields:

$$\begin{aligned}&\frac{\rho_e h_{ge}^3}{\mu_e}\frac{(p_E - p_P)}{dx_e}\Delta y - \frac{\rho_w h_{gw}^3}{\mu_w}\frac{(p_P - p_W)}{dx_w}\Delta y \\ &+ \frac{\rho_n h_{gn}^3}{\mu_n}\frac{(p_N - p_P)}{dy_n}\Delta x - \frac{\rho_s h_{gs}^3}{\mu_s}\frac{(p_P - p_S)}{dy_s}\Delta x - S\Delta x\Delta y = 0\end{aligned} \tag{3.5}$$

The wall value of the gap height, the fluid density, and the fluid viscosity in Pelosis pressure distribution model is obtained assuming linear distribution from the cell centroid to its neighbor cells centroid, as:

$$\begin{aligned}&h_{ge} = \frac{h_{gP} + h_{gE}}{2} \quad h_{gw} = \frac{h_{gP} + h_{gW}}{2} \quad h_{gn} = \frac{h_{gP} + h_{gN}}{2} \quad h_{gs} = \frac{h_{gP} + h_{gS}}{2} \\ &\rho_e = \frac{\rho_P + \rho_E}{2} \quad \rho_w = \frac{\rho_P + \rho_W}{2} \quad \rho_n = \frac{\rho_P + \rho_N}{2} \quad \rho_s = \frac{\rho_P + \rho_S}{2} \\ &\mu_e = \frac{\mu_P + \mu_E}{2} \quad \mu_w = \frac{\mu_P + \mu_W}{2} \quad \mu_n = \frac{\mu_P + \mu_N}{2} \quad \mu_s = \frac{\mu_P + \mu_S}{2}\end{aligned} \tag{3.6}$$

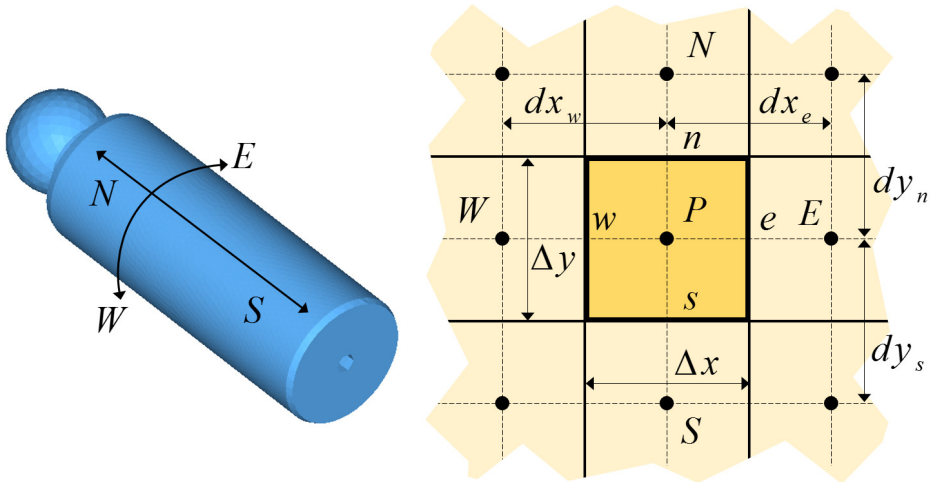

Fig. 3.9. Finite volume discretization for pressure distribution calculation.

However, both the fluid density and the fluid viscosity changes with the fluid temperature and pressure nonlinearly. Fig. 3.10 and Fig. 3.11 shows the measured fluid density and viscosity of a type of HLP-32 mineral hydraulic oil changing over the fluid pressure at a constant temperature.

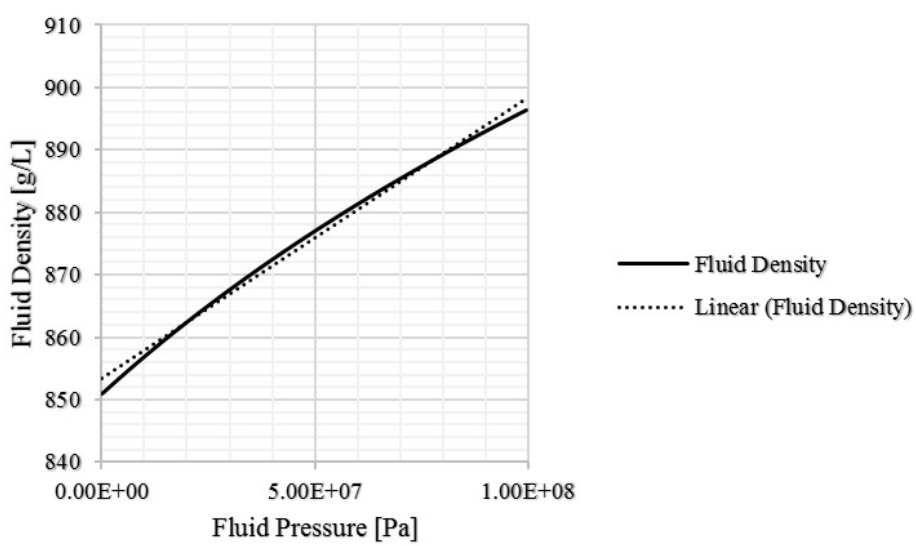

Fig. 3.10. Fluid density change with pressure.

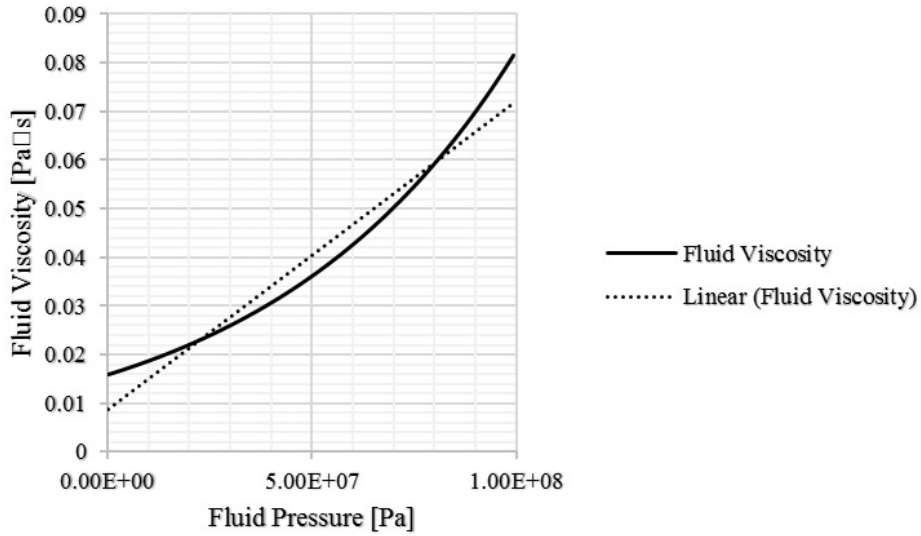

Fig. 3.11. Fluid viscosity change with pressure.

Comparing to the concave density curve and convex viscosity curve, the linear approximation underestimates the fluid density and overestimates the fluid viscosity on the cell wall between two fluid cells. According to Eq, 3.4 both linearly approximated fluid density and fluid viscosity on the cell wall underestimate the diffusive coefficients, therefore, results in unrealistic pressure spikes.

Instead of using linearly approximated fluid properties from the cell centroid value to its neighbor cells centroid value, the proposed improved wall value estimation method directly calculates the fluid density and the fluid viscosity from the fluid pressure and fluid temperature. The pressure and temperature are obtained assuming a linear gradient from the cell center to its neighbor cells center, as shown in Eq. 3.7.

$$\begin{aligned}
\rho_e &= \rho\left(\frac{p_P+p_E}{2},\frac{T_P+T_E}{2}\right) \quad \rho_w = \rho\left(\frac{p_P+p_W}{2},\frac{T_P+T_W}{2}\right)\\
\rho_n &= \rho\left(\frac{p_P+p_N}{2},\frac{T_P+T_N}{2}\right) \quad \rho_s = \rho\left(\frac{p_P+p_S}{2},\frac{T_P+T_S}{2}\right)\\
\mu_e &= \mu\left(\frac{p_P+p_E}{2},\frac{T_P+T_E}{2}\right) \quad \mu_w = \mu\left(\frac{p_P+p_W}{2},\frac{T_P+T_W}{2}\right)\\
\mu_n &= \mu\left(\frac{p_P+p_N}{2},\frac{T_P+T_N}{2}\right) \quad \mu_s = \mu\left(\frac{p_P+p_S}{2},\frac{T_P+T_S}{2}\right)
\end{aligned} \tag{3.7}$$

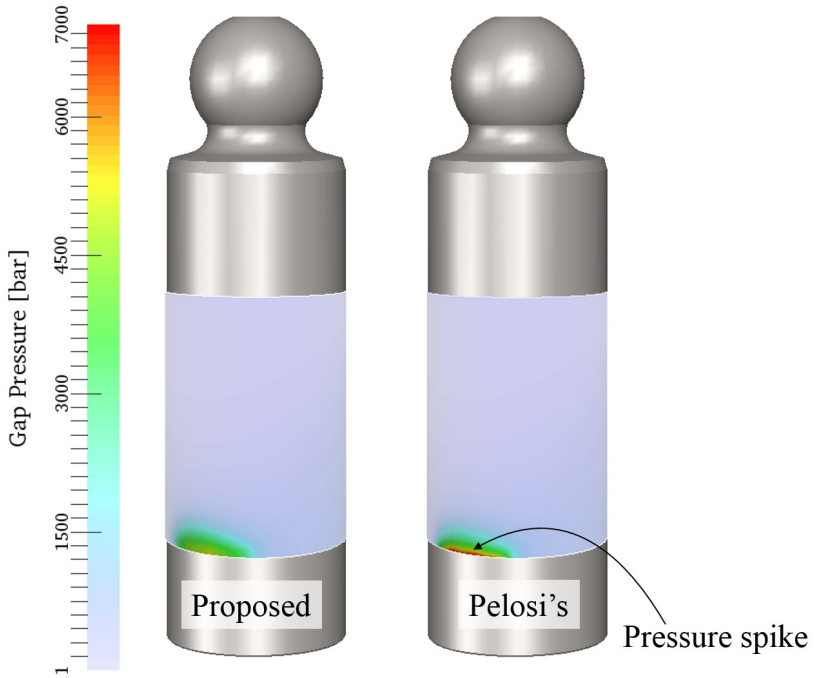

Fig. 3.12. Gap pressure distribution comparison at 90-degree shaft angle.

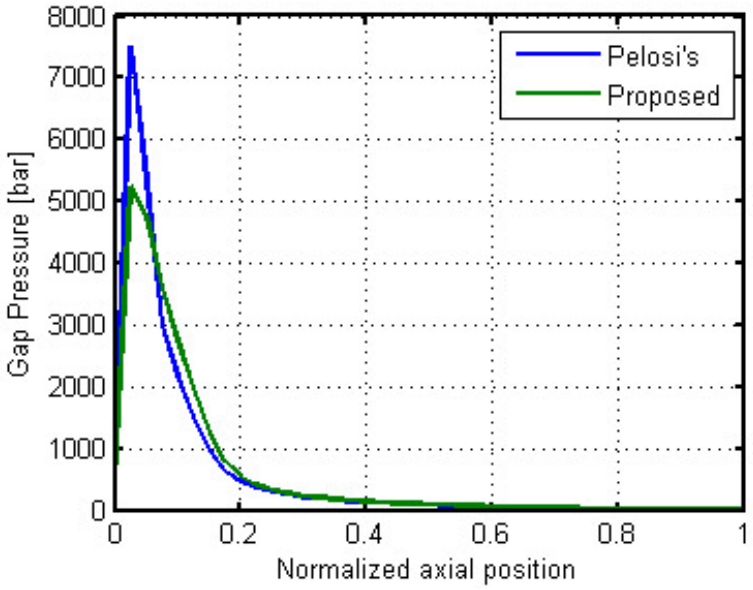

Fig. 3.13. Gap pressure spike comparison at 90-degree shaft angle.

Fig. 3.12 shows the gap pressure distribution comparison between Pelosis model and the model uses the proposed fluid properties estimation on the cell walls. The

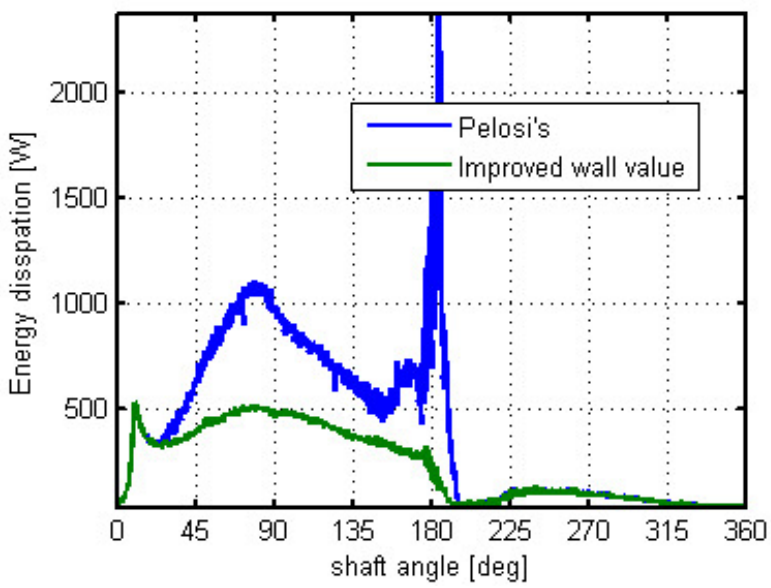

Fig. 3.14. Single piston/cylinder interface energy dissipation comparison.

figure shows the simulated pressure distribution in the piston/cylinder interface gap of a commercial pump at the shaft angle of 90 degrees at the maximum speed, 450 bar, and full displacement. According to Fig. 3.12, with the fluid properties estimation closer to reality, the simulated pressure distribution using the proposed improved model is smoother than the one using Pelosis model. The difference in the pressure peaks can be observed in more detail in Fig. 3.13, which shows the pressure distribution over the gap length crossing the pressure peak region in Fig. 3.12. The normalized axial position in Fig. 3.13 indicates the distance from the edge of the gap on the displacement chamber edge normalized by the axial length of the lubricating gap. In the direct comparison of the simulated pressure spikes between the proposed model and Pelosis model, the peak pressure of the simulation using the proposed fluid properties estimation on the fluid cell wall is 2000 bar lower than the one using Pelosis method. This pressure difference also results in different energy dissipation in the piston/cylinder lubricating gap. Fig. 3.14 shows the simulated energy dissipation in a single piston/cylinder lubricating interface using the proposed fluid properties estimation on the cell wall comparing to the one using Pelosis method. The energy

dissipation comparison indicates that the improved accuracy of the fluid properties estimation significantly influences the predicted piston/cylinder interfaces power loss.

3.4 Physics-based boundaries for fluid film thickness

The cylindrical piston/cylinder lubricating interface has two edges, one on the displacement chamber end, and one on the case end. The inclination of the piston generates regions of very thin fluid film located around both edges to provide the hydrodynamic pressure force to balance the external side load from the piston ball joint. Due to the low film thickness, the fluid viscous friction around both edges contributes most of the energy dissipation in the piston/cylinder lubricating gap. As described in previous sections, the pressure distribution in the lubricating gap between the piston and the cylinder bore is simulated by numerically solving the Reynolds equation in a two dimensional Cartesian discretized finite volume structure. The Reynolds equation with the forward difference linear approximation of the pressure gradients yields:

$$\begin{aligned}
&\frac{\rho_e h_{ge}^3}{\mu_e}\frac{(p_E - p_P)}{dx_e}\Delta y - \frac{\rho_w h_{gw}^3}{\mu_w}\frac{(p_P - p_W)}{dx_w}\Delta y \\
&+ \frac{\rho_n h_{gn}^3}{\mu_n}\frac{(p_N - p_P)}{dy_n}\Delta x - \frac{\rho_s h_{gs}^3}{\mu_s}\frac{(p_P - p_S)}{dy_s}\Delta x \\
&- 6\left[-v_x\frac{\partial}{\partial x}(\rho h_g) - v_y\frac{\partial}{\partial y}(\rho h_g) + 2\rho_p\left(\frac{dh_g}{dt}\right) - 2h_p\left(\frac{d\rho}{dt}\right)\right]\Delta x\Delta y = 0
\end{aligned} \tag{3.8}$$

With the central difference linear approximation of the density and gap height difference, equation 4.8 becomes:

$$\begin{aligned}
&\frac{\rho_e h_{ge}^3}{\mu_e}\frac{(p_E - p_P)}{dx_e}\Delta y - \frac{\rho_w h_{gw}^3}{\mu_w}\frac{(p_P - p_W)}{dx_w}\Delta y \\
&+ \frac{\rho_n h_{gn}^3}{\mu_n}\frac{(p_N - p_P)}{dy_n}\Delta x - \frac{\rho_s h_{gs}^3}{\mu_s}\frac{(p_P - p_S)}{dy_s}\Delta x \\
&- 6\left[-v_x\left(\frac{\rho_e h_{ge} - \rho_w h_{gw}}{\Delta x}\right) - v_y\left(\frac{\rho_n h_{gn} - \rho_s h_{gs}}{\Delta y}\right)\right]\Delta x\Delta y \\
&- 6\left[2\rho_p\left(\frac{dh_g}{dt}\right) - 2h_p\left(\frac{d\rho}{dt}\right)\right]\Delta x\Delta y = 0
\end{aligned} \tag{3.9}$$

The gap height on the wall of the cells is estimated assume linear gap height gradients between the cell center and its neighbors cell center, as:

$$h_{ge} = \frac{h_{gP} + h_{gE}}{2} \quad h_{gw} = \frac{h_{gP} + h_{gW}}{2} \quad h_{gn} = \frac{h_{gP} + h_{gN}}{2} \quad h_{gs} = \frac{h_{gP} + h_{gS}}{2} \tag{3.10}$$

This gap height approximation is only possible for the cell which locates not on the gap edge where only three instead of four neighbor cells exist. Pelosi uses the gap height at the centroid of the cell as the gap height on the cell wall where the neighbor is missing.

On the displacement chamber end, according to Pelosis model, the gap height on the cell wall yields:

$$h_{ge} = \frac{h_{gP} + h_{gE}}{2} \quad h_{gw} = \frac{h_{gP} + h_{gW}}{2} \quad h_{gn} = \frac{h_{gP} + h_{gN}}{2} \quad h_{gs} = h_{gP} \tag{3.11}$$

On the case end, the gap height on the cell wall yields:

$$h_{ge} = \frac{h_{gP} + h_{gE}}{2} \quad h_{gw} = \frac{h_{gP} + h_{gW}}{2} \quad h_{gn} = h_{gP} \quad h_{gs} = \frac{h_{gP} + h_{gS}}{2} \tag{3.12}$$

However, this estimation method compromises both the source terms and the diffusive terms in the Reynolds equation. Combining the already very low film thickness on the edge of the gap, which intensifies the hydrodynamic effect, Pelosis compromised wall gap height estimation on the gap edge induces instability to the simulated piston/cylinder lubricating interface fluid behavior, which results in unrealistic energy dissipation.

The proposed method quantifies the fluid film thickness on the edge of the lubricating interface directly from the piston position and the edge elastic deformation due to the pressure and the thermal load.

On the displacement chamber end, the proposed method quantifies the gap height on the cell wall as:

$$\begin{aligned} &h_{ge} = \frac{h_{gP} + h_{gE}}{2} \quad h_{gw} = \frac{h_{gP} + h_{gW}}{2} \quad h_{gn} = \frac{h_{gP} + h_{gN}}{2} \\ &h_{gs} = h_{gDCedge\_rigid} + \Delta h_{gDCedge\_pdef} + \Delta h_{gDCedge\_Tdef} \end{aligned} \tag{3.13}$$

On the case end, the wall gap height yields:

$$h_{ge} = \frac{h_{gP} + h_{gE}}{2} \quad h_{gw} = \frac{h_{gP} + h_{gW}}{2} \quad h_{gs} = \frac{h_{gP} + h_{gS}}{2}$$
$$h_{gn} = h_{gCaseedge\_rigid} + \Delta h_{gCaseedge\_pdef} + \Delta h_{gCaseedge\_Tdef} \tag{3.14}$$

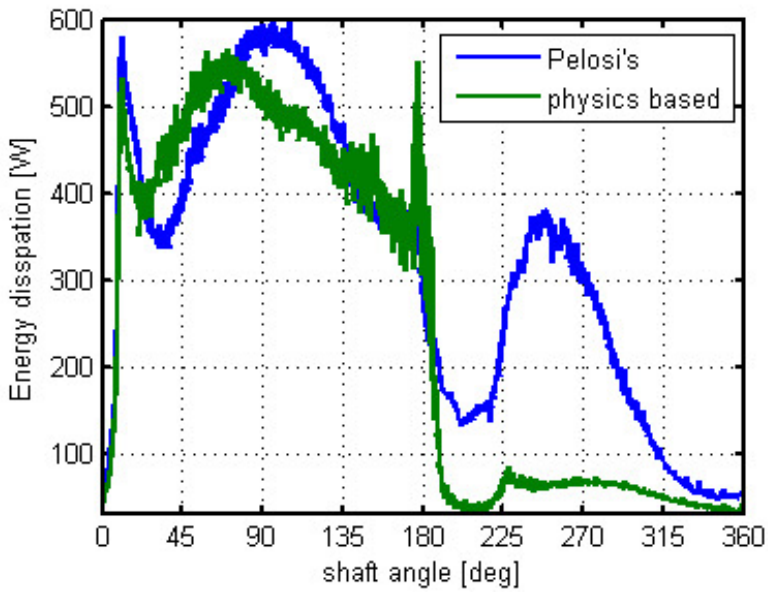

Fig. 3.15. Single piston/cylinder interface energy dissipation comparison of the gap height estimation method between Pelosis and the proposed.

Fig. 3.15 shows a comparison of the simulated energy dissipation of a single piston/cylinder interface of a commercial pump between using Pelosis method and the proposed method. The operating condition of this comparison study is maximum speed, 450 bar, and full displacement. The comparison study shows similar simulated energy dissipation during the high-pressure stroke between 0 and 180 degrees of shaft angle. However, the energy dissipation in the low-pressure stroke shows a significant difference. Due to the compromised gap height estimation on the gap edge, the unstable fluid film behavior induces spikes on the edge of the lubricating gap which results in the unrealistic high energy dissipation. Fig. 3.16 shows an unrealistic pressure spike on the lubricating gap edge when the shaft angle is at 255 degrees.

Note that there is no cylinder bore profile has been used in this comparison study since the measured profile as Fig. 3.4 increase the film thickness around the gap edge. The gap height on the edge is no longer critical when cylinder bore profile is applied, therefore no significant difference between this two edge gap height methods.

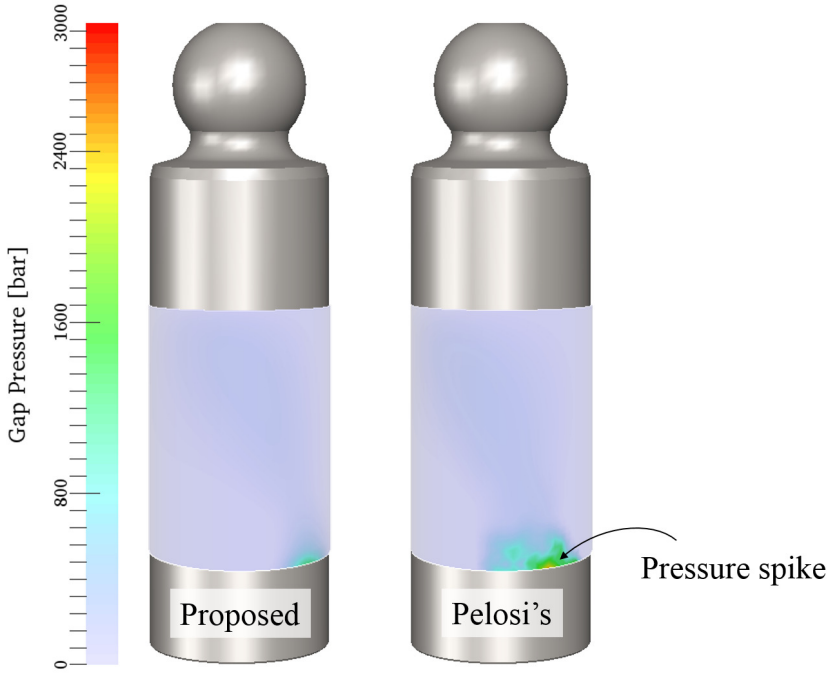

Fig. 3.16. Pressure distribution comparison of the gap height estimation method between Pelosis and the proposed.

3.5 Advanced integrated solid body heat transfer model

The three-dimensional solid body heat transfer model for the piston/cylinder interface mentioned in the previous chapter is based on the finite element discretization of the solid bodies. The steady-state diffusive form of energy equation as shown in Eq. 3.15 is used to determine the temperature distribution.

$$\nabla \cdot (\kappa_{solid} \nabla T) = 0 \tag{3.15}$$

The temperature at each nodal position then solved in a linear system:

$$\begin{aligned} \mathbf{M_P T_P} &= \mathbf{q_P} \\ \mathbf{M_B T_B} &= \mathbf{q_B} \end{aligned} \tag{3.16}$$

where $\mathbf{T_P}$ and $\mathbf{T_B}$ are the vectors of the temperature field of piston and cylinder block, $\mathbf{q_P}$ and $\mathbf{q_B}$ are the vectors of the thermal boundaries on the piston and the cylinder block solid bodies, and $\mathbf{M_P}$ and $\mathbf{M_B}$ are the matrices contain the conductivity between each node. The conductivity matrices are constructed from the material properties of the piston and the cylinder block solid bodies and the position of each node.

Unlike the simulation scheme of Pelosis model, which solves the temperature distribution in the piston and the cylinder block solid bodies separately, the proposed advanced heat transfer model solves the dual-body temperature distribution in an integrated linear system.

In this integrated linear system as shown in Eq. 3.17, there are two extra matrices $\mathbf{M_{b2p}}$ and $\mathbf{M_{p2b}}$ contain the conductivity of the fluid film between the piston and the cylinder block.

$$\left(\begin{bmatrix} \mathbf{M_P} & 0 \\ 0 & \mathbf{M_B} \end{bmatrix} + \begin{bmatrix} \mathbf{M_{b2p}} \\ \mathbf{M_{p2b}} \end{bmatrix} \right) \begin{bmatrix} \mathbf{T_P} \\ \mathbf{T_B} \end{bmatrix} = \begin{bmatrix} \mathbf{q_P} \\ \mathbf{q_B} \end{bmatrix} \tag{3.17}$$

In order to construct the matrix $\mathbf{M_{b2p}}$, the relationship of the temperature at face i of the piston running surface, the temperature at the face j on the cylinder bore running surface, and the average heat flux between face i and face j in one shaft revolution must be found first. The instantaneous piston/cylinder interface mesh relative position is shown in Fig. 3.17.

For each single time step, the heat flux on piston face i can be determined by:

$$q_i = \frac{\kappa_{fluid}}{h_{g(i,t)}} \left(T_{ref} - T_i \right) \tag{3.18}$$

where $h_{g(i,t)}$ is the gap height and T_{ref} is the cylinder bore surface temperature at the reference location. As shown in figure 4.17, the reference location is defined as the projection of face i on cylinder bore. Due to the relative motion of the piston,

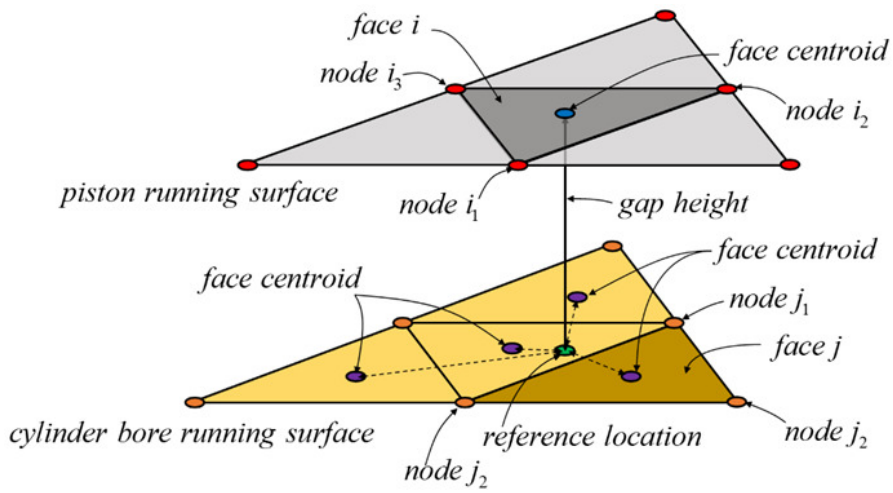

Fig. 3.17. Instantaneous piston/cylinder interface mesh relative position.

having a face exactly at the reference location is not possible. Therefore, the reference temperature T_{ref} is the weighted average of the temperatures of the faces on cylinder bore running surface near the reference location. Then, the instantaneous heat flux from face j to face i yields:

$$q_{ij} = \kappa_{fluid} \left(\frac{wt_{i,j,t}}{h_{g(i,t)}} \cdot (T_j - T_i) \right) \tag{3.19}$$

where $wt_{i,j,t}$ is the weight according to the distance between the location of face and the reference location.

The average heat flux from face j to face i over one shaft revolution yields

$$q_{avg\_ij} = \frac{n}{60} \cdot \sum_{t=0}^{60/n} [q_{ij} \cdot dt] \tag{3.20}$$

Rewrite Eq. 3.20:

$$q_{avg\_ij} = \frac{n}{60} \cdot \kappa_{fluid} \cdot (T_j - T_i) \, \mathbf{B2K} \, [i, j] \tag{3.21}$$

where the matrix **B2K** yields:

$$\mathbf{B2K} \, [i, j] = \sum_{t=0}^{60/n} \left(\frac{wt_{i,j,t}}{h_{g(i,t)}} \cdot dt \right) \tag{3.22}$$

Three nodes define each triangular face. As shown in figure 4.17, face i is defined by node $i_1, i_2, i_3$and face j is defined by node j_1, j_2, j_3. Each node can be used to define

multiple faces. The face temperature is defined as the average of the temperature of the three nodes. The heat flux on each face distributed to the three nodes evenly is shown in Fig. 3.18.

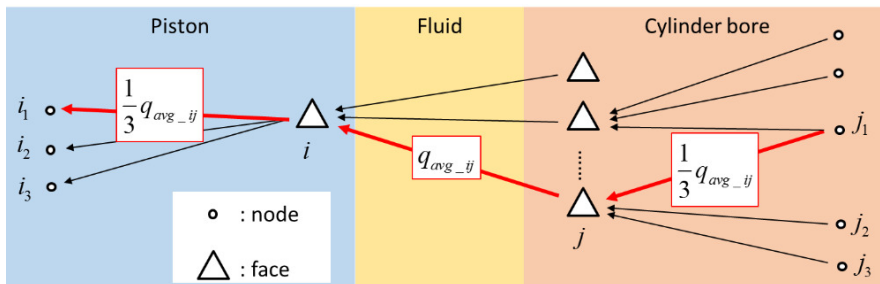

Fig. 3.18. Node to node heat flux.

The relationship between the temperature at piston nodes i_1, i_2, i_3 and cylinder block nodes j_1, j_2, j_3 and the conduction heat flux from face j to face i yields:

$$\sum_{m=1}^{3}\left(\sum_{n=1}^{3}\mathbf{M_{b2p}}\left[i_m, i_n\right]\mathbf{T_P}\left[i_n\right]+\sum_{n=1}^{3}\mathbf{M_{b2p}}\left[i_m, j_n\right]\mathbf{T_B}\left[j_n\right]\right)=q_{avg\_ij}\cdot A_i \tag{3.23}$$

where A_i is the area of face i.

Then, the matrix $\mathbf{M_{b2p}}$ can be constructed as:

$$\begin{aligned}\mathbf{M_{b2p}}\left[i_m, i_n\right]&=\frac{n}{60}\cdot\kappa_{fluid}\cdot\frac{1}{9}A_i\cdot\mathbf{B2K}\left[i,j\right]\\ \mathbf{M_{b2p}}\left[i_m, j_n\right]&=-\frac{n}{60}\cdot\kappa_{fluid}\cdot\frac{1}{9}A_i\cdot\mathbf{B2K}\left[i,j\right]\end{aligned} \tag{3.24}$$

In the fluid-structure and thermal interaction model using the proposed advanced heat transfer model, thanks to the fact that the conduction between the two running surfaces is already included in the linear system, the only changing thermal boundary between each iteration is the energy dissipation and the fluid convection in the gap, which is less sensitive to the solid body temperature.

In order to test the fluid structure and thermal interaction model with the advanced heat transfer model, a challenging operating condition is selected with a tighter clearance. The operating condition is the maximum, 50bar, and 20% displacement. The high speed leads to high energy dissipation in the gap. The low pressure causes

the low gap flow, therefore, low fluid convection. The low displacement leads to a low axial motion of the piston, therefore, concentrated heat flux.

Fig. 3.19 shows the simulated piston temperature distribution from the fourth revolution to the ninth revolution using the Pelosis heat transfer model. The piston temperature is not converging in this iterative fluid structure and thermal interaction simulation process.

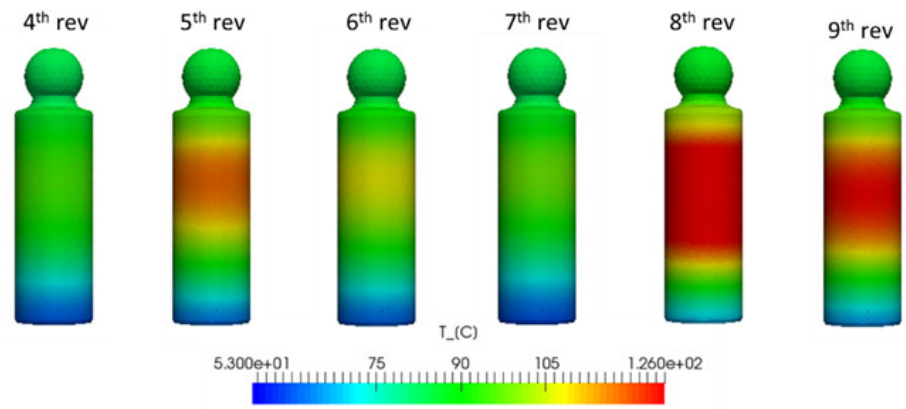

Fig. 3.19. The piston temperature convergence check for the previous model.

Fig. 3.20 shows the simulated piston temperature distribution from the fourth revolution to the ninth revolution using the advanced heat transfer model. The piston temperature converged on the ninth revolution, and the temperature difference between each iteration shows a stable converging process.

In summary, the proposed advance heat transfer model for the solid parts of the piston/cylinder interface that uses the integrated linear system to solve the temperature distribution in both solid bodies simultaneously improves the convergence of the iterative process of the fluid-structure and thermal interaction model without compromise the result accuracy. A challenging operating condition with high speed, low pressure, and low displacement is used to test the performance of the model. The simulation result comparison demonstrates the improvement of this proposed advanced heat transfer model.

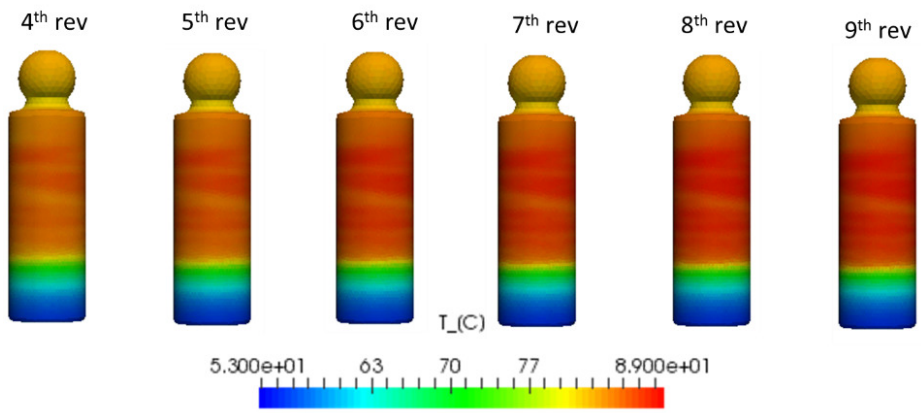

Fig. 3.20. The piston temperature convergence check for the advanced heat transfer model.

3.6 Heat transfer model for compressible fluid

The thermal behavior in the fluid domain of the piston/cylinder interface couples multiple physical phenomena. The hydrostatic and hydrodynamic pressure build up differently at different temperature since the fluid density and viscosity vary with the fluid temperature. The piston and the cylinder bore running surface also deform differently at different temperatures, which also affects the fluid behaviors in the piston/cylinder lubricating gap. The fluid temperature is affected by the fluid behaviors in terms of the gap flow and the viscous energy dissipation. In order to simulate this coupled interacting physical phenomena of piston/cylinder lubricating interface, Pelosi proposed a fluid structure and thermal interaction model as mentioned in the state-of-the-art. In Pelosis model, the fluid temperature distribution is calculated based on the energy equation as follow:

$$\rho c_p \mathbf{V} \cdot \nabla T - \nabla \cdot (\kappa \nabla T) = \mu \Phi_D \tag{3.25}$$

On the left side of the energy equation is the convective and diffusive terms, and the energy dissipation rate is on the right side serves as the source term.

As Eq. 3.25 shows, Pelosis fluid temperature model considers convection, the conduction, and the viscous energy dissipation in the fluid domain. However, the

fluid compression and expansion effect is not considered in his model. Figure 4.21 shows the enthalpy-entropy diagram of a type of HLP 32 hydraulic oil. The dashed blue lines are the isothermal lines from 40 Celsius to 75 Celsius and the isobaric lines from 0 bar to 500 bar. According to the figure, an adiabatic compression from 0 bar to 400 bar will increase the fluid temperature by roughly 4 degrees. As discussed in the previous sessions, the pressure spikes in the piston/cylinder lubricating gap can be as high as few thousand bar. The rapid and violent pressure variation in the lubricating gap will results in the fluid temperature variation, then the fluid properties variation. For the same type of fluid that been used to generate the figure 4.21, the viscosity at 400 bar and 50 degrees Celsius is 3.22×10^{-2} pascal seconds, the viscosity at the same pressure and 75 degrees Celsius is 1.37×10^{-2} pascal seconds. A 25 degrees temperature increase results in a 60% decrease on the fluid viscosity.

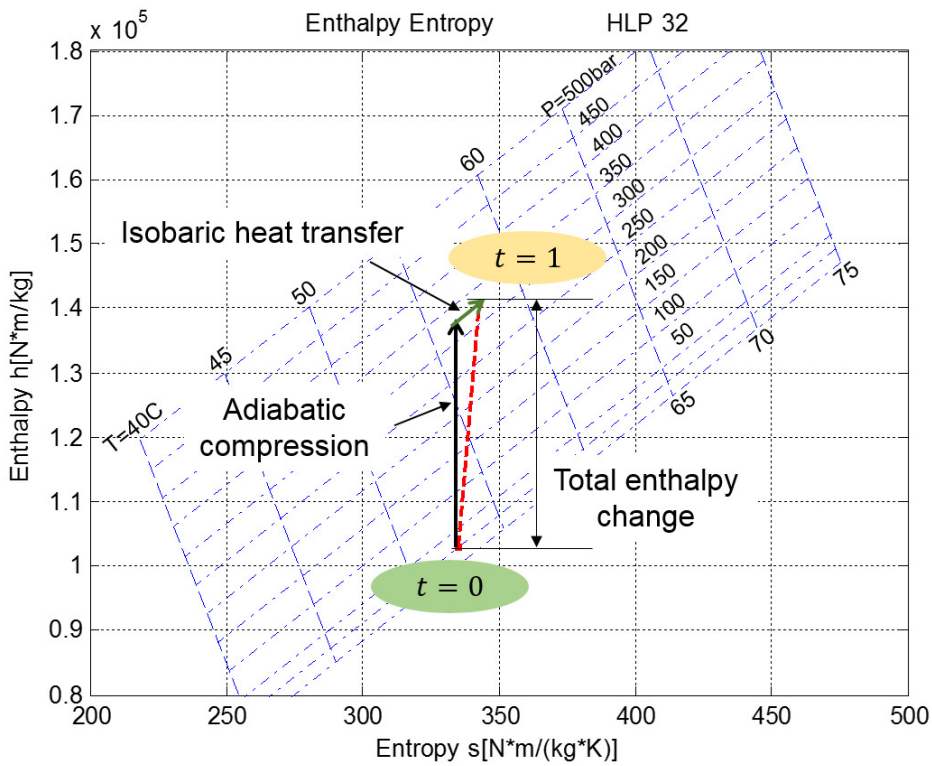

Fig. 3.21. Fluid enthalpy changes over pressure and temperature.

In order to capture the fluid temperature variation due to the compression and expansion in the fluid domain temperature distribution model, enthalpy must be considered as the thermal property of the thermodynamic system. Burton [37] analyzed the thermodynamics of a visco-elastic film under shear and compression. His study combined the first and the second law of thermodynamics. Xu and Sadeghi [38] reported their thermal EHL (elasto-hydrodynamic lubrication) analysis of circular contacts with measured surface roughness. A three-dimensional time dependent non-dimensional energy equation for the lubricating fluid was proposed which includes the local temperature change with respect to time.

In the viscous fluid film of the piston/cylinder interface of the swashplate type axial piston machine, the energy insert into the thermodynamic system not only as work (pressure multiplied by the volume variation in common thermodynamic system) but also as viscous energy dissipation. Also, the energy that pushes the viscous fluid through the lubricating gap is partially from the volumetric variation as described in the Reynolds equation and partially from the pressure differential across the gap. Due to these facts, instead directly implement the enthalpy changing as in the common thermodynamic system between time-steps in the simulation, the enthalpy of the fluid in the control volume is calculated in a two-step process. As Fig. 3.21 shows, the enthalpy changes from time step $t = 0$ to time step $t = 1$ is divided into an adiabatic compression and an isobaric mass and heat transfer process. The governing equation of the proposed thermal model then becomes:

$$H = H_0 + \Delta H|_S + \Delta H|_p \tag{3.26}$$

According to the differential of entropy:

$$ds = \frac{1}{T}dh - \frac{1}{\rho \cdot T}dp \tag{3.27}$$

The isentropic enthalpy differential of pressure yields:

$$\left.\frac{dh}{dp}\right|_s = \frac{1}{\rho} \tag{3.28}$$

Then, the adiabatic enthalpy difference can be written as:

$$\Delta H|_S = m_0 \cdot \frac{p - p_0}{\rho} \tag{3.29}$$

The isobaric enthalpy difference in the control volume controlled by the convection, conduction, and the energy dissipation:

$$\begin{aligned} \Delta H|_p = & \left[\int_V \mu \Phi_D dV + \int_V \left(\rho \mathbf{V} \frac{dh}{dp} \cdot \nabla p \right) dV \right] \cdot dt \\ & + \left[\int_A \left(\kappa \nabla T - \rho c_p \mathbf{V} \cdot T - \rho c_T \mathbf{V} \cdot p \right) \cdot dA \right] \cdot dt \end{aligned} \tag{3.30}$$

The first term of the right side of Eq. 3.30 is the energy dissipation rate due to the viscous shear in the fluid, the second term is the enthalpy difference due to the pressure change of the flow, and the third term is the convection and the conduction. In the third term:

$$\begin{aligned} c_p &= \left. \frac{dh}{dT} \right|_p \\ c_T &= \left. \frac{dh}{dp} \right|_T \end{aligned} \tag{3.31}$$

As Fig. 3.21 shows, the isothermal line and the isobaric line are very linear. Therefore, the two coefficients in Eq. 3.31 are assumed constant in the fluid domain temperature distribution model.

In order to solve the heat transfer problem in the numerical simulation, the fluid domain between the piston and the cylinder bore is discretized to a three-dimensional finite volume grid as shown in Fig. 3.22(a) in Pelosis model. For each three-dimensional finite volume as shown in Fig. 3.22(b), there are six faces labeled t, b, w, e, n, and s separate the volume from its neighbors located at T, B, W, E, N, and S. The mass in the control volume is changing due to the mass flow rate through the faces w, e, n, and s. The fluid velocity on the gap height direction is assumed to be zero. The temperature and the pressure in the control volume are token from the centroid.

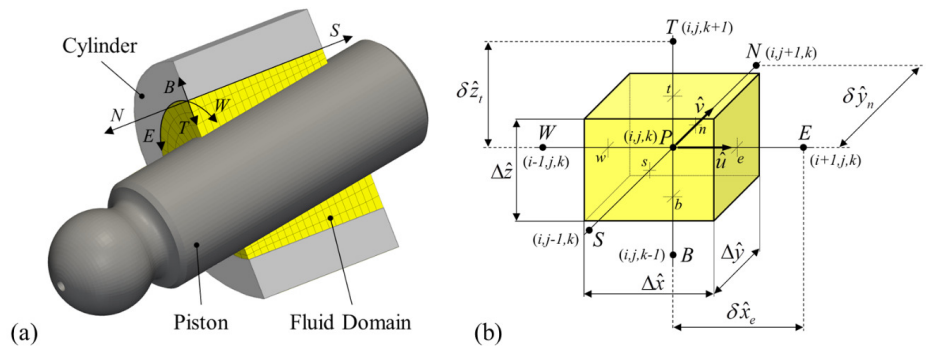

Fig. 3.22. Three-dimensional finite volume structure for fluid domain (a), and the finite volume definition (b) [14]

.

To be used in the finite volume fluid thermal model, the terms in equation 4.30 then can be expressed in the following form:

$$\int_V \mu\Phi_D dV = \mu\Phi_D \Delta x \Delta y \Delta z \tag{3.32}$$

$$\begin{aligned}\int_V \left(\rho \mathbf{V} \frac{dh}{dp} \cdot \nabla p\right) dV &= v_e p_e \Delta y \Delta z_e - v_w p_w \Delta y \Delta z_w \\ &+ v_n p_n \Delta x \Delta z_n - v_s p_s \Delta x \Delta z_s\end{aligned} \tag{3.33}$$

$$\begin{aligned}\int_A (\kappa \nabla T) \cdot dA &= \kappa \frac{T_t - T}{\Delta z} \Delta x \Delta y - \kappa \frac{T - T_b}{\Delta z} \Delta x \Delta y + \kappa \frac{T_e - T}{\Delta x} \Delta y \Delta z_e \\ &- \kappa \frac{T - T_w}{\Delta x} \Delta y \Delta z_w + \kappa \frac{T_n - T}{\Delta y} \Delta x \Delta z_n - \kappa \frac{T - T_s}{\Delta y} \Delta x \Delta z_s\end{aligned} \tag{3.34}$$

$$\begin{aligned}\int_A (\rho c_p \mathbf{V} \cdot T) \cdot dA &= \rho_e c_p v_e T_e \Delta y \Delta z_e - \rho_e c_p v_w T_w \Delta y \Delta z_w \\ &+ \rho_n c_p v_n T_n \Delta x \Delta z_n - \rho_s c_p v_s T_s \Delta x \Delta z_s\end{aligned} \tag{3.35}$$

$$\begin{aligned}\int_A (\rho c_T \mathbf{V} \cdot p) \cdot dA &= \rho_e c_T v_e p_e \Delta y \Delta z_e - \rho_e c_T v_w p_w \Delta y \Delta z_w \\ &+ \rho_n c_T v_n p_n \Delta x \Delta z_n - \rho_s c_T v_s p_s \Delta x \Delta z_s\end{aligned} \tag{3.36}$$

Combining Eq. 3.26, 3.29, 3.30, 3.32, 3.33, 3.34, 3.35 and 3.36 the fluid domain temperature distribution can be calculated through a Gauss-Seidel over-relaxed method. Comparing to the fluid domain temperature distribution calculated using

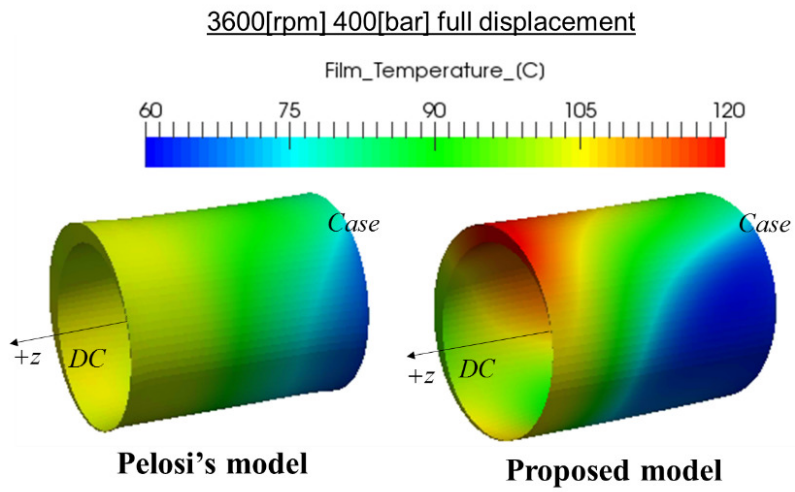

Fig. 3.23. Three dimensional fluid domain temperature distribution comparison.

Pelosis model, as shown on the left side of Fig. 3.23, the fluid temperature calculated from the proposed model distributes more unevenly, as shown on the right side of Fig. 3.23, thanks to the additional consideration of the fluid compression and expansion effect.

3.7 Experimental validation

Everth [39] designed the EHD (elastohydrodynamic) test pump to measure the dynamic pressure and temperature distribution in the operating axial piston machine piston/cylinder interface. The EHD pump is a single piston pump with a standstill single bore cylinder block as shown in Fig. 3.24. The piston is driven by a rotating wobble swashplate to achieve the reciprocating motion. The piston/cylinder interface kinematic and dynamic of the EHD pump is designed to be the same as a type of commercial pump.

There are nine thermocouples welded in the cylinder block located around the bore pointing to the lubricating gap. The tip of each thermocouple is touching the fluid film, and therefore, forming part of the running surface of the cylinder bore. As the unwrapped of the cylinder bore surface shown in Fig. 3.25, the nine thermocouples

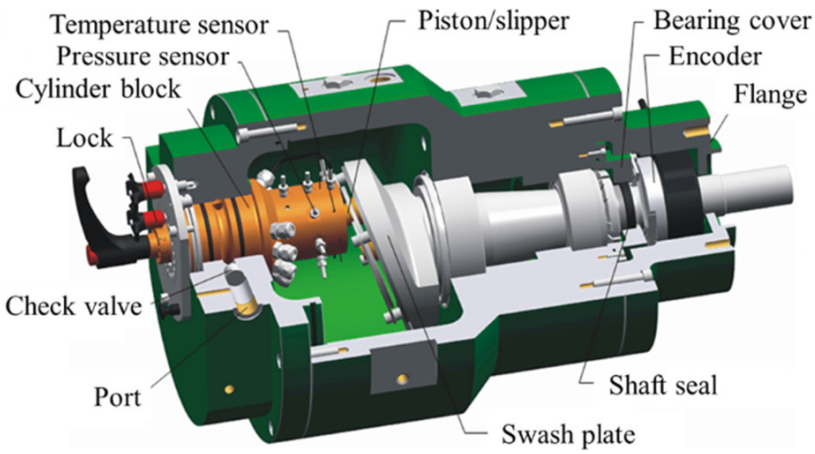

Fig. 3.24. The EHD test pump.

are placed 45 degrees apart angularly, and 2.5mm, 3.0mm, 5.0mm, 8.0mm, 14.33mm, 20.66mm, 23.66mm, 25.66mm, and 26.16mm axially from the displacement chamber end of the cylinder bore running surface. The cylinder block can be rotated and locked at 180 different angular positions 2.0 degrees apart from each other. Therefore, it is possible to measure fluid film temperature distribution on the circumference around the piston at nine different axial positions.

Pelosi and Ivantysynova [22] measured the fluid film temperature distribution of the piston/cylinder interface of the EHD pump at the operating condition shown in Table 3.7. The thermocouple at 3.0mm from the displacement chamber was damaged during the test. The measurement results at rest eight axial positions can be found in Fig. 3.26 to Fig. 3.33. The measured temperature is presented in the figures using black circles.

The fluid film behavior of the piston/cylinder interface of the EHD pump as the operating condition listed in Table 3.7 has been simulated using the proposed piston/cylinder interface model including:

- Pressure distribution calculation considering a backward difference squeeze term in Reynolds equation.
- Improved wall value estimation for fluid property in FVM discrete fluid domain.

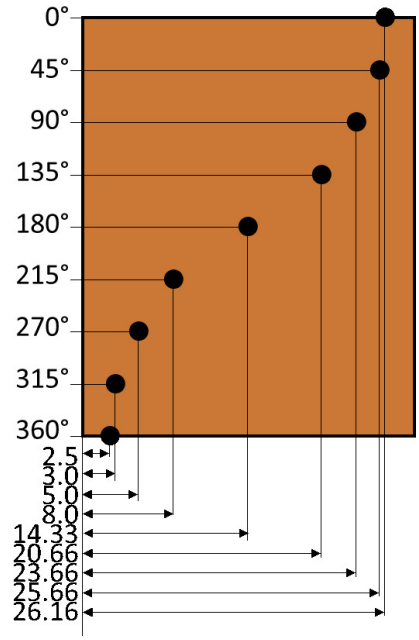

Fig. 3.25. The EHD pump sensor positions.

Table 3.1.
Operating condition for EHD pump temperature distribution measurement.

Shaft speed	1000 [rpm]
Differential Pressure	150 [bar]
Case Temperature	55.0 [°C]
High Pressure Port Temperature	45.0 [°C]
Low Pressure Port Temperature	43.0 [°C]

- Physics-based fluid film thickness on the gap edge.
- Advanced integrated solid body heat transfer model.
- Fluid temperature distribution calculation considering compression and expansion.

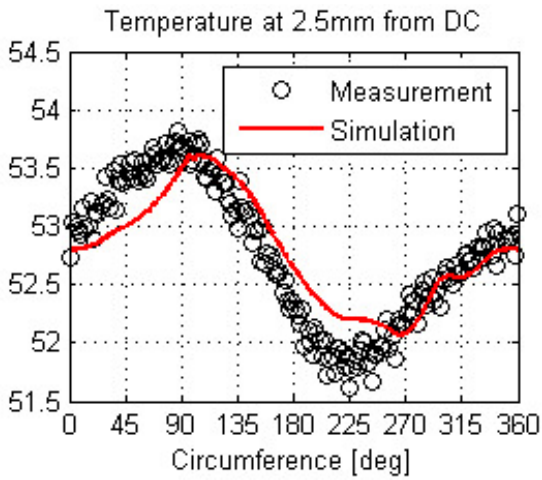

Fig. 3.26. EHD measurement vs. simulation at 2.5mm from D.C..

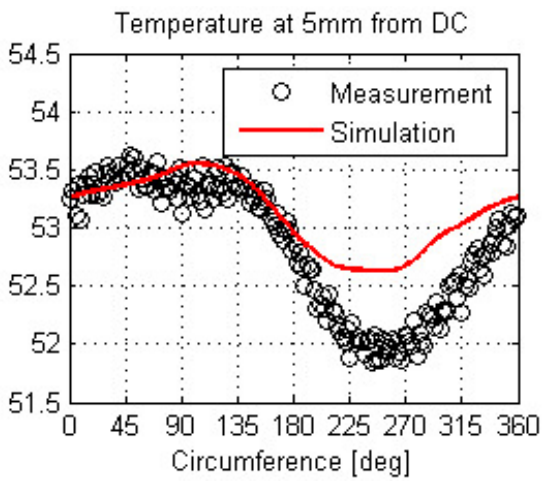

Fig. 3.27. EHD measurement vs. simulation at 5.0mm from D.C..

The simulated EHD pump cylinder bore running surface temperature distribution is compared to the measurement as shown in Fig. 3.26 to Fig. 3.33. The inclination of the piston causes the film thickness around both ends of the gap lower than the middle region. The lower film thickness contributes to higher energy dissipation, therefore higher localized temperature in the gap. As Fig. 3.26 to Fig. 3.33 show, the temperature distributes more evenly in the center section of the cylinder bore, and has more variation around both the displacement chamber end and the case end. As the figures show, the proposed piston/cylinder interface model is able to capture the

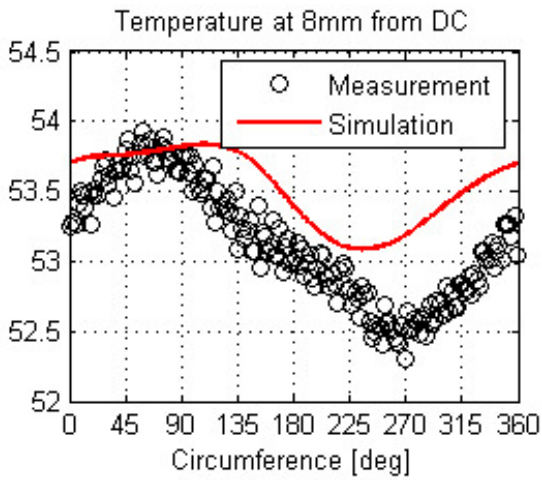

Fig. 3.28. EHD measurement vs. simulation at 8.0mm from D.C..

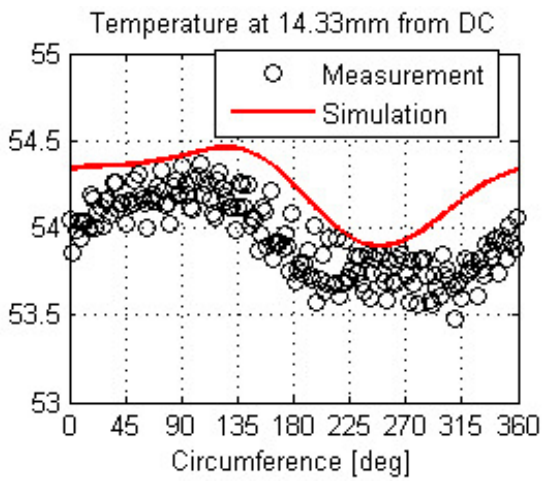

Fig. 3.29. EHD measurement vs. simulation at 14.33mm from D.C..

character of the temperature distribution on the cylinder bore running surface. The accurate cylinder bore running surface temperature distribution requires an accurate simulation of the non-isothermal elasto-hydrodynamic fluid film behaviors simulation with an accurate solid body heat transfer and thermal deformation model. Hence, according to the comparison results presented from Fig. 3.26 to Fig. 3.33, the accuracy of the proposed piston/cylinder interface is verified.

In order to further understand the impact of the proposed implementation mentioned previously on the accuracy of the piston/cylinder interface model accuracy, a

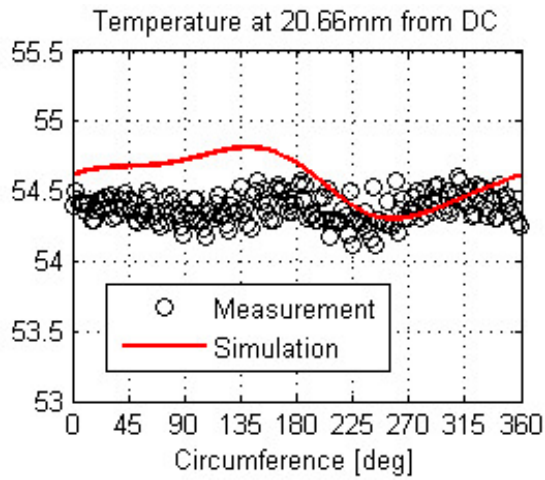

Fig. 3.30. EHD measurement vs. simulation at 20.66mm from D.C..

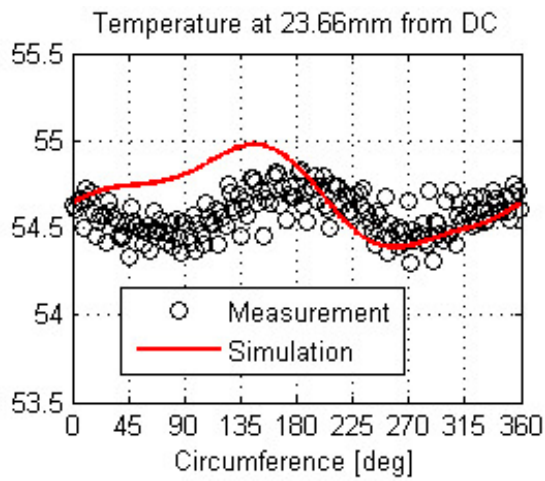

Fig. 3.31. EHD measurement vs. simulation at 23.06mm from D.C..

series of simulation is conducted using Pelosi's base model and the proposed model with partially implemented features, as the following list.

Sim 1 Pelosi's base model

Sim 2 the NG model without the improved wall value estimation for fluid property in FVM discrete fluid domain and the physics-based fluid film thickness on the gap edge.

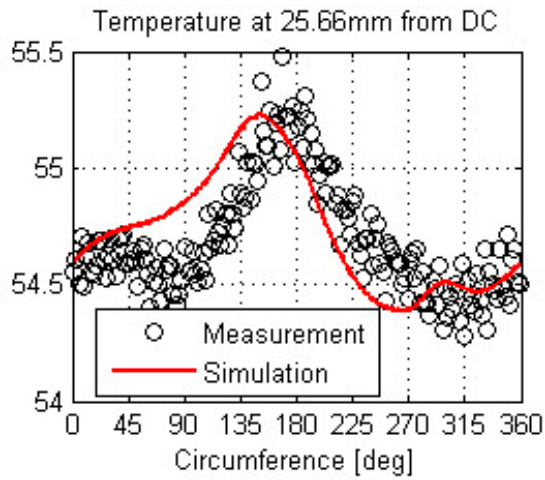

Fig. 3.32. EHD measurement vs. simulation at 25.66mm from D.C..

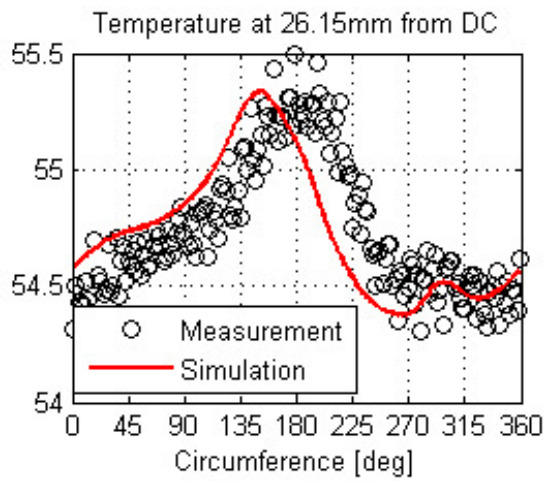

Fig. 3.33. EHD measurement vs. simulation at 26.61mm from D.C..

Sim 3 the NG model without the fluid temperature distribution calculation considering compression and expansion.

NG the fully implemented next-generation piston/cylinder interface model (Proposed model).

As discussed before, the temperature distribution at the case and displacement chamber ends show more variation along the circumference. Therefore, two axial locations are chosen to demonstrate the accuracy of the proposed model and its

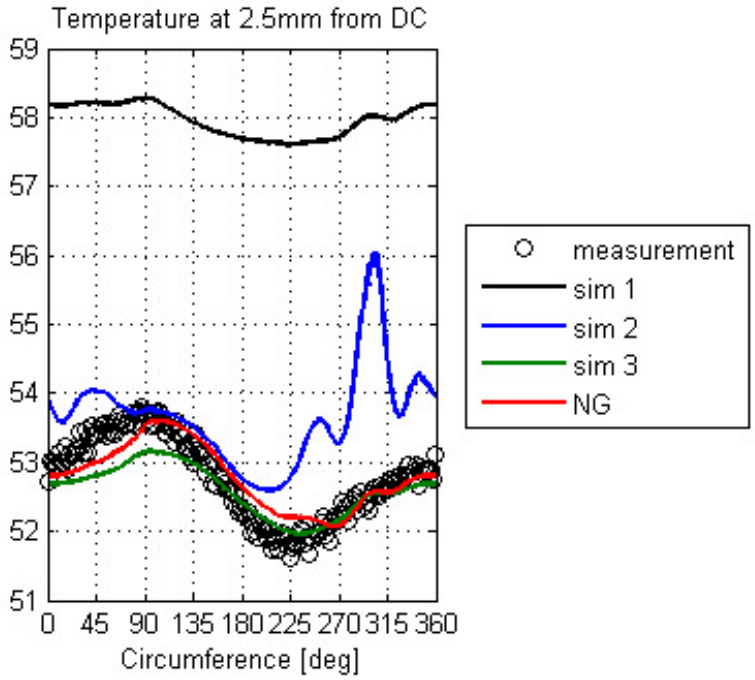

Fig. 3.34. EHD measurement vs. simulation at 2.5mm from D.C..

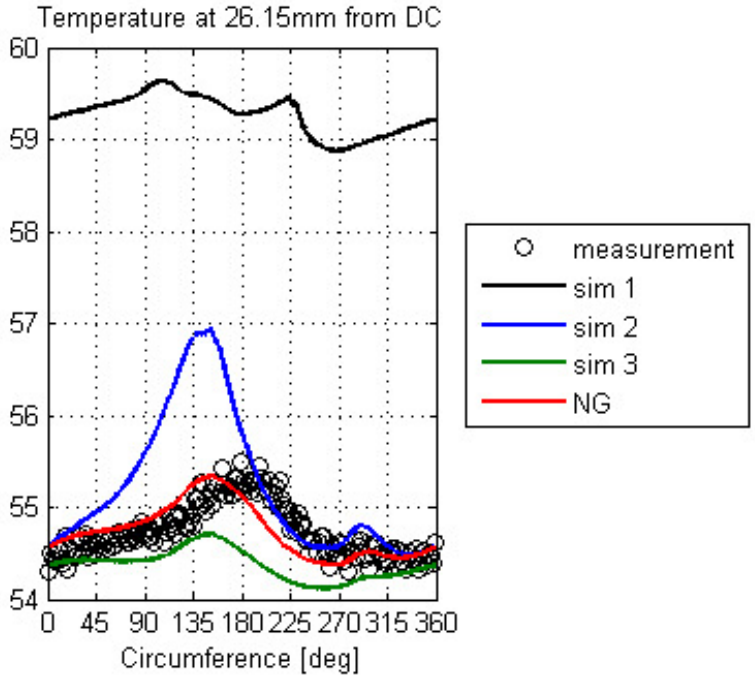

Fig. 3.35. EHD measurement vs. simulation at 26.61mm from D.C..

comparisons, where are 2.5 mm from the displacement chamber end and 2.5 mm from the case end (26.15 mm from D.C.).

As Fig. 3.34 and Fig. 3.35 show, Sim 1, which is Pelosi's base model predicts the temperature very different from the real-life measurement. The main reason is that the conventional heat transfer model mentioned in section 3.5 suffers from the instability. In order to achieve the thermal convergence, the heat flux from the fluid domain to both solid bodies are artificially saturated, therefore, causes an unrealistic solid body temperature prediction. This inaccuracy is able to be eliminated by using the advanced integrated solid body heat transfer model as mentioned in section 3.5. Another reason for the over-estimated temperature distribution from Sim 1 is due to its failure to accurately calculate the pressure distribution in the gap especially at where the film thickness is low. The consequence is that the logic behind the force balance loop put the piston closer to the cylinder bore and the energy dissipation is over-calculated, as previously discussed in section 3.2. This inaccuracy is eliminated in the proposed model by using the pressure distribution calculation considering a backward difference squeeze term in the Reynolds equation as presented in section 3.2.

Sim 2 uses the proposed piston/cylinder interface model without the improved wall value estimation for fluid property in FVM discrete fluid domain as presented in section 3.3 and the physics-based fluid film thickness on the gap edge in section 3.4. As discussed in these two sections, both new implementations on pressure distribution calculation reduce the unrealistic pressure spikes due to numerical limitations. As Fig. 3.34 and Fig. 3.35 show, without these two implementations, the unrealistic pressure spikes generates localized high heat flux, which then contributes to the unrealistic temperature distribution on the cylinder bore running surface.

Sim 3 uses the proposed piston/cylinder interface model without the fluid temperature distribution model considering compression and expansion. As Fig. 3.34 and Fig. 3.35 show, Sim 3 under-predicts the temperature distribution on the cylinder bore running surface. This is because that the temperature variation due to the compression and expansion effects are not considered in the conventional fluid domain

heat transfer model. The proposed piston/cylinder interface model decomposes the temperature variation in the fluid into two steps, an adiabatic pressure change process and an isobaric heat generation and heat transfer process. As the comparison shows, the proposed fluid temperature distribution model considering compression and expansion is able to improve the accuracy of the piston/cylinder interface simulation.

In summary, Fig. 3.26 to Fig. 3.33 present a comprehensive simulation verse measurement comparison study. The proposed next-generation piston/cylinder interface model is validated against the measurement for the temperature at 2880 different locations on the cylinder bore running surface. Fig. 3.34 and Fig. 3.35 then demonstrate how significant the influence of the implementations proposed in this chapter on model accuracy.

3.8 Conclusion

In this chapter, a proposed next-generation piston/cylinder interface simulation model is proposed, which advances over the previous generation model at the following points:

- A backward difference squeeze term in the Reynolds equation.
- Improved FVM fluid domain discretion scheme.
- Physics-based boundaries for fluid film thickness.
- Advanced integrated solid body heat transfer model. [40]
- Heat transfer model for compressible fluid.. [41]

The physics behind each point and its implementation in the simulation is described in detail in separate sections. The accuracy of the proposed model is verified with the measurement by comparing the temperature distribution on the cylinder bore running surface against the measured data obtained from a specially designed elasto-hydrodynamic (EHD) pump. The significance of the implementation proposed

in this chapter is also demonstrated by comparing multiple partially implemented model to the measurement.

4. THERMAL BOUNDARIES PREDICTION MODEL

For the simulations of existing pumps or motors, the essential port and case temperatures are set based on the pump flow temperatures obtained from steady-state measurements. However, in order to achieve the goal of understanding the performance of a scaled swash plate type axial piston machine, the ability to conduct the simulation studies without the support of the measurement is required. Therefore, a tool that predicts the port and drain flow temperatures solely from the unit design is demanded. A case flow temperature prediction model was proposed by Grönberg [42]. This model was further developed by Zecchi et al. [43]. A drawback of this model is its sensitivity to user's inputs, especially to the heat transfer area and the heat transfer coefficients. The goal of this chapter is to develop a robust and accurate port and case temperatures prediction model that can provide reliable thermal boundaries to the three-dimensional multi-domain heat transfer model for the three lubricating interfaces.

In this chapter, the scheme of the proposed thermal boundaries prediction model as well as the governing physics are explained. The model is validated through a comparison study between the simulated temperature and the measurement over three hundred combinations of different units and different operation conditions.

4.1 Introduction to the thermal boundaries

The most recent simulation methodology for all three lubricating interfaces of swash plate type axial piston machine (piston/cylinder, cylinder block/valve plate, and slipper/swashplate) described in the previous chapters requires the temperatures in the port volume and the case volume as the essential thermal boundaries. These temperatures are not only used to calculate the three-dimensional temperature distri-

bution not only in fluid domain but also in the solid bodies. The solid body temperature distribution serves as a thermal load causes thermal deflections on the running surface of the solid parts and further impacts the lubricating interfaces performance.

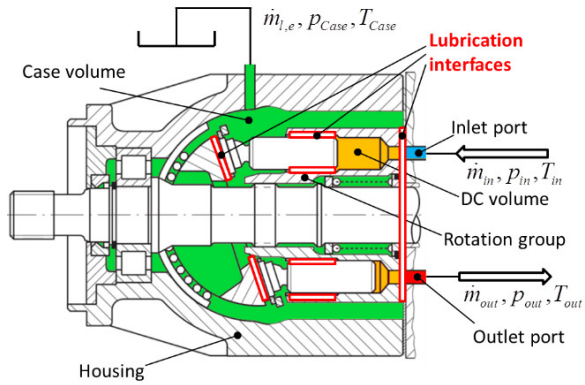

Fig. 4.1. Definition of the control volumes in swashplate type axial piston machines

Fig. 4.1 is a cross-section of a swash type axial piston machine. The location of the three main lubricating interfaces together with the inlet port volume, output port volume, and the case volume are shown in this figure. The fluid flow temperature in the inlet port volume is defined by the operating condition, while the case flow temperature and the outlet flow temperature are dependent on many other factors including the expansion of compression of the working fluid, the energy dissipation in all the power loss sources of the machine, and the heat transfer of both fluid and solid domain. In order to demonstrate the sensitivity of these ports temperatures on simulated the unit performance, three sets of temperatures (HT, MT, and LT) are chosen and used as thermal boundaries of the simulation study on a commercial axial piston machine. The three sets of temperatures (HT, MT, and LT) are shown in Table. 4.1.

Fig. 4.2 shows the simulated power loss and leakage flow rate of each lubricating interface and the whole unit for these three sets of temperatures. This figure illustrates that the outlet flow temperature and case flow temperature have a significant influence on the simulated performance and efficiency of each lubricating interface.

Table 4.1.
Operating temperatures of HT, MT, and LT

		HT	MT	LT
inlet temperature	[°C]	52.4	52.4	52.4
outlet temperature	[°C]	70	60.5	52.4
case temperature	[°C]	100	79.4	52.4

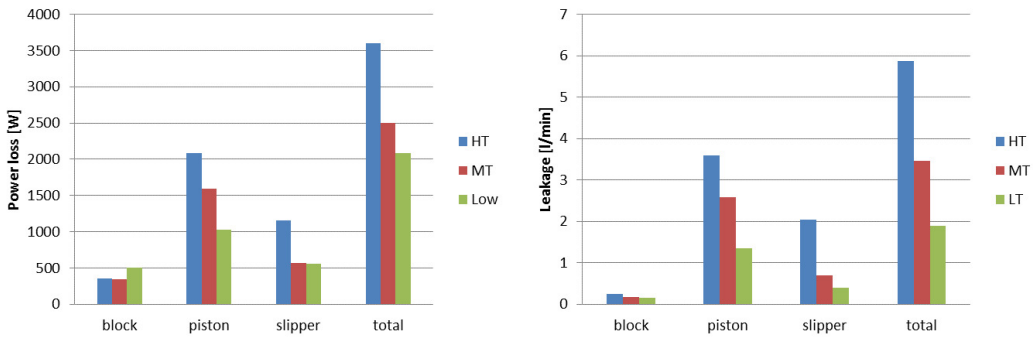

Fig. 4.2. Simulation results for HT, MT, and LT.

Fig. 4.3 shows a schematic of the heat and mass transfer in an axial piston machine. The fluid domain is divided into four control volumes, namely the inlet port volume, the outlet port volume, the displacement chamber (D.C.) volume, and the case volume. These four control volumes, which are isolated by the three lubricating interfaces, hold different fluid pressures due to the sealing function of the interfaces. The pressure in the inlet port volume and the outlet port are the inlet pressure and the outlet pressure respectively. The pressure in the displacement chamber, however, dynamically changes according to the connection between the chamber and the inlet or outlet port. The fluid pressure in the case volume is control by the drain line pressure.

Most of the inlet flow eventually leaves the machine through the outlet port. A small portion of the inlet flow leaves the machine through the case volume as external leakage flow. The cross porting happens in many valve plate designs allowing the

displacement chamber to connect both inlet and outlet port simultaneously in a very short period to avoid the pressure jump and the cavitation. The additional mass flow from the outlet port through the displacement chamber into inlet port due to the cross porting circulates inside of the machine, therefore, is called internal leakage.

The heat exchanges across different domains due to the temperature difference. The heat transfers between the solid bodies and the displacement chamber, between the solid bodies and the case volume, between the case volume and the housing, and between the housing and the ambient (both convection and radiation). Due to

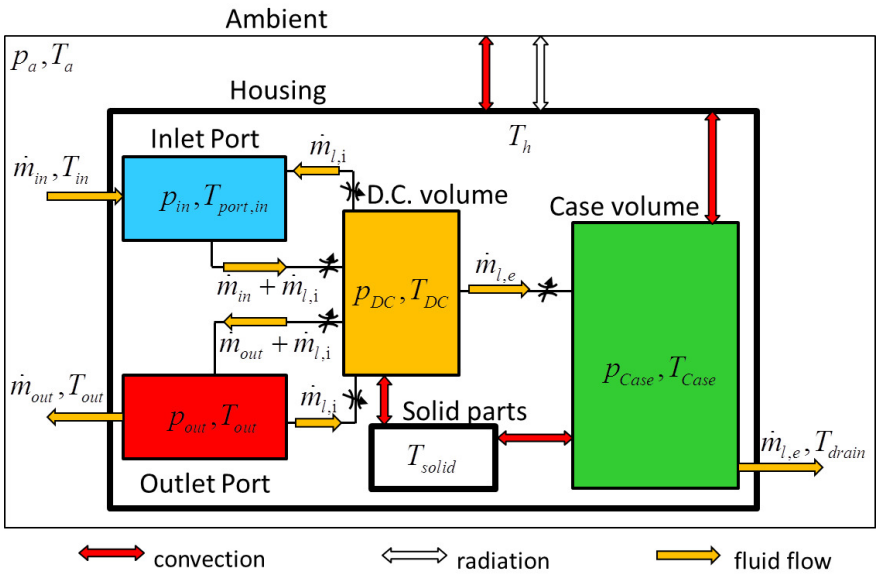

Fig. 4.3. Schematic of the heat and mass transfer in axial piston machines.

the low flow rate, the internal leakage has limited influence on the port and case flow temperature. Hence, in order to simplify the heat transfer model between the fluid and solid domain, the heat and mass transfer due to the cross porting internal leakage is neglected. Also, by neglecting the internal leakage, the inlet port volume and the outlet port volume can be simplified as two orifices. The radiation between the housing and the ambient is also ignored due to the limited influence on the temperature calculation. The external housing is assumed to be the same as the case fluid temperature.

With all of the simplifications mentioned above, the schematic of the heat and mass transfer in the axial piston machine become as Fig. 4.4.

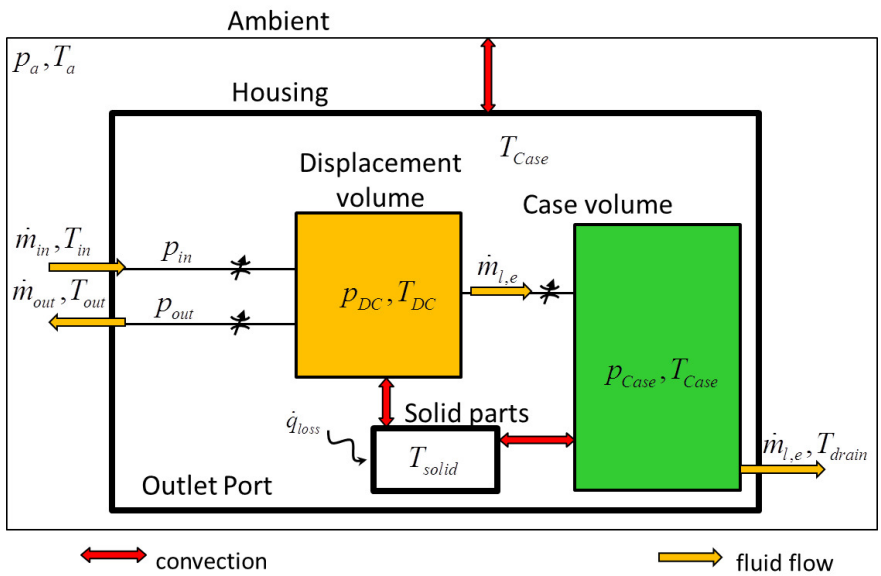

Fig. 4.4. Simplified schematic of the heat and mass transfer in in axial piston machines.

Besides of the heat transfer, the compression and the expansion also impact on the fluid temperature. The most noticeable compression and expansion happen in the displacement chamber when the chamber pressure shifts between the inlet pressure and the outlet pressure. An enthalpy-entropy diagram in Fig. 4.5 shows an example of a compression process in the displacement chamber during a discharge stroke in the pumping mode. The compression process can be decoupled into two processes. The black vertical vector represents the enthalpy change in adiabatic compression. The green vector follows the adiabatic compression vector stands for the isobaric temperature changes due to the heat and mass transfer and the energy dissipation in the lubricating gap. The proposed temperatures prediction model for the port and drain flow calculates the temperature change due to the expansion/compression and heat transfer separately.

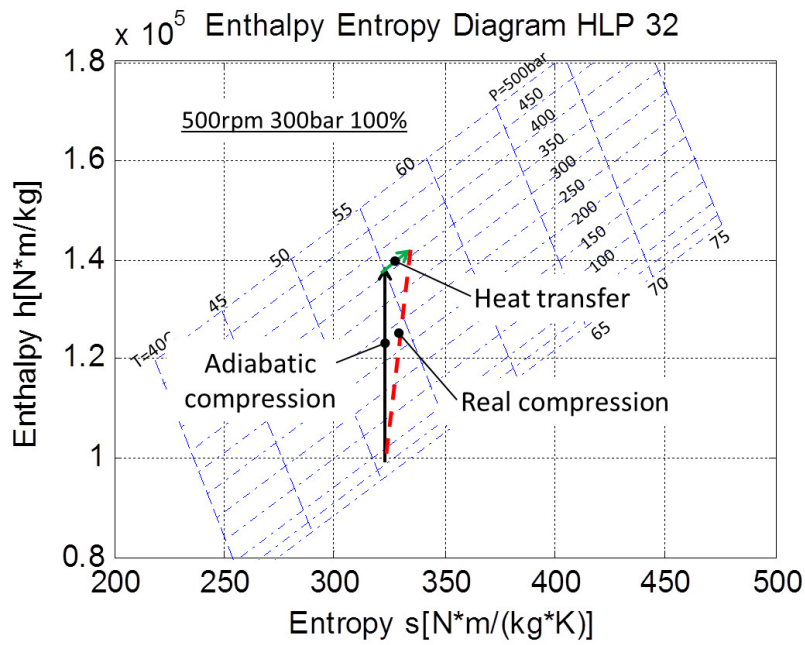

Fig. 4.5. An example compression process in the displacement chamber volume.

4.2 Temperature change via adiabatic compression and expansion

The enthalpy change in the adiabatic compression/expansion process is calculate while holding the entropy. Both the specific enthalpy and the specific entropy of compressible fluid are functions of temperature and pressure:

$$\begin{aligned} h &= h(T,p) \\ s &= s(T,p) \end{aligned} \tag{4.1}$$

The differential of the specific enthalpy and entropy yield to:

$$\begin{aligned} dh &= \left(\frac{\partial h}{\partial T}\right)_p \cdot dT + \left(\frac{\partial h}{\partial p}\right)_T \cdot dp \\ ds &= \left(\frac{\partial s}{\partial T}\right)_p \cdot dT + \left(\frac{\partial s}{\partial p}\right)_T \cdot dp \end{aligned} \tag{4.2}$$

The derivations of the caloric constitutive equations yields:

$$c_p = \left(\frac{\partial h}{\partial T}\right)_p \tag{4.3}$$

Using the Maxwell relation:

$$ds = \left(\frac{\partial s}{\partial T}\right)_p \cdot dT - \left(\frac{\partial v_{fluid}}{\partial T}\right)_p \cdot dp \tag{4.4}$$

where v_{fluid} is the specific volume of the fluid. Substituting dh and ds into $ds = T \cdot ds + v_{fluid} \cdot dp$

$$\left[\left(\frac{\partial h}{\partial p}\right)_T + T\left(\frac{\partial v_{fluid}}{\partial T}\right)_p - v_{fluid}\right] dp = \left[T\left(\frac{\partial s}{\partial T}\right)_p - \left(\frac{\partial h}{\partial T}\right)_p\right] dT \tag{4.5}$$

At constant temperature:

$$\begin{aligned} \left[\left(\frac{\partial h}{\partial p}\right)_T + T\left(\frac{\partial v}{\partial T}\right)_p - v_{fluid}\right] dp = 0 \\ \left(\frac{\partial h}{\partial p}\right)_T = v_{fluid} - T\left(\frac{\partial v_{fluid}}{\partial T}\right)_p \end{aligned} \tag{4.6}$$

At constant pressure:

$$\begin{aligned} 0 = \left[T\left(\frac{\partial s}{\partial T}\right)_p - \left(\frac{\partial h}{\partial T}\right)_p\right] dT \\ \left(\frac{\partial s}{\partial T}\right)_p = \frac{1}{T}\left(\frac{\partial h}{\partial T}\right)_p = \frac{1}{T} c_p \end{aligned} \tag{4.7}$$

Applied Eq. 4.3 and Eq. 4.6 to Eq. 4.2:

$$dh = c_p \cdot dT + \left(v_{fluid} - T \cdot \left(\frac{\partial v_{fluid}}{\partial T}\right)_p\right) \cdot dp \tag{4.8}$$

Applied Eq. 4.7 to Eq. 4.4:

$$ds = c_p \cdot \frac{dT}{T} - \left(\frac{\partial v_{fluid}}{\partial T}\right)_p \cdot dp \tag{4.9}$$

Integrating Eq. 4.8 and Eq. 4.9 at $T_o$andp_o:

$$\begin{aligned} h = h_o\left(T_o\right) + \int_{T_o}^{T} c_p \cdot dT + \int_{p_0}^{p} v \cdot dp - \int_{p_0}^{p} T \cdot \left(\frac{\partial v_{fluid}}{\partial T}\right)_p \cdot dp \\ s = s_o\left(T_o\right) + \int_{T_o}^{T} \frac{c_p}{T} \cdot dT - \int_{p_0}^{p} \left(\frac{\partial v_{fluid}}{\partial T}\right)_p \cdot dp \end{aligned} \tag{4.10}$$

Based on the adiabatic compression assumption, the entropy of the fluid before and after the compression or the expansion is the same:

$$s_1 = s_2$$
$$\int_{T_o}^{T_1} \frac{c_p}{T} \cdot dT - \int_{p_0}^{p_1} \left(\frac{\partial v_{fluid}}{\partial T} \right)_p \cdot dp = \int_{T_o}^{T_2} \frac{c_p}{T} \cdot dT - \int_{p_0}^{p_2} \left(\frac{\partial v_{fluid}}{\partial T} \right)_p \cdot dp \tag{4.11}$$

The temperature of the fluid after the adiabatic compression or expansion in both displacement and case volume T_{adia_DC} and T_{adia_Case} can be solved by using Eq. 4.11.

4.3 Temperature change via heat transfer

The heat transfer process in the axial piston machine presented in Fig. 4.4 is further simplified into a symbolized three-volume model which includes a displacement chamber volume, a solid parts volume, and a case volume as shown in Fig. 4.6. The energy dissipation rate due to the viscous friction is retro-proportional to the gap height. The majority of the viscous friction power dissipates into heat in the gap area where the minimum film thickness occurs. Because of the low film thickness, this dissipated heat transfers into the solid bodies directly as conduction instead of into case volume through convection. Therefore, the total power loss of the axial piston machine is considered as a heat source which provides a rate of heat flux directly into the solid parts volume. The power leaves the unit through two paths: either transfers into the displacement chamber, then leaves the unit with the outlet flow; or transfers in the case volume then leaves the machine with the drain flow or the natural convection of the external housing surface.

The energy dissipation in the lubricating interfaces leaves solid parts in two ways:

$$\dot{q}_{loss} = \dot{q}_{s\_DC} + \dot{q}_{s\_Case} \tag{4.12}$$

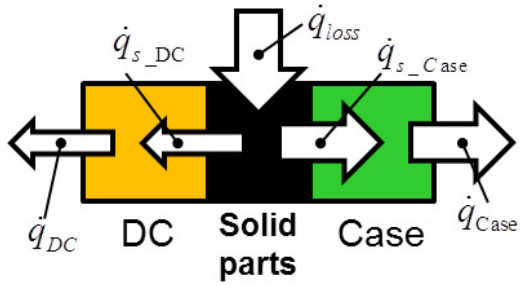

Fig. 4.6. Simplified three-volume scheme for heat transfer.

The energy conservation is applied in the displacement chamber volume and the case volume due to the steady-state condition. Therefore,

$$\begin{aligned} \dot{q}_{DC} &= \dot{q}_{s\_DC} \\ \dot{q}_{Case} &= \dot{q}_{s\_Case} \end{aligned} \tag{4.13}$$

where T_{adia_dc} is the fluid temperature after adiabatic compression or expansion in the displacement chamber volume calculated in the compression/expansion process.

The rate of energy leaving the case volume with the case flow rate or the natural convection is calculated from the case mass flow rate, temperature differential, fluid specific heat capacity, the air temperature and the overall natural heat transfer coefficient of the external housing surface:

$$\dot{q}_{Case} = \dot{m}_{Case} \cdot \int_{T_{adia\_Case}}^{T_{Case}} c_p dT + k_{natural} \cdot (T_{Case} - T_{air}) \tag{4.14}$$

where T_{adia_case} is the fluid temperature after adiabatic compression in case volume calculated in the thermodynamic module, $k_{natural}$ is the overall natural convection coefficient of the pump housing surface.

The value of $k_{natural}$ is proportional to the housing surface which is proportional to the second order of the linear scaling factor:

$$k_{natural} = C_{natrual\_ref} \cdot \lambda^2 \tag{4.15}$$

where $C_{natural\_ref}$ is a constant value determined based on steady-state measurements of a baseline unit. The scaling factor is used to generalize of the model.

The linear scaling factor can be obtained as:

$$\lambda = \sqrt[3]{\frac{V_i}{V_{i\_baseline}}} \tag{4.16}$$

where V_i is the displacement volume of the pump or motor under investigation.

The rate of energy from solid parts to both the displacement chamber volume and the case volume can be calculated as:

$$\begin{aligned} \dot{q}_{s\_DC} &= k_{DC} \cdot (T_{solid} - T_{DC}) \\ \dot{q}_{s\_Case} &= k_{Case} \cdot (T_{solid} - T_{Case}) \end{aligned} \tag{4.17}$$

where k_{DC} and k_{Case} are the overall heat transfer coefficients of the displacement chamber surface and the case volume surface, T_{DC} is the temperature in the displacement chamber which approximately equals to the average of the inlet flow temperature and the outlet flow temperature.

The value of k_{DC} is a function of outlet flow rate and the linear scaling factor:

$$k_{DC} = \left(\frac{Q_{out}}{\lambda}\right)^{0.4} \cdot \lambda^2 \cdot C_{DC\_ref} \tag{4.18}$$

where C_{DC_ref} is a constant value determined based on the steady state measurement, the scaling reference, and fluid properties. The term $\frac{Q_{out}}{\lambda}$ scales the overall heat transfer coefficient with Reynolds number; the order value 0.4 is found that match the measurements the best, and the term λ^2 scales the overall heat transfer coefficient with the heat transfer surface area.

The value of k_{case} is a function of the pump speed, the leakage flow rate correction factor (lcf) and the linear scaling factor:

$$k_{Case} = \left(n \cdot \lambda^2 \cdot lcf\right)^{0.4} \cdot \lambda^2 \cdot C_{Case\_ref} \tag{4.19}$$

where C_{Case_ref} is a constant value determined based on the steady state measurement, the scaling reference, and fluid property. The term $n \cdot \lambda^2 \cdot lcf$ scales the overall heat transfer coefficient with Reynolds number; the order value 0.4 is found that match the measurements the best, and the term λ^2 scales the overall heat transfer coefficient

with the heat transfer surface area. lcf is leakage flow rate correction factor which is a function of the pump speed, the case flow rate and the linear scaling factor:

$$lcf = \frac{\sqrt{\left(\frac{n}{C_{lcf}} \cdot \lambda\right)^2 + \left(\frac{Q_{case}}{\lambda^2}\right)^2}}{\frac{n}{C_{lcf}} \cdot \lambda} \tag{4.20}$$

where C_{lcf} is a constant value based on the scaling reference. This leakage flow correction factor corrects the overall case heat transfer coefficient based on the leakage flow rate.

The heat transfer model requires four heat transfer constants $C_{natural\_ref}$, C_{DC_ref}, C_{Case_ref} and C_{lcf}. C_{lcf} is determined from the geometry of the pump:

$$C_{lcf} = \frac{\pi \cdot A_{block} \cdot t}{2} \tag{4.21}$$

where A_{block} represents cylinder block outer surface area and t is the distance between the cylinder block outer surface and the housing inner surface.

$C_{natural\_ref}$ is determined from the geometry of the pump and the air-metal natural convection heat transfer coefficient of the outer housing surface:

$$C_{natural\_ref} = h_{c\_air} \cdot A_{hou\sin g} \tag{4.22}$$

where h_{c_air} is a the air-metal natural convection heat transfer coefficient and $A_{hou\sin g}$ is the outer housing surface area.

C_{DC_ref} and C_{Case_ref} is found by conducting optimization on the discrepancies between the simulated pump flow temperatures and the steady state measured pump flow temperatures.

Those resulting constants can be used for any given size of a pump or motor by using the linear scaling law.

To conclude the balance of the rate of energy in the heat transfer model:

$$\begin{aligned}
\dot{q}_{s_DC} &= \dot{q}_{s_DC}\left(T_{solid}, T_{out}\right) \\
\dot{q}_{s_Case} &= \dot{q}_{s_Case}\left(T_{solid}, T_{Case}\right) \\
\dot{q}_{DC} &= \dot{q}_{DC}\left(T_{solid}, T_{out}\right) \\
\dot{q}_{Case} &= \dot{q}_{Case}\left(T_{solid}, T_{Case}\right)
\end{aligned} \tag{4.23}$$

There are three energy rate balance equations:

$$\begin{aligned} \dot{q}_{loss} &= \dot{q}_{s\_DC} + \dot{q}_{s\_Case} \\ \dot{q}_{DC} &= \dot{q}_{s\_DC} \\ \dot{q}_{Case} &= \dot{q}_{s\_Case} \end{aligned} \tag{4.24}$$

with three unknowns T_{out}, T_{Case} and T_{solid}.

4.4 Structure of thermal boundaries prediction model

The temperatures prediction model for port and drain flow is a combination of the two modules as shown in Fig. 4.7: the thermodynamic module, and the heat transfer module. The thermodynamic module calculates the temperature change due to adiabatic compression/expansion, while the heat transfer module calculates the temperature change due to heat transferring at constant pressure.

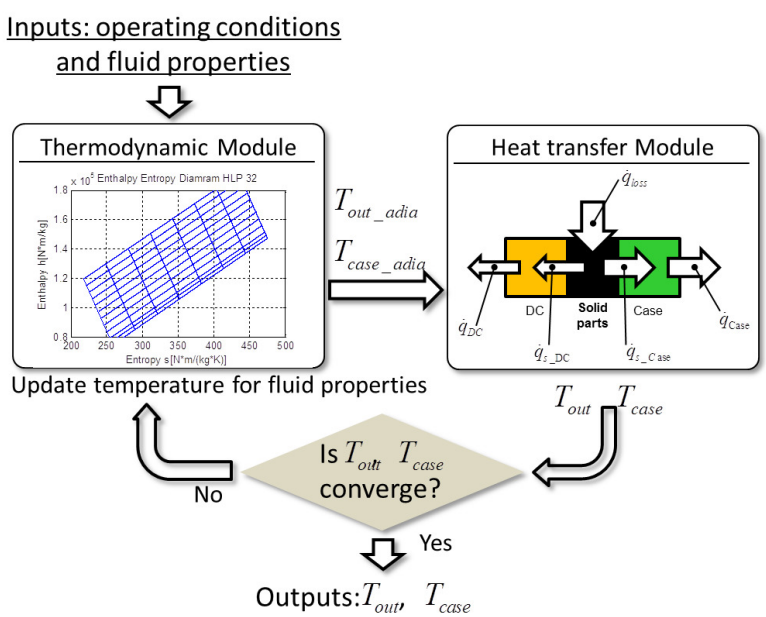

Fig. 4.7. Pump flow temperatures prediction model solution scheme.

In the thermodynamic module, the outlet flow temperature and case flow temperature due to adiabatic pressure change is calculated with the given operating condition

and the fluid properties. The heat transfer module then corrects the outlet and case flow temperature with the given power loss. Table 4.2 summarizes the required fluid properties which are functions of temperature, therefore, need to be updated with the latest calculated port and case flow temperatures. This iterative loop continues until the outlet and case flow temperature converges.

Table 4.2.
Required fluid properties.

Fluid Properties		**Comments**
density	ρ	function of pressure and temperature
specific heat capacity	c_p	function of temperature

4.5 Multi-physics multi-domain model

In this section, a multi-physcis multi-domain swashplate axial piston machine performance prediction model is proposed as shown in Fig. 4.8. Thanks to the previously mentioned port and drain flow prediction model, the thermal boundaries for the multi-domain heat transfer model of the three lubricating interfaces can be obtained without steady-state measurements.

The input parameters that are required to calculate the port and drain flow temperatures are listed in Table 4.3. The pump size, the pump speed, the inlet/outlet/case pressure, the inlet flow temperature, and the ambient temperature are given with the design and known without simulation. The outlet flow rate, the drain flow rate, and the total power loss are unknown, and needed to be obtained from other models.

The outlet flow rate, the drain flow rate, and the total power loss depend on the performance and the efficiency of unit, therefore can to be simulated using the fluid structure and thermal interaction model for the three lubricating interfaces as

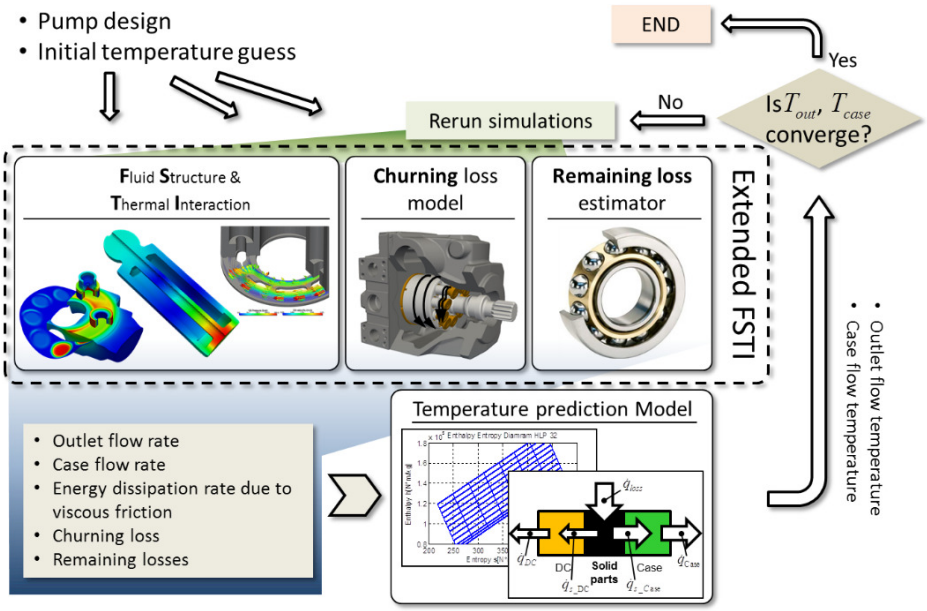

Fig. 4.8. An multi-physics multi-domain model to predict swashplate type axial piston machine performance.

mentioned in the previous chapter together with a churning loss model and the estimated bearing and sealing losses. Since the calculation of the lubricating interface performance needs the port and case flow temperature as the thermal boundaries, an iterative method is required and shown in Fig. 4.8.

As shown in Fig. 4.8, the efficiency lubricating interfaces together with the churning, sealing, and bearing losses (Together labeled as extended FSTI) are conducted with an initial guessed thermal boundaries. The simulated energy dissipation rate and leakage flow rate from the three lubricating interfaces from the fluid structure and thermal interaction model, combining with the estimated churning loss and the remaining losses in the bearing and sealing, serve as the input parameters of the port and drain flow temperature prediction model. The calculated outlet flow temperature and drain flow are then used as the thermal boundaries in the lubricating interface model. The iterative loop keep running until the port and drain flow temperatures converges.

Table 4.3.
Required operating conditions.

Required inputs		**Comments**
Pump size	V_i	Known
Pump speed	n	Known
Inlet pressure	p_{in}	Known
Outlet pressure	p_{out}	Known
Case pressure	p_{Case}	Known
Inlet temperature	T_{in}	Known
Ambient temperature	T_{air}	Known
Outlet flow rate	Q_{out}	Unknown
Drain flow rate	Q_{Case}	Unknown
Power loss	$\dot{q}_{loss}$	Unknown

4.6 Model validation

Before utilizing this temperature prediction model in the scaling study, a large amount of simulation/measurement comparison studies are conducted for the validation purpose. As shown in Table 4.4, these comparison studies include four different sizes, two different types of fluid, and many different displacements, pump speeds, and pressure differences.

Fluid type I and fluid type II in Table 4.4 have different fluid properties. Fig. 4.9 illustrates the density and specific isobar heat capacity of this two type of fluid.

For the comparison studies, in order to focus on examining the accuracy of the temperature prediction model only, the power loss is calculated from the measurement data instead of the lubricating gap model. The power loss is calculated according to the following equation:

$$\dot{q}_{loss} = \dot{m}_{out} \cdot c_p \cdot (T_{out} - T_{out\_adia}) + \dot{m}_{l,e} \cdot c_p \cdot (T_{case} - T_{case\_adia}) \tag{4.25}$$

Table 4.4.
Operating conditions of the comparison study.

Set #	fluid	size	displacement	pump speed	pressure differential
		[cc]	[%]	[rpm]	[bar]
1	Type I	42	100,80,60 ,40,20	200,500,1000,2000 ,3000,4000,4600	20,50,100,200 ,300,400
2	Type I	130	100,50,20	1000,2000,2800	50,100,200,300,400
3	Type I	75	100,20	500,1000,1500 ,2000 2800	100,200,300,400
4	Type II	4	100,10	8750,10500	200

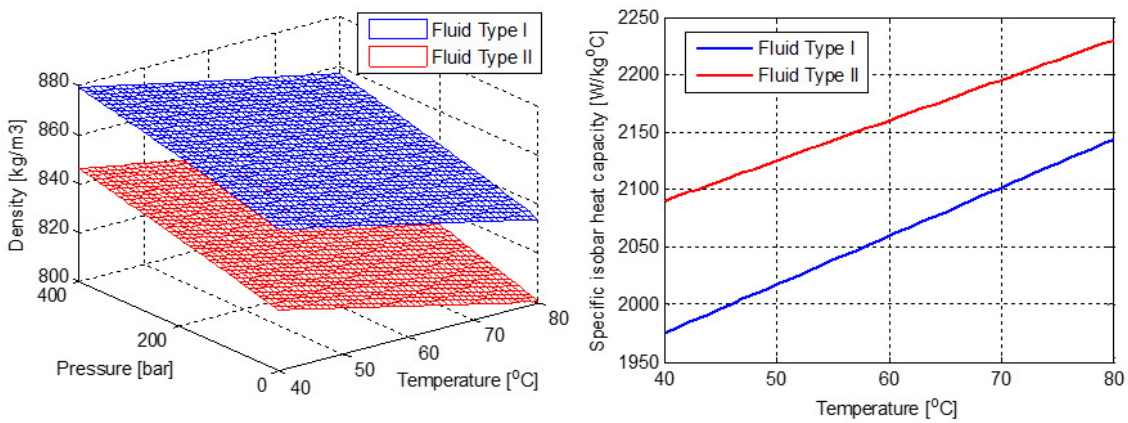

Fig. 4.9. Type I and type II fluid properties.

The first set of comparison results of the outlet temperature and the case temperature are shown in Fig. 4.10 to Fig. 4.14. In each figure, the outlet flow temperature comparison is shown on the left side and the case temperature comparison is shown on the right side. For both comparisons, the measurement results are shown in blue and the simulation results are shown in red. Both the pressure and speed are normalized to published maximum value of the measured unit.

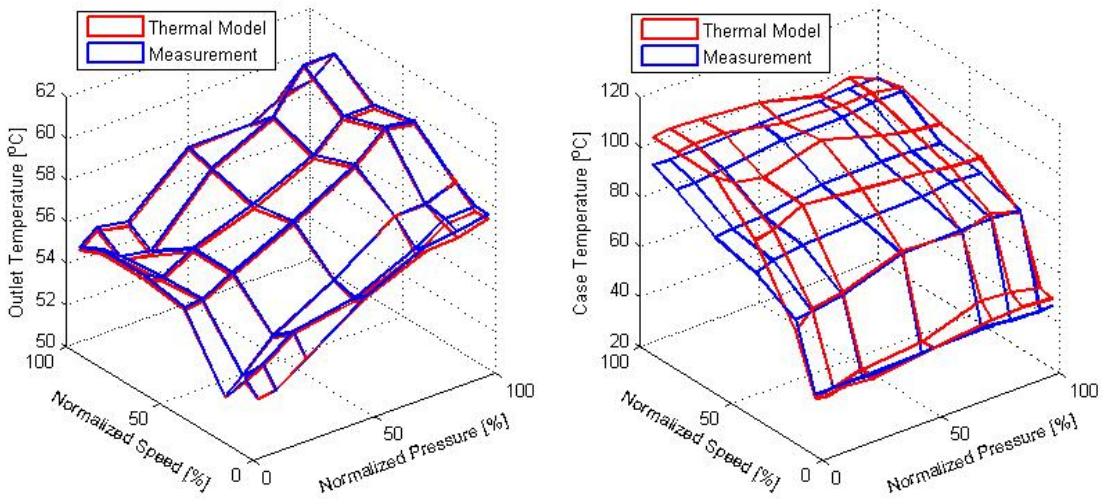

(a) Outlet temperature (b) Case temperature

Fig. 4.10. Set #1, flow temperatures comparison at 100% displacement.

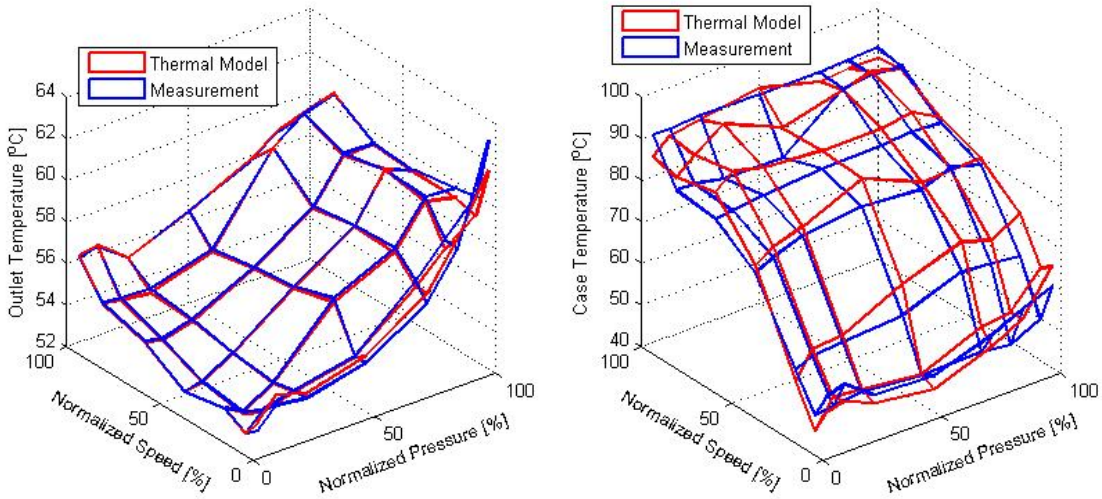

(a) Outlet temperature (b) Case temperature

Fig. 4.11. Set #1, flow temperatures comparison at 80% displacement.

The second set of outlet temperature and the case temperature comparison results are shown in Table 4.6 to Table 4.6. The first three columns are the swash plate angles, the pump speeds and the operating pressures in percentage to the maximum value.

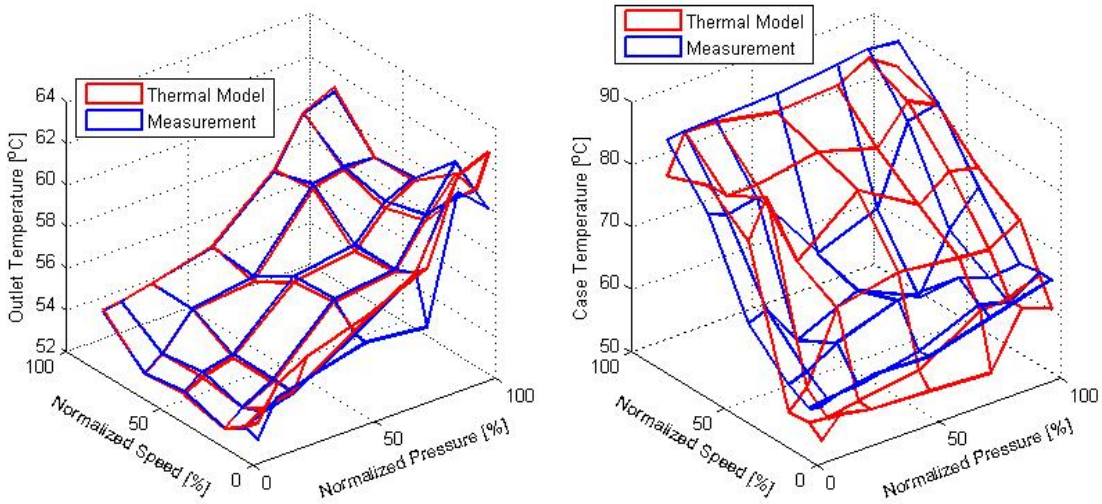

(a) Outlet temperature (b) Case temperature

Fig. 4.12. Set #1, flow temperatures comparison at 60% displacement.

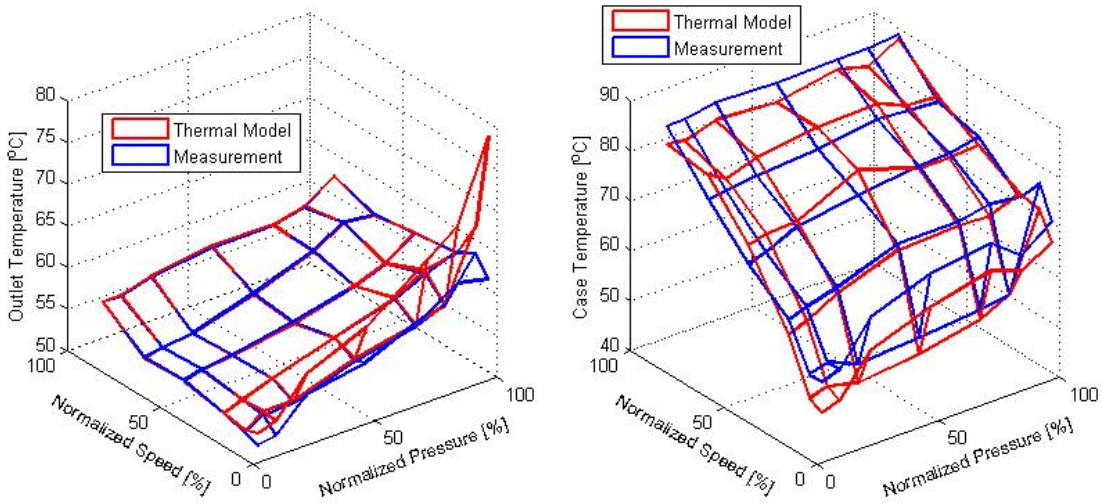

(a) Outlet temperature (b) Case temperature

Fig. 4.13. Set #1, flow temperatures comparison at 40% displacement.

The last six columns show the measured port and case temperatures, the simulated port and case temperatures and the difference between the measurement and the simulation.

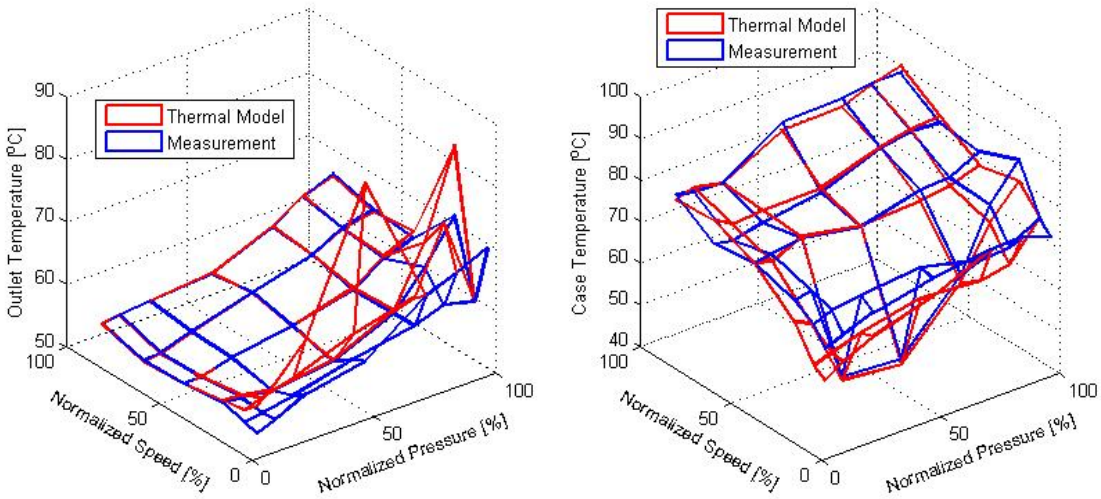

(a) Outlet temperature (b) Case temperature

Fig. 4.14. Set #1, flow temperatures comparison at 20% displacement.

Table 4.6 and Table 4.6 show the third set of outlet temperature and case temperature comparison. The first three columns are the swash plate angles, the pump speeds and the operating pressures in percentage to the maximum value. The last six columns show the measured port and case temperatures, the simulated port and case temperatures and the difference between the measurement and the simulation.

Table 4.6 shows the fourth set of comparison results, which is a 4cc pump with fluid type II. The first three columns are the swash plate angles, the pump speeds and the operating pressures in percentage to the maximum value. The last six columns show the measured port and case temperatures, the simulated port and case temperatures and the difference between the measurement and the simulation.

To summarize the comparison studies, the proposed pump flow temperatures prediction model is able to predict the outlet flow temperature and the case flow temperature with a reasonable accuracy of $\pm 5°C$ for outlet flow temperature and $\pm 10°C$ for case flow temperature.

Table 4.5.
Set #2, outlet and case flow temperature comparison at 100% displacement

O.C.			T_out			T_case		
beta	n	Δp	*mea.*	*sim.*	*diff.*	*mea.*	*sim.*	*diff.*
[%]	[%]	[%]	[°C]	[°C]	[°C]	[°C]	[°C]	[°C]
100	35.7	12.5	53.1	53.1	-0.1	63.2	60.7	2.5
100	35.7	25	54.1	54.1	0.0	66.7	68.0	-1.3
100	35.7	50	56.0	55.9	0.1	71.7	74.5	-2.8
100	35.7	75	58.2	58.0	0.2	76.0	82.2	-6.2
100	35.7	100	60.5	60.4	0.1	79.4	80.9	-1.5
100	71.5	12.5	53.7	53.7	0.0	76.6	76.2	0.4
100	71.5	25	54.6	54.6	0.0	78.4	79.5	-1.1
100	71.5	50	55.8	55.8	0.0	80.1	80.8	-0.8
100	71.5	75	57.8	57.7	0.0	83.1	86.8	-3.8
100	71.5	100	59.6	59.6	-0.1	84.3	83.8	0.5
100	100	12.5	57.2	57.2	0.0	83.1	83.9	-0.8
100	100	25	59.0	59.0	0.0	87.5	85.3	2.2
100	100	50	62.4	62.4	0.0	90.2	89.6	0.6
100	100	75	67.5	67.5	0.0	94.3	95.5	-1.2

4.7 Sensitivity study

Besides providing the necessary thermal boundaries for the lubricating fluid film behaviors study, the proposed model also allows to study the pump performance sensitivity on port and drain flow temperatures.

The perfect scaled lubricating interface will have the exact performance and efficiency as the baseline, therefore, the same port and case temperature as the baseline. However, this prefect scenario is very difficult to achieve. On the path toward the

Table 4.6.
Set #2, outlet and case flow temperature comparison at 50% displacement

O.C.			T_out			T_case		
beta	n	Δp	*mea.*	*sim.*	*diff.*	*mea.*	*sim.*	*diff.*
[%]	[%]	[%]	[°C]	[°C]	[°C]	[°C]	[°C]	[°C]
50	35.7	12.5	53.4	53.5	-0.1	60.9	58.4	2.4
50	35.7	25	54.6	54.6	0.0	62.5	62.3	0.2
50	35.7	50	57.2	56.9	0.2	66.8	71.6	-4.7
50	35.7	75	60.3	59.7	0.5	72.1	78.2	-6.1
50	35.7	100	63.9	63.9	0.0	79.6	79.7	-0.1
50	71.5	12.5	53.7	53.7	0.0	73.9	72.3	1.7
50	71.5	25	54.6	54.6	0.0	74.3	73.4	0.9
50	71.5	50	56.7	56.6	0.1	75.1	78.9	-3.7
50	71.5	75	58.9	58.7	0.2	77.5	82.7	-5.2
50	71.5	100	61.2	61.2	0.0	81.6	81.4	0.1
50	100	12.5	53.7	53.8	-0.1	81.8	75.4	6.4
50	100	25	54.6	54.7	-0.1	82.2	78.3	3.8
50	100	50	56.6	56.6	-0.1	82.3	81.3	1.1
50	100	75	58.6	58.6	0.1	83.2	84.4	-1.1
50	100	100	60.4	60.6	-0.1	84.9	82.6	2.3

prefect scaling approach, there are many scaled lubricating interfaces, which have the performance and efficiency close to the baseline, but not exactly the same. This sensitivity study will provide a general idea on how the performance difference influences the port and drain flow temperatures.

Table 4.7.
Set #2, outlet and case flow temperature comparison at 20% displacement

O.C.			T_out			T_case		
beta	n	Δp	*mea.*	*sim.*	*diff.*	*mea.*	*sim.*	*diff.*
[%]	[%]	[%]	[°C]	[°C]	[°C]	[°C]	[°C]	[°C]
20	35.7	12.5	54.1	54.2	-0.1	60.6	59.9	0.7
20	35.7	25	56.1	55.9	0.2	63.4	65.2	-1.8
20	35.7	50	61.4	60.5	0.9	69.5	72.7	-3.2
20	71.5	12.5	54.3	54.4	-0.1	73.1	71.9	1.1
20	71.5	25	55.5	55.5	0.0	73.3	72.8	0.4
20	71.5	50	58.6	58.2	0.4	74.4	77.8	-3.4
20	71.5	75	62.6	61.9	0.7	78.1	81.6	-3.5
20	71.5	100	67.6	69.0	-1.4	85.5	83.0	2.5
20	100	12.5	54.7	54.7	0.0	81.1	81.7	-0.6
20	100	25	55.7	55.7	-0.1	80.8	80.1	0.7
20	100	50	57.9	57.8	0.0	80.7	81.6	-0.9
20	100	75	61.3	60.9	0.4	82.3	84.9	-2.6
20	100	100	65.5	66.1	-0.6	86.9	85.0	1.9

In this sensitivity study, the internal leakage is ignored due to its limited impact on the pump flow temperatures. The outlet mass flow rate follows the simplified relationship:

$$\dot{m}_{out} = \dot{m}_{th} - \dot{m}_{leakage} \tag{4.26}$$

The theoretical flow rate is calculated from the pump size and the operating condition.

The total power loss is simplified into two parts, the volumetric power loss, and the mechanical power loss. The volumetric power loss is generated by the leakage

Table 4.8.
Set #3, outlet and case flow temperature comparison at 100% displacement

O.C.			T_out			T_case		
beta	n	Δp	*mea.*	*sim.*	*diff.*	*mea.*	*sim.*	*diff.*
[%]	[%]	[%]	[°C]	[°C]	[°C]	[°C]	[°C]	[°C]
100	17.9	25	54.2	54.0	0.2	48.0	57.9	-9.9
100	17.9	50	56.0	55.7	0.3	53.8	63.8	-10.0
100	17.9	75	58.4	58.0	0.4	61.0	68.9	-7.9
100	35.7	25	54.2	54.1	0.1	56.8	68.6	-11.9
100	35.7	50	55.8	55.6	0.1	60.5	69.5	-9.0
100	35.7	75	57.4	57.3	0.2	64.0	71.0	-6.9
100	35.7	100	59.4	59.4	0.0	70.2	69.9	0.3
100	53.6	25	54.3	54.2	0.1	58.7	71.6	-12.9
100	53.6	50	55.8	55.6	0.1	61.7	71.7	-10.0
100	53.6	75	57.4	57.3	0.1	65.8	71.1	-5.3
100	71.5	25	53.8	53.7	0.1	63.5	74.0	-10.5
100	71.5	50	55.4	55.3	0.1	66.7	74.2	-7.5
100	71.5	75	57.1	57.0	0.1	69.2	72.3	-3.0
100	71.5	100	58.6	58.7	-0.1	73.0	69.5	3.5
100	100	75	57.3	57.3	0.0	75.0	73.5	1.5
100	100	100	58.7	58.9	-0.2	76.4	71.1	5.2

flow rate and the pressure drop from the displacement chamber pressure to the case pressure, and the mechanical loss captures all the rest of the energy dissipation.

$$\begin{aligned} P_{loss} &= P_{vol.loss} + P_{mech.loss} \\ P_{loss} &= Q_{leakage} \cdot \Delta p + P_{mech.loss} \end{aligned} \tag{4.27}$$

Table 4.9.
Set #3, outlet and case flow temperature comparison at 20% displacement

O.C.			T_out			T_case		
beta	n	Δp	*mea.*	*sim.*	*diff.*	*mea.*	*sim.*	*diff.*
[%]	[%]	[%]	[°C]	[°C]	[°C]	[°C]	[°C]	[°C]
20	35.7	25	55.1	55.5	-0.4	60.1	58.6	1.5
20	35.7	75	64.1	66.2	-2.1	70.9	68.9	1.9
20	71.5	25	54.8	54.8	0.0	60.0	59.6	0.4
20	71.5	75	59.9	60.1	-0.2	68.2	67.5	0.7
20	71.5	100	66.1	69.8	-3.7	76.2	73.1	3.2
20	100	75	61.5	61.3	0.2	71.4	72.0	-0.6
20	100	100	65.8	67.1	-1.3	76.8	75.0	1.8

50 sets of outlet flow temperatures and case flow temperatures are obtained at different leakage flow rates and mechanical losses using the pump flow temperatures prediction model. Fig. 4.15 and Fig. 4.16 show two three-dimensional meshes for the simulated outlet flow temperatures and case flow temperatures.

In Fig. 4.15, the three-dimensional grid shows the outlet flow temperatures over different leakages and mechanical losses. The leakages displayed in the picture are normalized to the theoretical delivered flow rate, and the mechanical losses displayed in the picture are normalized to the theoretical delivered power. The green dot in the three-dimensional picture shows the ideal design which has the minimum leakage and the minimum mechanical loss. The design marked with the red dot has a high mechanical loss, and the design marked with the yellow dot a high leakage. Two pictures on the right show two side views of the three-dimensional picture. From these pictures, two trends can be observed clearly: the outlet flow temperature increases with both the leakage and the mechanical loss.

Table 4.10.
Set #4, outlet and case flow temperature comparison at 100% and 10% displacement

O.C.			T_out			T_case		
beta	n	Δp	*mea.*	*sim.*	*diff.*	*mea.*	*sim.*	*diff.*
[%]	[%]	[%]	[°C]	[°C]	[°C]	[°C]	[°C]	[°C]
100	83.3	100	86.2	86.2	0.0	96.1	96.8	-0.8
10	83.3	100	88.0	88.1	-0.1	97.0	96.7	0.3
100	83.3	100	119.6	119.5	0.0	125.2	125.8	-0.6
10	83.3	100	120.6	121.1	-0.5	125.3	124.5	0.8
100	100	100	86.6	86.7	0.0	99.7	98.8	0.9
10	100	100	90.0	90.3	-0.3	101.8	101.1	0.8
100	100	100	119.8	119.7	0.1	127.2	128.7	-1.5
10	100	100	120.7	120.8	-0.1	127.6	127.5	0.1

Fig. 4.16 shows the case flow temperatures over various leakages and mechanical losses. Two trends can be observed for the case flow temperature: the case flow temperature decreases with the leakage and increases with the mechanical loss. The higher mechanical power loss transferred into the displacement chamber volume and the case volume increases both the outlet flow temperature and the case temperature. The case flow temperature decreases with the leakage because the case flow temperature variation is inversely proportional to the case flow rate which is the leakage flow rate. The outlet flow temperature increases with the leakage because higher leakage produces higher volumetric power loss.

Fig. 4.16 also shows that the case flow temperature mesh is flat in the high leakage region and steeper in the low leakage region. This is because the sensitivity of the case flow temperature decreases with increasing case flow rate, i.e. increasing leakage.

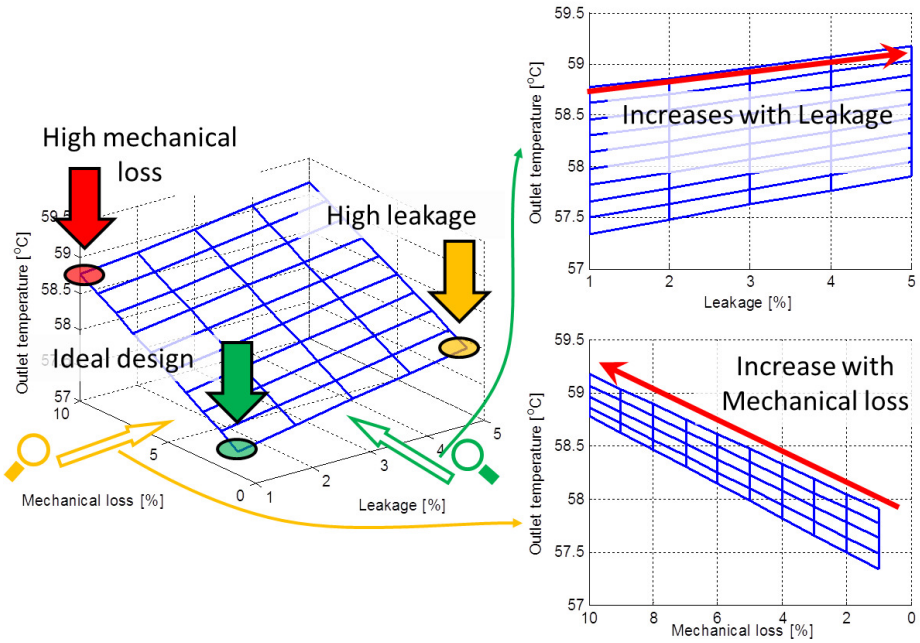

Fig. 4.15. Outlet flow temperature for different normalized leakage the normalized mechanical losses.

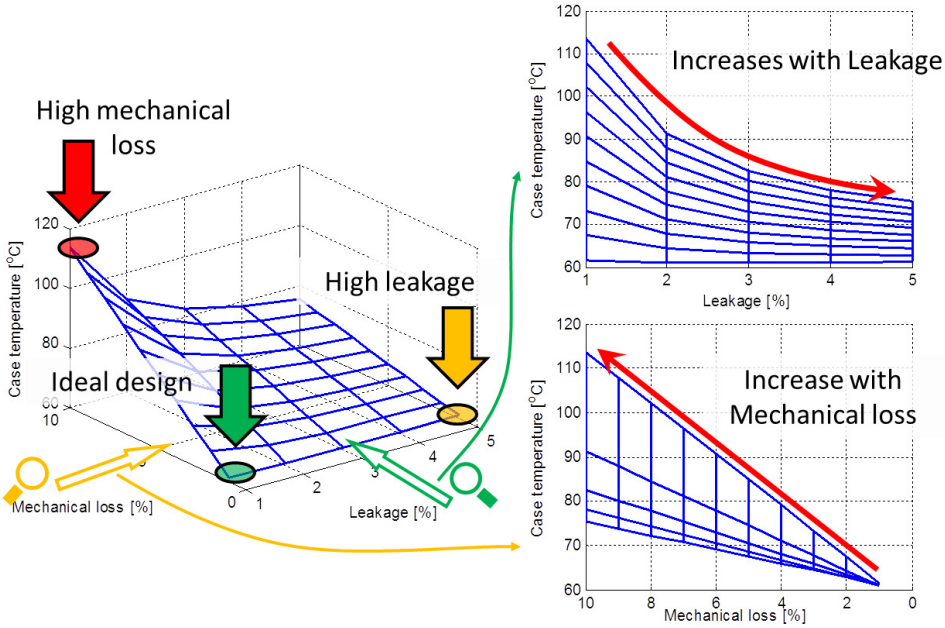

Fig. 4.16. Case flow temperature for different normalized leakage the normalized mechanical losses.

To conclude this sensitivity study, the machine performance will have a small impact on the port and case flow temperature when the normalized leakage is high. However, when normalized leakage is low, the case temperature increases dramatically with the mechanical loss. The high leakage flow temperature will then cause low fluid viscosity, therefore unfavorable load support in the lubricating gap, and more thermal deformation, which can be dangerous in some designs.

4.8 Conclusion

In this chapter, a novel outlet and case flow temperatures prediction model for axial piston machine is proposed. The model calculates the port temperatures considering the compression-expansion effect and the heat generation and heat transfer in and between the solid and the fluid domain. The model is designed to apply on pumps and motors at any size by scaling the coefficients with the respective linear scaling factor. Over three hundred measured outlet and case flow temperatures have been used to compare to the simulated results. The operating conditions include four different unit size from 4 cc to 130 cc, two different types of fluid, from 10% to 100% displacement, from 200 rpm to 10500 rpm, from 20 bar to 400 bar. The comparison results prove that the proposed model is capable to predict the outlet and case flow temperatures for unit with any size at any operating condition.

This proposed port temperatures prediction model allows the previously mentioned fluid structure and thermal interaction model to be used for virtual prototyping and virtual optimization without any measurement data.

A sensitivity study is conducted using the proposed temperature prediction model. The sensitivity study results can be used to reduce the required computational time for the iterative pump and motor performance calculation. More sensitivity studies were conducted within this research, and are detailed in [44].

5. THE SCALING OF PHYSICAL PHENOMENA IN AXIAL PISTON MACHINES

The energy efficiency of axial piston machines do not remind the same after scaling due to the size-dependent physics of the three tribological lubricating interfaces. In this chapter, the size-dependence of physics that determines the behavior of the three lubricating interfaces, including the hydrostatic/hydrodynamic pressure distribution in fluid domain, the elastic deformation due to pressure and thermal load in solid domain, and the heat transfer in the fluid and solid domains, are investigated using scalable dimensions. The findings are used to provide a guide to scale the lubricating interface while compensating the non-scalable physical phenomena.

The scalable or non-scalable physical phenomenon is defined as either it follows the linear scaling law, such as pressure, temperature, and translational velocity remind the same, distance and displacement follows the first order of the linear scaling factor, area, power, and flow rate follow the second order of the linear scaling factor, and mass and volume follow the third order of the linear scaling factor.

5.1 Linear scaling method (conventional approach)

Before explaining size-dependent physics, an example is given to demonstrate the performance difference of the three interfaces before and after scaling according to the linear scaling law. The scaling law is defined as scaling the axial piston machine proportionally, such that the ratio of one design parameter to another is maintained. The operating speed is scaled to keep the relative sliding speed between the parts that form the tribological interfaces constant. For this example, a Sauer-Danfoss S90 75cc unit is selected as the baseline unit. This baseline is linearly scaled to two different sizes. The smaller one is scaled based on the linear factorλ of 0.5, and the bigger one

is scaled based on the linear factorλ of 2. All three units have been simulated using the fluid-structure-thermal interaction model described in the previous section. As Table 5.1 shows, the biggest unit has a displacement volume 64 times larger than the smallest unit.

In order to keep the sliding velocity the same, the rotational speed is scaled with the reciprocal of the linear factorλ. The sizes of the three units and their respective operating conditions are summarized in Table 5.1, with the labels A, B, and C. These three sets of size/operating condition combinations are used repeatedly through this chapter.

Table 5.1.
Summary of unit sizes and operating conditions.

	A	B	C
linear factor λ	0.5	1	2
Unit size [cc]	9.375	75	600
Pressure [bar]	400	400	400
Displacement [%]	100	100	100
Speed [rpm]	7200	3600	1800

Since A, B, and C share the same pressure, the same swash plate angle, and the same sliding velocity, the normalized energy dissipation, the normalized leakage flow rate, and the normalized torque loss of these three cases are comparable for each of the lubricating interfaces. The normalized energy dissipation uses the theoretical output power as reference, the normalized leakage flow rate uses the theoretical outlet flow rate as reference, and the normalized torque loss uses the theoretical input torque as reference. The power loss, the volumetric loss, and the torque loss represent the fluid behavior and the performance of each interface.

Fig. 5.1 to Fig. 5.2 show the simulated performance of the three lubricating interfaces using the previously described fluid-structure-thermal interaction model, which

takes into consideration the non-isothermal fluid, as well as both pressure and thermal solid body deformation.

Fig. 5.1 shows the performance comparison of the piston/cylinder interface for A, B, and C. The normalized energy dissipation, normalized leakage flow, and normalized torque loss correspond to a single piston/cylinder interface. According to the simulation results, the normalized energy dissipation and the normalized torque loss for different unit sizes are relatively close (they differ less than 20%). However, the normalized leakage exhibits significant size-dependence. To be exact, the piston/cylinder interface C produces more than twice the simulated normalized leakage compared to its smallest counterpart, A.

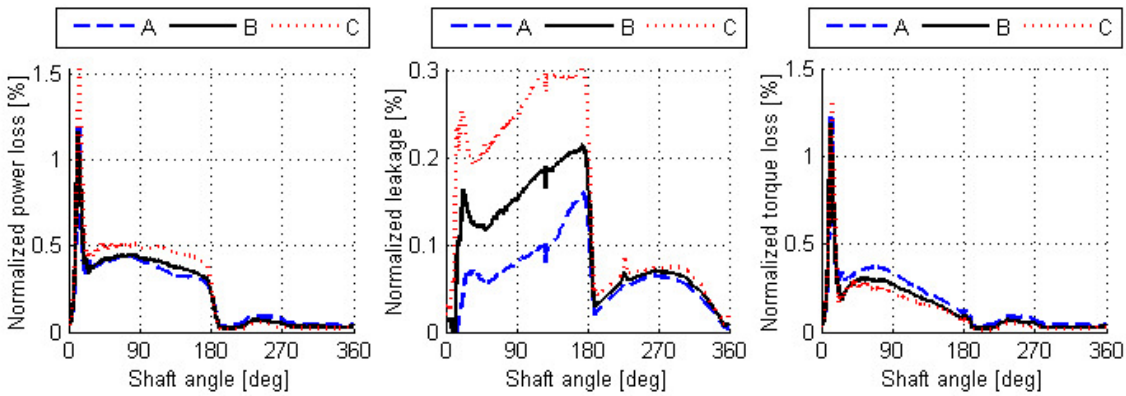

Fig. 5.1. Normalized piston/cylinder interface performance for different sizes.

Fig. 5.2 shows the performance comparison of the cylinder block/valve plate interface of the three cases, A, B, and C. According to the results, the cylinder block/valve plate interface behaves very differently for different sizes. The larger unit produces more normalized leakage than the smaller ones, while the smaller unit produces more normalized torque loss than the larger ones. This results in a similar normalized energy dissipation between the mid-size B and large-size C, but a greater normalized power loss in the small unit A.

Fig. 5.3 shows the normalized energy dissipation, normalized leakage, and the normalized torque loss for a single slipper/swashplate interface corresponding to each

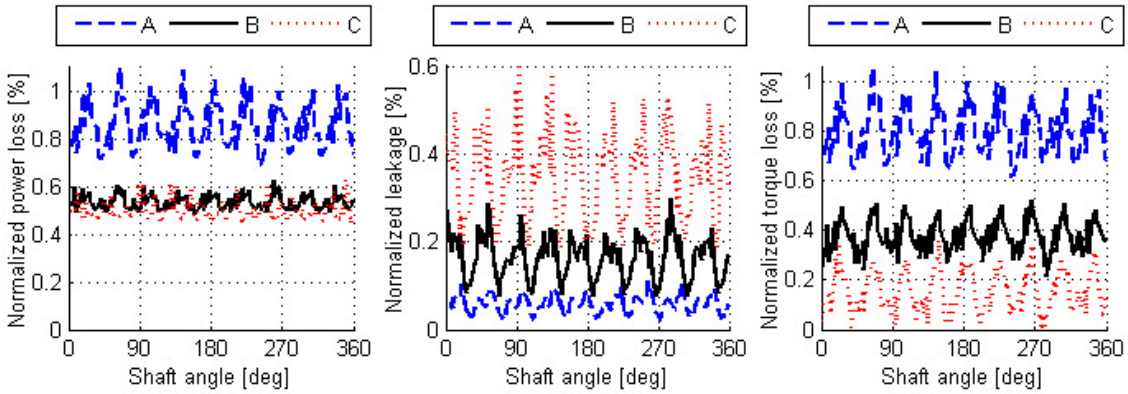

Fig. 5.2. Normalized cylinder block/valve plate interface performance for different sizes.

of the simulated unit sizes. According to the results, similarly to the piston/cylinder interface and the cylinder block/valve plate interface, the large unit C produces more leakage than the smaller units. Furthermore, the smaller unit A produces more torque loss than the larger units. At the selected operating conditions simulated for the three units, the energy dissipation in the slipper/swashplate interface is dominated by viscous shear. Therefore, the energy dissipation shows similar trends to the torque loss.

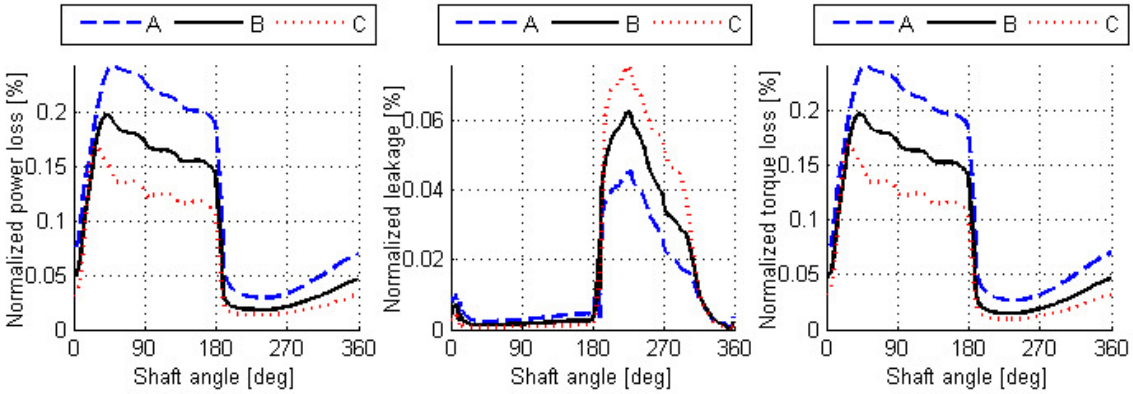

Fig. 5.3. Normalized slipper/swashplate interface performance for different sizes.

Comparing the results of the three differently sized units in Figure 5 to Figure 7 demonstrates that the linearly scaled piston/cylinder interface, cylinder block/valve plate interface, and slipper/swashplate interface do not perform the same as their pre-scaled counterparts without design modifications. The undesired size-dependence of the lubricating interface performance leads to the demand for an understanding of the physics behind the scaling process. In the following sections, the physical phenomena that contribute to the tribological performance of the three lubricating interfaces are studied independently.

5.2 Analysis of fundamental physics of lubricating interfaces

The physical phenomena that are studied in this section include the viscous fluid pressure distribution (Reynolds equation), the elastic solid body deformation under both pressure and thermal loads, the heat dissipation and heat transfer in the fluid domain, and the heat transfer in the solid bodies. For each physical phenomenon, the governing equations are derived using scalable dimensions in order to examine their size-dependence.

5.2.1 Fluid pressure distribution

The Reynolds equation [13], which is derived from the Navier-Stokes equation and the conservation of mass, is the fundamental governing equation of a compressible, Newtonian, laminar flow pressure distribution. A general form of the Reynolds equation of an arbitrary lubricating gap, e.g. the one shown in Fig. 5.4, can be written as:

$$\begin{aligned} 0 = \nabla \cdot \left(-\frac{\rho h_g^3}{12\mu} \nabla p \right) + \frac{(v_t + v_b)}{2} \cdot \nabla \left(\rho h_g \right) \\ -\rho v_t \cdot \nabla h_{gt} + \rho v_b \cdot \nabla h_{gb} + \rho \left(w_t - w_b \right) \end{aligned} \tag{5.1}$$

The abbreviation t stands for top surface, and b stands for bottom surface. Each

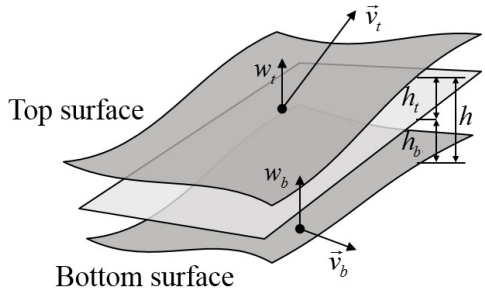

Fig. 5.4. An arbitrary lubricating gap.

dimensional variable can be described using an original dimension and a linear scaling factor, as demonstrated in Eq. 9. The linear factor is consistent for each variable.

$$\begin{gathered} x = \lambda x_0 \quad y = \lambda y_0 \quad z = \lambda z_0 \quad \vec{v} = v_0 \quad \vec{u} = \vec{u}_0 \\ \nabla \cdot \tilde{\mathbf{A}} = \frac{1}{\lambda} \cdot \left(\nabla \cdot \tilde{\mathbf{A}} \right)_0 \quad \nabla a = \frac{1}{\lambda} \cdot (\nabla a)_0 \end{gathered} \tag{5.2}$$

By applying Eq. 5.2 to Eq. 5.1, the Reynolds equation becomes:

$$\begin{gathered} 0 = \nabla \cdot \left(-\frac{\rho \lambda h_0^3}{12\mu} \nabla p\left(\lambda\right) \right) + \frac{\left(v_{t0} + v_{b0}\right)}{2} \cdot \nabla \left(\rho h_0\right) \\ -\rho \vec{v}_t \cdot \nabla h_{t0} + \rho \vec{v}_b \cdot \nabla h_{b0} + \rho \left(w_t - w_b\right) \end{gathered} \tag{5.3}$$

Comparing Eq. 5.1 to Eq. 5.3, the remaining scaling factor makes the Reynolds equation size-dependent. Therefore, the pressure distribution in a linearly scaled lubricating gap is not able to retain the behavior of the gap in the pre-scaled unit.

5.2.2 Solid body elastic deformation

The solid body elastic deformation due to the pressure and thermal loads also plays an essential role in the performance of the lubricating interface. The nodal displacement under the pressure and thermal load is determined using the principle of minimal potential energy. The total potential energy Π is the sum of the strain energy U and the applied load potential energy V_{NF}:

$$\Pi = U + V_{NF} \tag{5.4}$$

where the applied load potential energy V is a function of the nodal force $\mathbf{f}_E$ and the nodal displacement vector $\mathbf{u}$:

$$V_{NF} = -\mathbf{u}^T \mathbf{f}_E \tag{5.5}$$

and the strain energy U is a function of the elastic strain ε_F, and the stress σ:

$$U = \frac{1}{2} \int_{\delta V} {\varepsilon_F}^T \sigma dV \tag{5.6}$$

The relationship between the stress and the elastic strain can be expressed by the constitutive matrix $\mathbf{C}$:

$$\sigma = \mathbf{C}\varepsilon_F = \mathbf{C}\left(\varepsilon - \varepsilon_T\right) \tag{5.7}$$

where the constitutive matrix $\mathbf{C}$ contains the isothermal elastic modulus E and the Poissons ratio ν:

$$\mathbf{C} = \frac{E}{(1-\nu)(1-2\nu)} \begin{bmatrix} 1-\nu & \nu & \nu & 0 & 0 & 0 \\ \nu & 1-\nu & \nu & 0 & 0 & 0 \\ \nu & \nu & 1-\nu & 0 & 0 & 0 \\ 0 & 0 & 0 & \frac{1-2\nu}{2} & 0 & 0 \\ 0 & 0 & 0 & 0 & \frac{1-2\nu}{2} & 0 \\ 0 & 0 & 0 & 0 & 0 & \frac{1-2\nu}{2} \end{bmatrix} \tag{5.8}$$

The matrix $\mathbf{B}$ expresses the strain as a function of the nodal displacement:

$$\varepsilon = \mathbf{B}\mathbf{u} \tag{5.9}$$

Combining Eq. 5.6, Eq. 5.7, and Eq. 5.9:

$$U = \frac{1}{2} \int_{\delta V} \left(\mathbf{B}\mathbf{u} - \varepsilon_T\right)^T \mathbf{C} \left(\mathbf{B}\mathbf{u} - \varepsilon_T\right) dV \tag{5.10}$$

The total potential energy then becomes:

$$\Pi = \frac{1}{2} \int_{\delta V} \left(\mathbf{B}\mathbf{u} - \varepsilon_T\right)^T \mathbf{C} \left(\mathbf{B}\mathbf{u} - \varepsilon_T\right) dV - \mathbf{u}^T \mathbf{f}_E \tag{5.11}$$

According to the minimal potential energy principle, by setting the differential of the total potential energy with respect to the nodal displacement to zero, the elasticity equation is obtained:

$$\int_{\delta V} \mathbf{B}^T \mathbf{C} \mathbf{B} dV \mathbf{u} = \int_{\delta V} \mathbf{B}^T \mathbf{C} \varepsilon_T dV + \mathbf{f}_E \tag{5.12}$$

Eq. 5.12 can be written more compactly as:

$$\mathbf{k}\mathbf{u} = \mathbf{f}_T + \mathbf{f}_E \tag{5.13}$$

In order to examine the size-dependence of the solid body deformation under both pressure and thermal loading, the loading pressure distribution and temperature distribution is proportionally scaled in order to allow for a direct comparison of the effects of scaling across different unit sizes. Therefore, the nodal force vector due to the external load scales with area, which scales according to the second order of the linear scaling factor:

$$\mathbf{f}_E(\lambda) = \lambda^2 \mathbf{f}_{E0} \tag{5.14}$$

When using scalable dimensions, Eq. 5.9 therefore becomes:

$$\varepsilon(\lambda) = \mathbf{B}(\lambda)\, \mathbf{u}(\lambda) \tag{5.15}$$

Again, scaling the pressure distribution assures that the stress remains the same, while the nodal displacement scales according the linear scaling factor. Accordingly, Eq 5.15 becomes:

$$\varepsilon_0 = \lambda \mathbf{B}(\lambda)\, \mathbf{u}_0 \tag{5.16}$$

It can be seen from Eq. 5.16 that the matrix$\mathbf{B}$scales according to the reciprocal of the linear scaling factor:

$$\mathbf{B}(\lambda) = \lambda^{-1} \mathbf{B}_0 \tag{5.17}$$

The nodal forces vector due to thermally induced stress then scales as:

$$\begin{aligned} \mathbf{f}_T(\lambda) = \int_{\delta V} \mathbf{B}(\lambda)^T \mathbf{C} \varepsilon_T dV(\lambda) &= \lambda^2 \int_{\delta V} \mathbf{B}_0{}^T \mathbf{C} \varepsilon_T dV_0 \\ &= \lambda^2 \mathbf{f}_{T0} \end{aligned} \tag{5.18}$$

The element stiffness matrix $\mathbf{k}$ scales as:

$$\begin{aligned}\mathbf{k}\left(\lambda\right) = \int\limits_{\delta V} \mathbf{B}(\lambda)^T \mathbf{C}\mathbf{B}\left(\lambda\right) dV\left(\lambda\right) &= \lambda \int\limits_{\delta V} \mathbf{B}_0{}^T \mathbf{C}\mathbf{B}_0 dV_0 \\ &= \lambda \mathbf{k}_0\end{aligned} \tag{5.19}$$

With scaling, the elasticity equation becomes:

$$\lambda \mathbf{k}_0 \mathbf{u} = \lambda^2 \mathbf{f}_{T0} + \lambda^2 \mathbf{f}_{E0} \tag{5.20}$$

Therefore, the resulting nodal displacement due to pressure and thermal loading is scaled based on the first order of the scaling factor:

$$\mathbf{u}\left(\lambda\right) = \lambda \mathbf{u}_0 \tag{5.21}$$

In conclusion, the elastic deformation due to both the pressure and thermal loading is linearly scalable. The solid parts of the lubricating interfaces deform linearly with respect to the first order linear scaling factor when the pressure and temperature distribution is kept consistent. Therefore, the elastic deformation principle itself does not cause any performance difference when scaling an axial piston machine.

To verify this conclusion, simulation cases A B, and C are reconfigured in order to ensure that they remain comparable in terms of both the pressure and thermal loading. The temperature distribution is made identical for all three cases by turning off the solid body heat transfer model. Instead of solving the heat transfer problem, the solid body temperatures remain at their initial values. The heat transfer phenomenon is further discussed in future sections. However, from the conclusion of the Reynolds equation size dependence study associated with Eq. 5.3, the pressure distribution is not able to maintain the same across cases A, B, and C when changing the size of the interface. In order to achieve a consistent pressure distribution that will allow for drawing the proper conclusions from this study, and also in order to verify the Reynolds equation size-dependence study, instead of using the same fluid viscosity in the three simulation cases, the fluid viscosity was set artificially with respect to the first order of the linear scaling factor:

$$\mu = \lambda \cdot \mu_0 \tag{5.22}$$

With the viscosity as described by Eq. 5.22, Eq. 5.3 becomes:

$$0 = \nabla \cdot \left(-\frac{\rho h_{g0}^3}{12\mu_0} \nabla p\left(\lambda\right) \right) + \frac{\left(v_{t0} + v_{b0}\right)}{2} \cdot \nabla\left(\rho h_0\right) \\ -\rho \vec{v}_t \cdot \nabla h_{t0} + \rho \vec{v}_b \cdot \nabla h_{b0} + \rho\left(w_t - w_b\right) \tag{5.23}$$

In this way, the pressure distribution is maintained consistent.

The inputs for simulation cases A, B, and C are then characterized as shown in Table 5.2.2. Fig. 5.5 shows a comparison of the normalized energy dissipation, the normalized leakage flow, and the normalized torque loss of a single piston/cylinder interface for the three simulation cases, A, B, and C. The fluid viscosity is artificially scaled with the linear scaling factor, and the fluid and the solid body heat transfer models are turned off to maintain the temperature distribution consistent between cases. The figure shows that the normalized energy dissipation, the normalized leakage, and the normalized torque loss are very similar throughout the three simulation cases. The performance differences are less than 4%.

Table 5.2.
Summary of operating conditions with scaled fluid viscosity.

	A	B	C
linear factor λ	0.5	1	2
Unit size [cc]	9.375	75	600
Pressure [bar]	400	400	400
Displacement [%]	100	100	100
Speed [rpm]	7200	3600	1800
Fluid viscosity	$0.5 \cdot \mu_0$	μ_0	$2 \cdot \mu_0$

Fig. 5.6 shows a comparison of the normalized energy dissipation, the normalized leakage, and the normalized torque loss of the cylinder block/valve plate interface simulation for cases A, B, and C. Again, the fluid viscosity is artificially scaled with the linear scaling factor, and the fluid and the solid body heat transfer models are turned

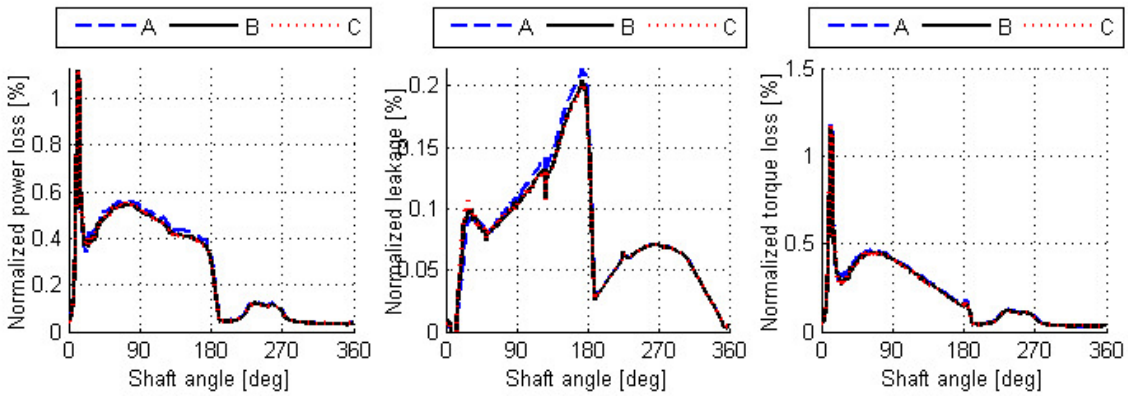

Fig. 5.5. Normalized piston/cylinder interface performance for different sizes (no heat transfer, scaled viscosity).

off to maintain the temperature distribution consistent. Similar to the piston/cylinder interface comparison results, the cylinder block/valve plate interface results show that the interface performs very similarly for the three simulated unit sizes.

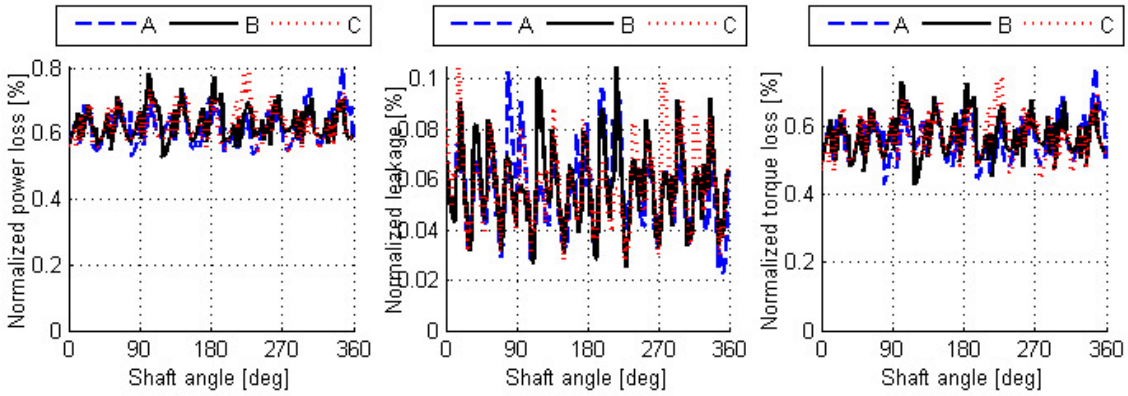

Fig. 5.6. Normalized cylinder block/valve plate interface performance for different sizes (no heat transfer, scaled viscosity).

Fig. 5.7 shows a comparison of the normalized energy dissipation, the normalized leakage, and the normalized torque loss of the slipper swashplate interface simulation for cases A, B, and C. As was done for the piston/cylinder interface and the cylinder block/valve plate interface, the fluid viscosity is artificially scaled with the linear

scaling factor, and the fluid and solid body heat transfer models are turned off to maintain the temperature distribution consistent. The normalized energy dissipation and normalized torque loss are almost identical for the different sizes simulated. The normalized leakages from the three cases are also very close to each other.

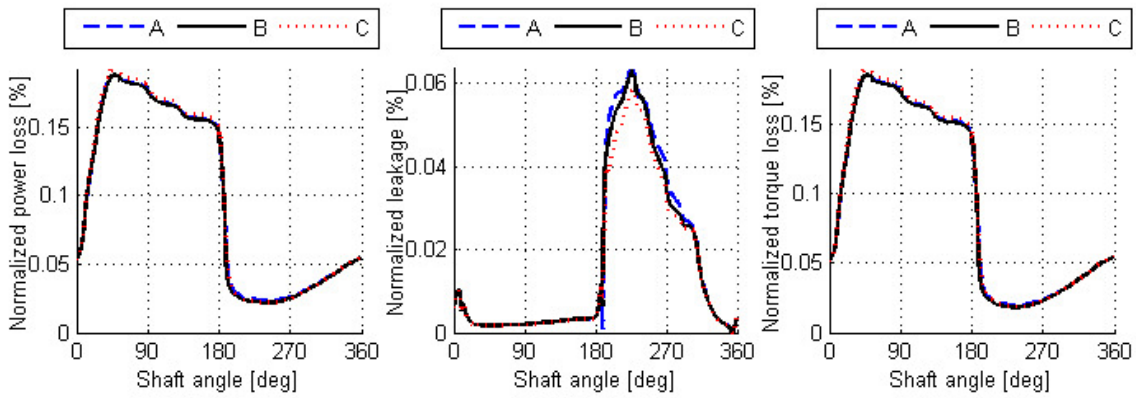

Fig. 5.7. Normalized slipper/swashplate interface performance for different sizes (no heat transfer, scaled viscosity).

The simulation results from Fig. 5.5 to Fig. 5.7 validate all the conclusions in the Reynolds equation size-dependence study and the elastic deformation size-dependence study. In summary, without the consideration of heat transfer, the scaled axial piston machine is able to achieve the same performance as the pre-scaled unit with a different fluid viscosity.

5.2.3 Multi-domain heat transfer

To investigate the size-dependence of the multi-domain heat transfer, the simulation cases A, B, and C as shown in Table 5.2.2 are rerun with both the fluid domain heat transfer model and the solid domain heat transfer model turned on.

Fig. 5.8 shows a comparison of the normalized energy dissipation, the normalized leakage, and the normalized torque loss of a single piston/cylinder interface for the three simulation cases A, B, and C, again with the fluid viscosity artificially scaled with the linear scaling factor. Also considered in these simulations are the elastic

solid body deformations due to pressure and thermal loads. The fluid temperature distribution is calculated from a three-dimensional fluid heat transfer model, and the solid body temperature distribution is calculated from a three-dimensional solid body heat transfer model. In comparison to Fig. 5.5, the piston/cylinder interface shows much more variation across the different sizes in Fig. 5.8.

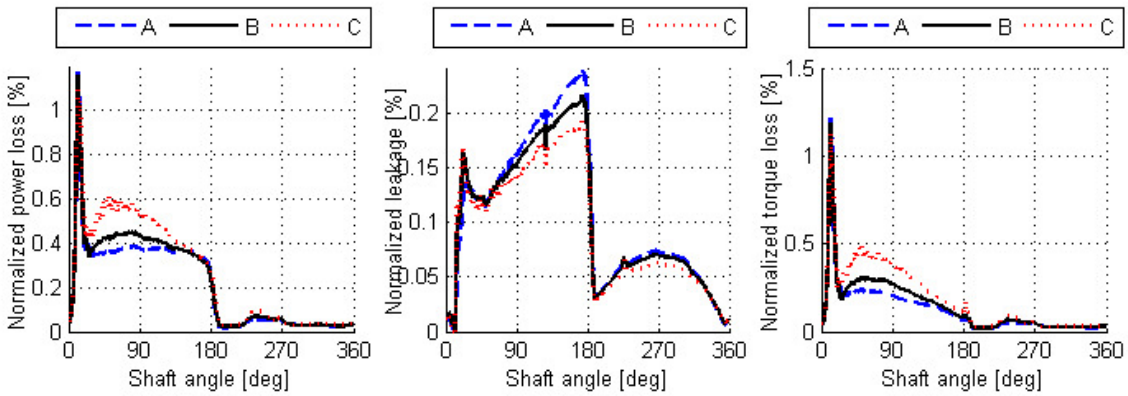

Fig. 5.8. Normalized piston/cylinder interface performance for different sizes (scaled viscosity).

Fig. 5.9 compares the normalized energy dissipation, the normalized leakage, and the normalized torque loss of the cylinder block/valve plate interface for cases A, B, and C, again with the fluid viscosity artificially scaled, and with both the fluid and the solid heat transfer models turned on. The fluid temperature distribution is calculated from a three-dimensional fluid heat transfer model, and the solid temperature distribution is calculated from a three-dimensional solid body heat transfer model. The figure shows that the normalized energy dissipation remains at roughly the same level for all three cases, but the normalized leakage and the normalized torque loss have major differences across the different unit sizes.

Fig. 5.10 compares the normalized energy dissipation, the normalized leakage, and the normalized torque loss of the slipper/swashplate interface for the three simulated cases, A, B, and C, with the fluid viscosity artificially scaled, and with both the fluid and the solid heat transfer models turned on. Just as for the piston/cylinder interface

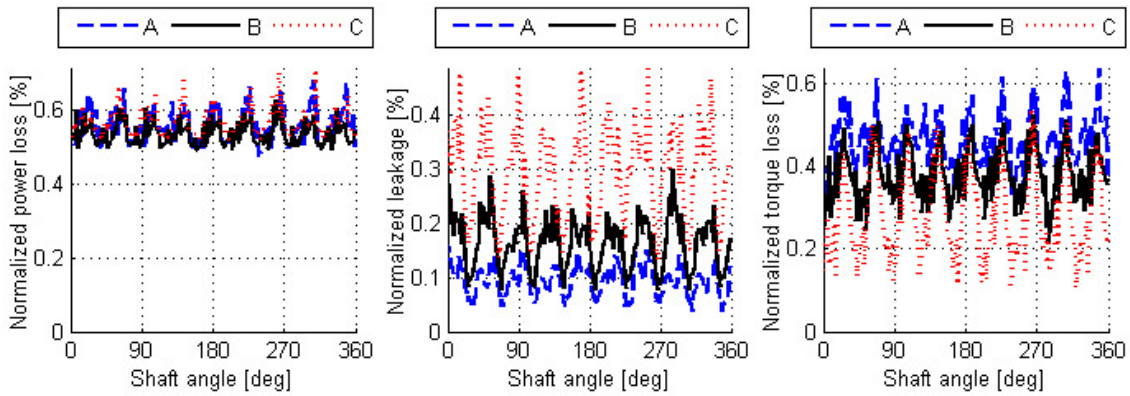

Fig. 5.9. Normalized cylinder block/valve plate interface performance for different sizes (scaled viscosity).

and the cylinder block/valve plate interface, the fluid temperature distribution is calculated from a three-dimensional fluid heat transfer model, and the solid temperature distribution is calculated from a three-dimensional solid body heat transfer model. The different size slipper/swashplate interfaces behave very similarly even with the heat transfer model turned on.

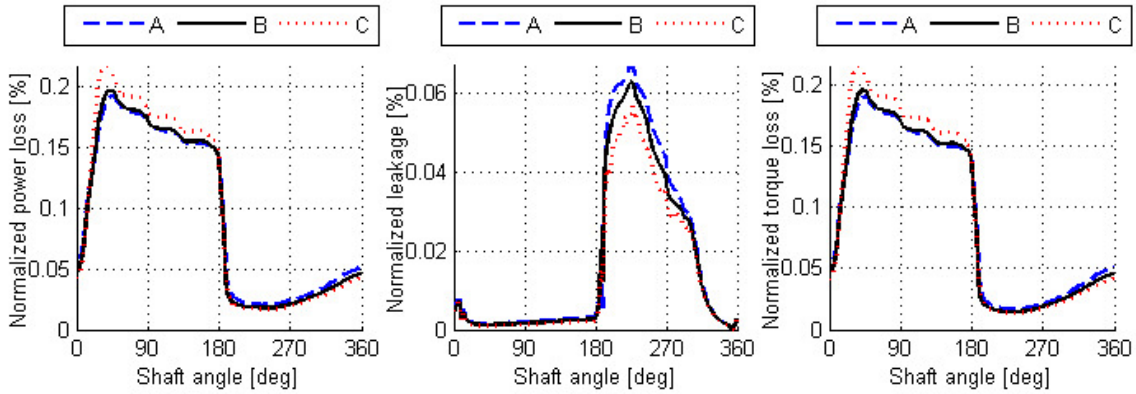

Fig. 5.10. Normalized slipper/swashplate interface performance for different sizes (scaled viscosity).

To further investigate the size-dependence of the thermal behavior of the three lubricating interfaces, the resulting solid body temperature distributions of the piston,

cylinder block, and the slipper are studied as shown from Fig. 5.12 to Fig. 5.14. In order to compare the solid body temperature distributions between different sizes, the solid parts are stretched to the same size, as illustrated in Fig. 5.11.

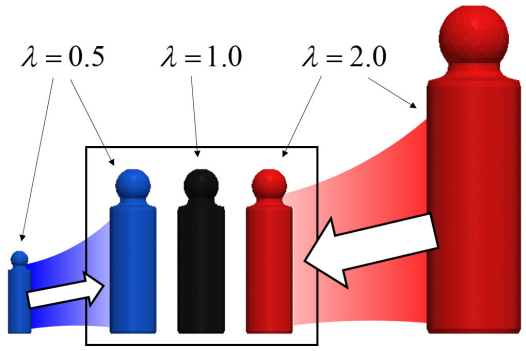

Fig. 5.11. Demonstration of solid body temperature comparison for different sizes.

Fig. 5.12 shows the piston temperature distributions of cases A, B, and C. Clearly, the piston solid body temperature distributes differently over the three sizes. The temperature distribution of the larger unit shows more variation than its smaller counterpart.

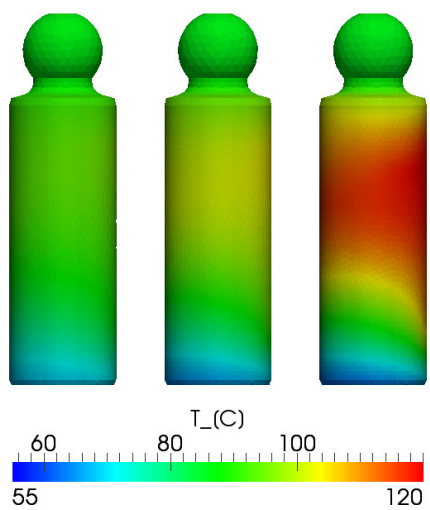

Fig. 5.12. Piston temperature distribution comparison for different sizes (scaled viscosity).

Fig. 5.13 shows the cylinder block temperature distribution of cases A, B, and C. The cylinder block solid body temperature distribution also shows more variation for the larger size.

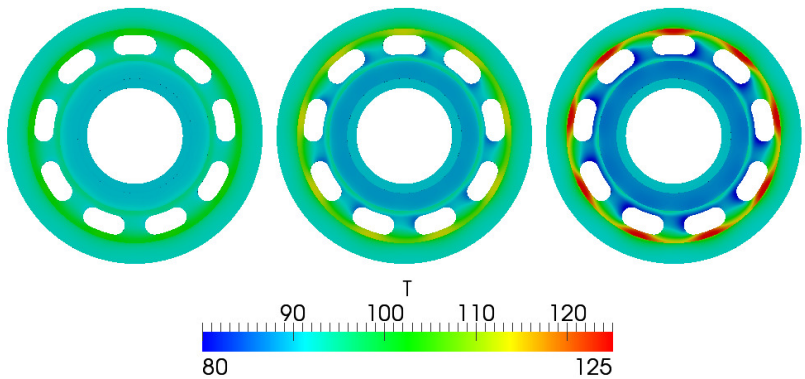

Fig. 5.13. Cylinder block temperature distribution comparison for different sizes (scaled viscosity).

Fig. 5.14 shows the slipper temperature distribution of cases A, B, and C. Similar to the piston and the cylinder block solid body temperatures, the slipper solid body temperature also shows more variation for the larger size. However, unlike the piston and the cylinder block, the slipper solid body thermal deformation under the temperature distributions shown in Fig. 5.14 enlarges the solid body proportionally. The surface deflection due to thermal load has rather a limited impact on the fluid film behavior in the slipper/swashplate interface. Therefore, comparing Fig. 5.10, Fig. 5.7, and Fig. 5.3, even though the thermal behavior is size-dependent, the slipper/swashplate interface size-dependence is mainly determined by the pressure distribution.

In order to understand the solid body temperature distribution, the fluid temperature distribution must be solved first. The energy equation that describes the convective-diffusive effects in the fluid domain is used to solve for the fluid temperature distribution:

$$\nabla \cdot (\rho \mathbf{V} T - \Gamma \nabla T) = S \tag{5.24}$$

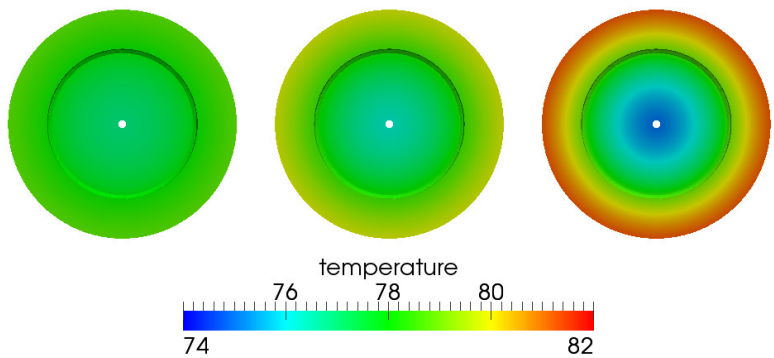

Fig. 5.14. Slipper temperature distribution comparison for different sizes (scaled viscosity).

where the diffusion coefficient is:

$$\Gamma = \frac{\kappa_{fluid}}{c_p} \tag{5.25}$$

and the source term S is:

$$S = \frac{\mu}{c_p}\left(\frac{\partial v}{\partial h}\right)^2 \tag{5.26}$$

Integrating the energy equation over a volume and applying the divergence theorem:

$$\int_A (\rho \mathbf{V} T - \Gamma \nabla T) \cdot dA\mathbf{n} = \int_V S dV \tag{5.27}$$

With scalable dimensions, the source term S becomes:

$$S(\lambda) = \frac{\mu(\lambda)}{c_p}\Phi_d(\lambda) = \frac{\mu_0}{c_p}\lambda^{-2}\Phi_{d0} = \lambda^{-2}S_0 \tag{5.28}$$

Then the energy equation for the scaled fluid domain yields:

$$\int_A (\rho \mathbf{V} T(\lambda) - \Gamma \nabla T(\lambda)) \cdot \lambda dA_0\mathbf{n} = \int_V S_0 dV_0 \tag{5.29}$$

By comparing Eq. 5.29 to Eq. 5.27, it can be concluded that the temperature distribution in the fluid domain is not linearly scalable.

The governing energy equation for the three-dimensional heat transfer problem is commonly written as the sum of the convective part and the conductive part:

$$\nabla \cdot (\mathbf{q}_{cv} + \mathbf{q}_{cd}) = 0 \tag{5.30}$$

For a control volume, the energy equation yields:

$$\int_A \mathbf{q}_{cv} \cdot \mathbf{n} dA + \int_V \nabla \cdot \mathbf{q}_{cd} dV = 0 \tag{5.31}$$

There are two types of convection boundaries commonly applied to the solid body surfaces:

Neumann boundary condition: The Neumann condition is applied to the running surfaces of the lubricating interface, where the heat flux into each of the solid parts adjacent to the fluid can be calculated as the energy dissipation, minus the energy taken away with the passing flow.

$$\mathbf{q}_{cv} \cdot \mathbf{n} dA = \frac{1}{2} \left[\int_V \mu \Phi_d dV - \int_S c_p \rho \mathbf{V} T \cdot \mathbf{n} dS \right] \tag{5.32}$$

Mixed boundary condition: The mixed condition is applied on the surfaces where the temperature of the surrounding environment is constant. The heat flux of the mixed condition can be calculated using the solid body surface temperature, the temperature of the surrounding environment, and a heat transfer coefficient.

$$\mathbf{q}_{cv} \cdot \mathbf{n} dA = h \left(T_S - T_\infty \right) dA \tag{5.33}$$

The conductive part of the energy equation yields:

$$\int_V \nabla \cdot \mathbf{q}_{cd} dV = \int_V \nabla \cdot \left(-\kappa_{solid} \nabla T \right) dV \tag{5.34}$$

When use scalable dimensions, the Neumann type convection boundary becomes:

$$\mathbf{q}_{cv} \left(\lambda \right) \cdot \mathbf{n} dA \left(\lambda \right) = \frac{1}{2} \left[\int_V \mu \left(\lambda \right) \lambda^{-2} \Phi_{d0} \lambda^3 dV_0 - \int_S c_p \rho \mathbf{V} T \cdot \mathbf{n} \lambda^2 dS_0 \right] \tag{5.35}$$

The mixed type convection boundary becomes:

$$\mathbf{q}_{cv} \left(\lambda \right) \cdot \mathbf{n} dA \left(\lambda \right) = h \left(T_S - T_\infty \right) \lambda^2 dA_0 = \lambda^2 \mathbf{q}_{cv0} \cdot \mathbf{n} dA_0 \tag{5.36}$$

The conductive term of the energy equation scales as:

$$\int_V \nabla \cdot \left(-\kappa_{solid} \nabla T\left(\lambda\right)\right) dV\left(\lambda\right) = \lambda^2 \int_V \nabla \cdot \left(-\kappa_{solid} \nabla T\left(\lambda\right)\right) dV_0 \tag{5.37}$$

Eq. 5.35, Eq. 5.36, and Eq. 5.37 show that the scaled solid body parts will result in a different dimensional heat transfer performance than when using linear scaling.

So far, the analytical investigation of the temperature distribution in both the fluid domain and the solid domain proved that the thermal characteristic of the lubricating interface is not scalable. For the purposes of scientific research, the artificial size-dependent viscosity in Eq. 5.22 was used in Eq. 5.28.

$$S\left(\lambda\right) = \lambda^{-1} S_0 \tag{5.38}$$

Then the energy equation for the scaled fluid domain yields:

$$\int_A \left(\rho \mathbf{V} T\left(\lambda\right) - \Gamma \nabla T\left(\lambda\right)\right) \cdot dA_0 \mathbf{n} = \int_V S_0 dV_0 \tag{5.39}$$

To keep the temperature distribution consistent in the scaled fluid domain, the temperature and the temperature gradient scale as:

$$\begin{aligned} T\left(\lambda\right) &= T_0 \\ \nabla T\left(\lambda\right) &= \lambda^{-1} \nabla T_0 \end{aligned} \tag{5.40}$$

Eq. 5.39 then becomes:

$$\int_A \left(\rho \mathbf{V} T_0 - \Gamma \lambda^{-1} \nabla T_0\right) \cdot dA_0 \mathbf{n} = \int_V S_0 dV_0 \tag{5.41}$$

Eq. 5.41 shows that consistency in the temperature distribution can be achieved if the fluid is not only given the viscosity of Eq. 5.22, but also the following fluid diffusion coefficient:

$$\Gamma\left(\lambda\right) = \lambda \Gamma_0 \tag{5.42}$$

A similar approach can be used for the three-dimensional solid body heat transfer analysis. Applying Eq. 5.22 to Eq. 5.35:

$$\begin{aligned} \mathbf{q}_{cv}\left(\lambda\right) \cdot \mathbf{n} dA\left(\lambda\right) &= \frac{1}{2} \left[\int_V \lambda \mu_0 \lambda^{-2} \Phi_{d0} \lambda^3 dV_0 - \int_S c_p \rho \mathbf{V} T \cdot \mathbf{n} \lambda^2 dS_0 \right] \\ &= \lambda^2 \mathbf{q}_{cv0} \cdot \mathbf{n} dA_0 \end{aligned} \tag{5.43}$$

Then, together with Eq. 5.36, the convective term of the energy equation scales as:

$$\mathbf{q}_{cv}(\lambda) \cdot \mathbf{n} dA(\lambda) = \lambda^2 \mathbf{q}_{cv0} \cdot \mathbf{n} dA_0 \tag{5.44}$$

Substituting Eq. 5.44 and Eq. 5.37 into Eq. 5.31:

$$\lambda^2 \int_A \mathbf{q}_{cv0} \cdot \mathbf{n} dA_0 + \lambda^2 \int_V \nabla \cdot (-\kappa_{solid} \nabla T(\lambda))\, dV_0 = 0 \tag{5.45}$$

Consistency of the temperature distribution in the scaled solid domain can be achieved if the solid parts conductivity scales with the first order linear scaling factor:

$$\kappa_{solid}(\lambda) = \lambda \kappa_{solid\_o} \tag{5.46}$$

In order to verify the analysis for the temperature distribution in the fluid and solid domains, the simulation cases A, B, and C are reconfigured to reflect Eq. 5.22, Eq. 5.42, and Eq. 5.46. Since the fluid diffusion coefficient is a function of fluid conductivity κ_{fluid}, and the fluid heat capacity c_p, in this study, the fluid conductivity was changed with the linear scaling factor, while the heat capacity remains the same. The simulation inputs for cases A, B, and C become those shown in Table 5.2.3.

Figure 19, 20, and 21 show the simulated temperature distribution of the piston, the cylinder block, and the slipper using the artificially scaled fluid viscosity, fluid conductivity, and solid body conductivity as specified in Table 3. The simulations are conducted with all the fluid and structure physical phenomena, including heat transfer in the fluid and solid domains. The solid bodies temperature distribution demonstrates that the fluid and solid body heat transfer is no longer size-dependent when the fluid viscosity, and the fluid and solid conductivities, are artificially scaled with the unit size.

Fig. 5.18, Fig. 5.19, and Fig. 5.20 show the normalized energy dissipation, the normalized leakage, and the normalized torque loss of the piston/cylinder interface, the cylinder block/valve plate interface, and the slipper/swashplate interface from the simulations A, B, and C, as shown in Table. 5.2.3.

Table 5.3.
Summary of operating conditions with scaled fluid viscosity, scaled fluid conductivity, and scaled solid conductivity.

	A	B	C
linear factor λ	0.5	1	2
Unit size [cc]	9.375	75	600
Pressure [bar]	400	400	400
Displacement [%]	100	100	100
Speed [rpm]	7200	3600	1800
Fluid viscosity	$0.5 \cdot \mu_0$	μ_0	$2 \cdot \mu_0$
Fluid conductivity	$0.5 \cdot \kappa_{fluid\_0}$	κ_{fluid_0}	$2 \cdot \kappa_{fluid\_0}$
Solid conductivity	$0.5 \cdot \kappa_{solid\_0}$	κ_{solid_0}	$2 \cdot \kappa_{solid\_0}$

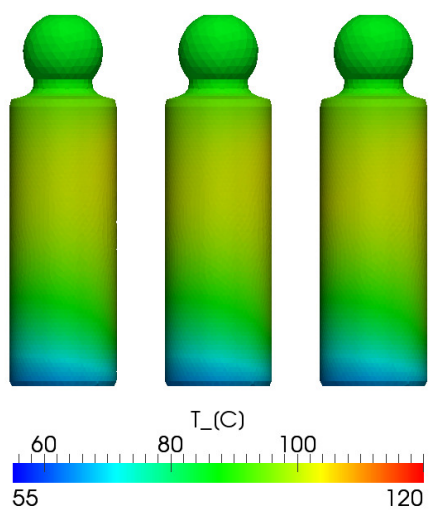

Fig. 5.15. Piston temperature distribution comparison for different sizes (scaled viscosity, scaled fluid and solid conductivity).

According to Fig. 5.18, the normalized energy dissipation and normalized torque loss of the piston/cylinder interface from cases A, B, and C are almost identical for

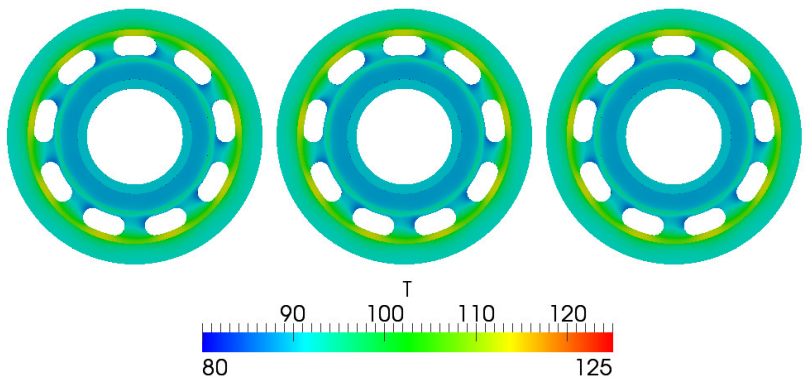

Fig. 5.16. Cylinder block temperature distribution comparison for different sizes (scaled viscosity, scaled fluid and solid conductivity).

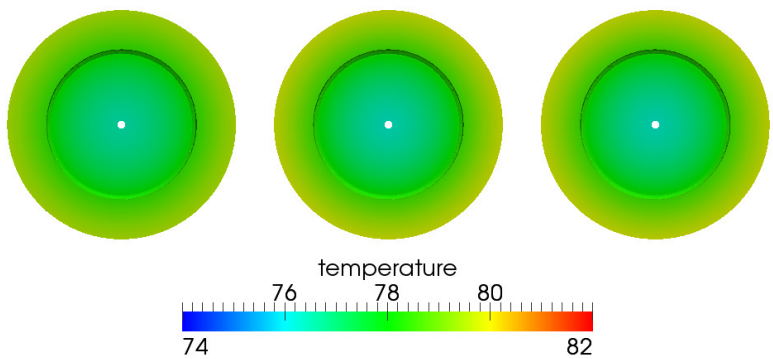

Fig. 5.17. Slipper temperature distribution comparison for different sizes (scaled viscosity, scaled fluid and solid conductivity).

the unit sizes, which differ in size by a factor of 64 from the smallest to the largest. The normalized leakages, even though not identical, are very close to each other.

Fig. 5.19 shows that the cylinder block/valve plate interface of cases A, B, and C behaves very similarly. Both the magnitude and the shape of the normalized energy dissipation, the normalized leakage, and the normalized torque loss are very close to each other across the different sizes.

Similarly to the piston/cylinder interface, Fig. 5.20 shows that the normalized energy dissipation and normalized torque loss of slipper/swashplate interfaces from

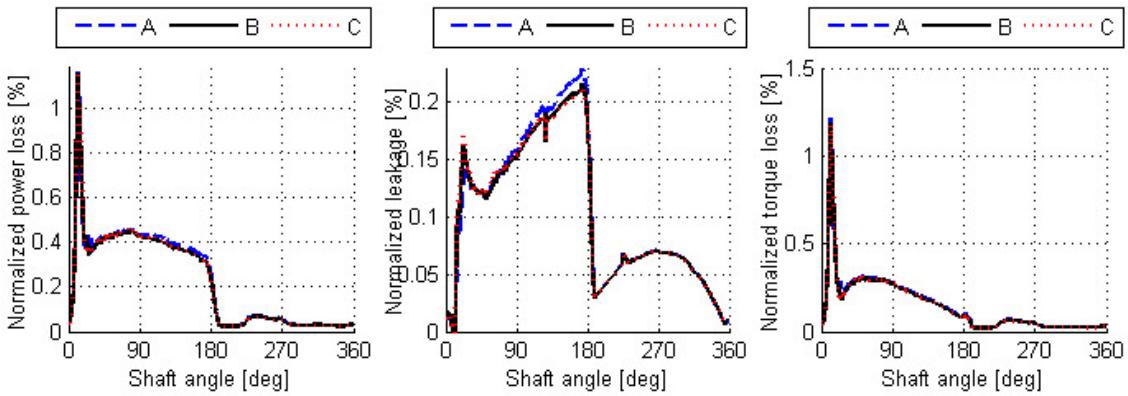

Fig. 5.18. Normalized piston/cylinder interface performance for different sizes (scaled viscosity, scaled fluid and solid conductivity).

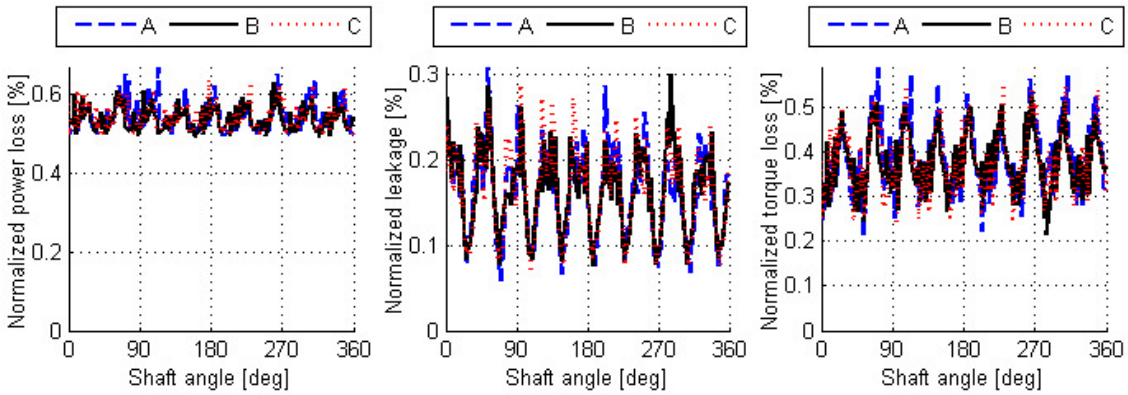

Fig. 5.19. Normalized cylinder block/valve plate interface performance for different sizes (scaled viscosity, scaled fluid and solid conductivity).

cases A, B, and C are almost identical. The normalized leakages, even though are not identical, are very close to each other.

Fig. 5.15 to Fig. 5.20 show that the size-dependence of the performance of the axial piston machine can be eliminated by artificially scaling the fluid viscosity, the fluid conductivity, and the solid conductivity. The reason that the common practice, which is to proportionally scale an axial piston machine design to larger or smaller sizes, cannot achieve the pre-scaled performance can be found in the presented analysis

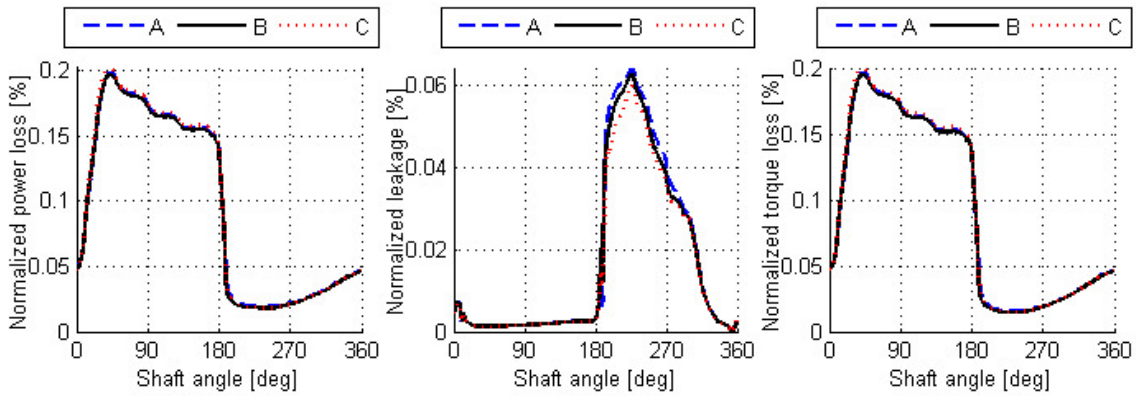

Fig. 5.20. Normalized slipper/swashplate interface performance for different sizes (scaled viscosity, scaled fluid and solid conductivity).

and simulation studies, which show the size-dependent pressure distribution and the size-dependent multi-domain heat transfer.

5.3 Findings and scaling guides

According to Fig. 5.1 to Fig. 5.3, by proportionally scaling the axial piston machine, the performance of the three lubricating interfaces does not match the pre-scaled one, which agrees with the result published before [45, 46]. The reasons, found through the analysis and demonstrated through the simulation, are that:

- Pressure distribution and heat transfer in both the fluid domain and the solid domain are the only contributions to the size-dependence of the axial piston machines lubricating interface performance.
- As long as the pressure distribution and temperature distribution are proportionally scaled, the deformation due to the pressure and thermal load stays constant, and therefore does not contribute to the size-dependence of the lubricating interface performance.

From the analysis conducted, it is also can be found that:

- A size-independent fluid pressure distribution can be achieved by scaling the viscosity with the linear scaling factor. The simulation results in Fig. 5.5 to Fig. 5.7 demonstrated this by showing an identical normalized performance for all three lubricating interfaces when using a scaled viscosity and no heat transfer. Since the viscosity can not be scaled artificially according to the linear scaling factor in the real life, non-scalable viscosity contributes to the size-dependence of the performance of lubricating interfaces.

- The size-independent temperature distribution in both the fluid and solid domains can be achieved by scaling the fluid and solid conductivity with the linear scaling factor. The simulation results in Fig. 5.15 to Fig. 5.20 demonstrated this by showing an identical normalized performance for all three lubricating interfaces with a scaled viscosity and conductivity. Since the thermal conductivity can not be scaled artificially according to the linear scaling factor in the real life, non-scalable thermal behavior contributes to the size-dependence of the performance of lubricating interfaces.

From the findings of the analysis and simulation studies, the following scaling guide for all three lubricating interfaces emerges:

- When scaling an swashplate type axial piston machines to a different size, the size-dependent pressure distribution-induced performance bias can be eliminated by using hydraulic fluid at a different viscosity grade.
  - Use higher viscosity for up-scaling.
  - Use lower viscosity for down-scaling.
  - Choose the viscosity based on the linear scaling factor as in Eq. 5.22.
- The viscosity of the fluid can also be controlled by:
  - Increasing operating temperature for down-scaling
  - Decreasing operating temperature for up-scaling.

- When using a fluid of different viscosity is not feasible, design modifications should compensate for the size-dependent sealing function of the scaled lubricating interfaces:
  - For the piston/cylinder interface, use a lower normalized clearance for up-scaling, and use a higher normalized clearance for down-scaling [46].
  - For the cylinder block/valve plate interface, increase the sealing land area for up-scaling, and decrease the sealing land area for down-scaling [45].
  - For the slipper/swashplate interface, increase the sealing land area for up-scaling, and decrease the sealing land area for down-scaling.
- To compensate for the size-dependent heat transfer, the design of the lubricating interfaces needs to be modified:
  - When up-scaling, the lubricating interface design should be modified to increase the cooling performance of the lubricating gap, e.g. adding a flow channel beneath the valve plate to smooth the temperature distribution.
  - When down-scaling, the lubricating interface design should be modified to create more thermal deformation, e.g. by using a bi-material solid body [47].

Even though the simulation studies shown pertain to the fluid-structure and thermal interaction model for all the three lubricating interfaces in a swashplate type axial piston machine, the analytical study is not limited to a single type of hydraulic pump. The findings will hold true for not only the tribological interfaces in axial piston machines, radial piston machines, internal and external gear pumps and motors, gerotors, and vane pumps, but also for all the thermoelastohydrodynamic tribological interfaces in bearings and seals.

5.4 Conclusions

This chapter presented an analytical study of the size-dependence of thermoelastohydrodynamic tribological interfaces. The physical phenomena that were studied include the hydrostatic and hydrodynamic pressure distributions, the heat transfer and heat generation in the fluid film, the heat transfer in the solid domain, and the solid body deformation due to both the pressure loading and the thermal loading.

The analysis indicates that the pressure distribution in the lubricating gap, and the heat transfer in the fluid and in the solid bodies are the only size-dependent physical phenomena; therefore, they are the only contributors to the performance change of the thermoelastohydrodynamic tribological interfaces in response to scaling.

A state-of-the-art fluid-structure-thermal interaction model for the three lubricating interfaces in axial piston machines was used to demonstrate the consequences of the analytical study. Three different pump sizes were modeled in a series of simulation studies, the largest of which is 64 times bigger than the smallest. These simulation studies verified the findings of the analysis, and allowed for the creation of a general guide to scaling aimed at maintaining the efficiency of the original unit. This scaling guide enables pump manufacturers to apply the developed scaling laws, and efficiently generate scaled pump designs of much higher efficiency than the traditional approach of linear scaling allows for.

6. A PATH TOWARD AN EFFECTIVE PISTON/CYLINDER INTERFACE SCALING

In this chapter, the piston/cylinder interface is studied for three different sizes (9.375 cc, 75 cc, and 600 cc) at multiple operating conditions. The piston/cylinder clearance, the length of the piston guide, the material, and the groove profiles are investigated and a nonlinear scaling rule for piston/cylinder interface is proposed which allows to maintain the volumetric efficiency of the scaled interface very close to the original size, and to keep energy efficiency of the up-scaled interface above the value for the original size.

6.1 Piston/cylinder interface fluid film

The piston/cylinder interface in swash plate type axial piston machines is the most complicated tribological interface. Unlike the slipper/swash plate interface and cylinder block/valve plate interface, the hydrostatic pressure force in the piston/cylinder interface does not assist the bearing function. Instead, the balancing of the external forces and moments rely on the hydrodynamic effect. The periodically oscillating external forces and moments lead to a complex micromotion of the piston. The piston changes its eccentricity and the inclination angle in the cylinder bore till the resulting hydrodynamic pressure force balance the external forces. Fig. 6.1 shows an example of an inclined piston position in the cylinder bore.

Fig. 6.2 shows an unwrapped fluid film between the piston and the cylinder bore of an axial piston machine at a shaft angle of 135 degrees when the unit is operating at the maximum speed, the maximum pressure, and the maximum swash plate angle. The gap height shown in this figure is normalized to its original clearance. The running surface deforms under the pressure and the thermal loading and influences

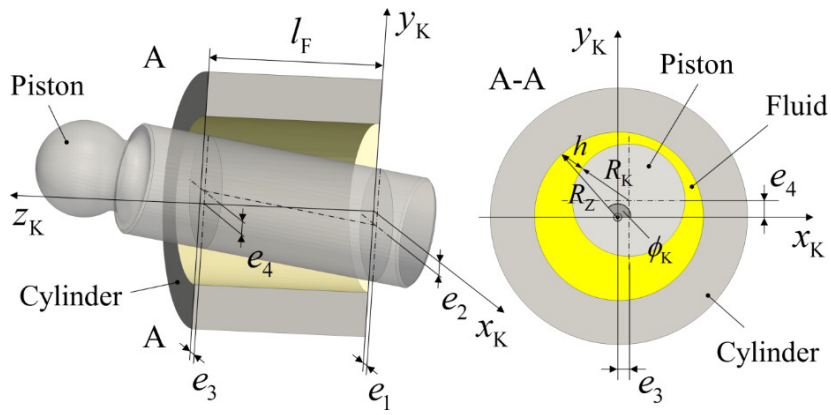

Fig. 6.1. Inclined piston in cylinder bore forming the fluid film.

the resulting film thickness. That is the reason that the maximum film thickness shown in Fig. 6.2 is larger than the value of the clearance. The resulting film thickness can be described as a sum of the gap height from the given clearance and position of the piston inside the bore, the total deformation of piston and cylinder $\Delta h_{g\_def\_p}$ due to pressure, and the total deformation of piston and cylinder $\Delta h_{g\_def\_th}$ due to thermal loading:

$$h_g = h_{g\_rigid} + \Delta h_{g\_def\_p} + \Delta h_{g\_def\_th} \tag{6.1}$$

The total deformations of the piston and the cylinder bore due to pressure defor-

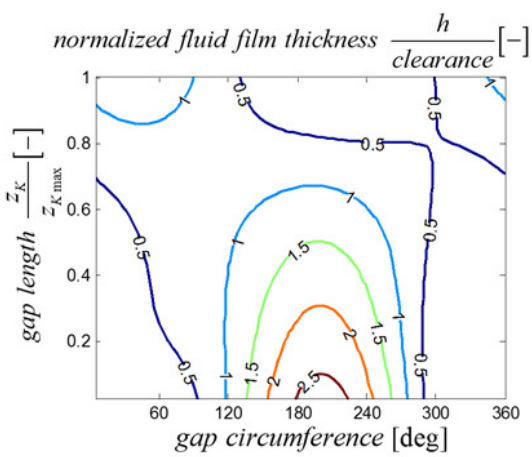

Fig. 6.2. Film thickness for the unwrapped gap without pressure and thermal deformations.

mation $\Delta h_{g\_def\_p}$ and the total deformation of the piston and the cylinder bore due to thermal loading $\Delta h_{g\_def\_th}$ are calculated according to Eq. 6.2. The sign convention in Eq. 6.2 is based on the following definition: Positive values of the pressure deformation of the piston $\Delta h_{g\_def\_p\_K}$, the positive value of the pressure deformation of the cylinder bore$\Delta h_{g_def_p_B}$, and the positive value of the thermal deformation of the cylinder bore$\Delta h_{g_def_th_B}$ increase film thickness of the interface, while a positive value of the thermal deformation of the piston $\Delta h_{g\_def\_p\_K}$ reduces the resulting film thickness.

$$\begin{aligned} \Delta h_{g\_def\_p} &= \Delta h_{g\_def\_p\_K} + \Delta h_{g\_def\_p\_B} \\ \Delta h_{g\_def\_th} &= -\Delta h_{g\_def\_th\_K} + \Delta h_{g\_def\_th\_B} \end{aligned} \tag{6.2}$$

Fig. 6.3 shows the resulting change of film thickness $\Delta h_{g\_def\_p}$ due to the pressure deformation of both the piston and the cylinder bore normalized to the original clearance.

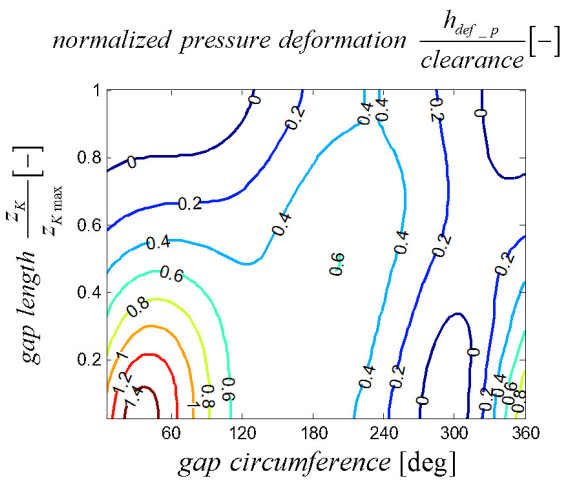

Fig. 6.3. The resulting change of film thickness $\Delta h_{g_def_p}$due to pressure deformation.

In Fig. 6.4, the resulting change in film thickness due to the thermal deformation of the piston and the cylinder bore $\Delta h_{g\_def\_th}$ is plotted. Again the values of resulting thermal deformation are normalized to the original clearance.

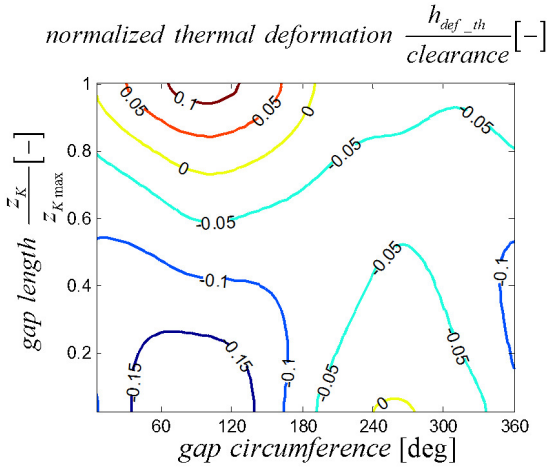

Fig. 6.4. The resulting change of film thickness $\Delta h_{g\_def\_th}$ due to thermal deformation.

Fig. 6.2, Fig. 6.3, and Fig. 6.4 indicate that the deformation due to both the pressure and the thermal load has a significant impact on the resulting fluid film thickness. According to the conclusion in chapter 5, the pressure and the thermal deformation represent different characteristic when scaling, mainly due to the dissimilarity of the pressure distribution and temperature distribution. On the path toward the effective scaling approach, the piston/cylinder interface design parameters such as the clearance, the piston guide length, and the material are studied with the consideration of these deformations.

6.2 Clearance and piston guide length study

According to the analytical study in chapter 5, merely scale the piston/cylinder interface proportionally can never achieve the goal of the effective scaling, which is to keep the performance as the pre-scaled size, by physics. Therefore, the effective scaling practice requires nonlinearly scaled design parameters to compensate the physics-based performance difference. The path toward the effective piston/cylinder interface scaling start from the understanding of the design parameters influence on the interface performance.

The piston/cylinder interface clearance is defined as the difference between the cylinder bore (or bushing) running surface inner diameter and the piston running surface outer diameter:

$$clearance = d_B - d_K \tag{6.3}$$

To study the clearance for different sizes, the piston/cylinder interface clearance is normalized to the piston diameter:

$$norm.clearance = \frac{d_B - d_K}{d_K} \tag{6.4}$$

The piston guide length is the axial length of the running surface of the cylinder bore or the bushing. When the design allows the end of piston running surface moves into the cylinder bore running surface, the length of the lubricating gap then controlled by the piston position, and therefore, varies with the piston position. Figure 7.5 shows an example of piston a guide length.

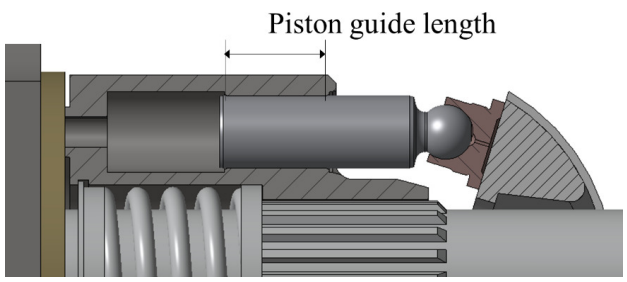

Fig. 6.5. Piston guide length.

In this study, the nominal piston guide length is studied together with 80% of the nominal length and 120% of the nominal length. The normalized clearance is varied from 0.9 per mil to 2.1 per mil. The studied operating conditions are listed in Table 6.2:

Fig. 6.6 to Fig. 6.9 show the normalized energy dissipation and normalized leakage flow rate from all the piston/cylinder interfaces with different piston guide length and different clearance. Three different colors represent three different piston guide

Table 6.1.
Summary of operating conditions.

operating conditions	pressure	speed	displacement
OC #1	max	max	full
OC #2	max	28% of max	full
OC #3	12.5% of max	max	full
OC #4	12.5% of max	28% of max	full

lengths: 80%, 100%, and 120% of the nominal length. The x-axis shows the normalized clearance. The normalized energy dissipation uses the total theoretical output power as the reference and the normalized leakage flow rate uses the total theoretical outlet flow rate as the reference. The performance of the nominal piston guide length and nominal clearance is marked using the horizontal black line as the reference in these figures.

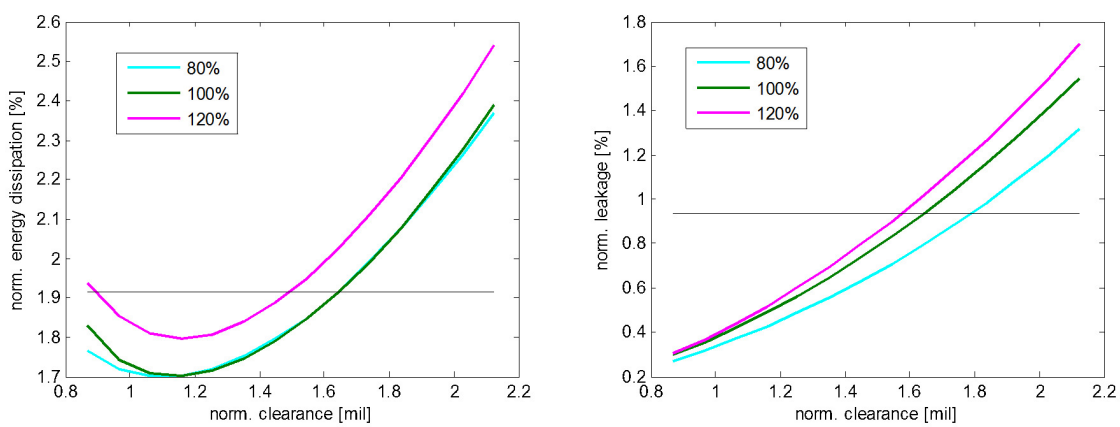

Fig. 6.6. Piston guide length and clearance influence on piston/cylinder interface performance at OC #1.

The positive correlation between the clearance and the leakage can be found through all four operating conditions. The longer piston guide length produces higher normalized leakage at high operating pressure (OC #1 and OC #2). The trend be-

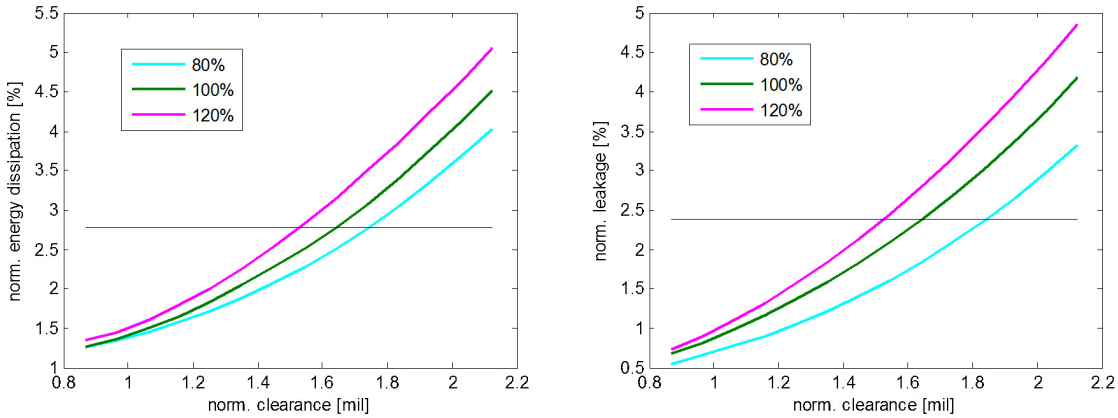

Fig. 6.7. Piston guide length and clearance influence on piston/cylinder interface performance at OC #2.

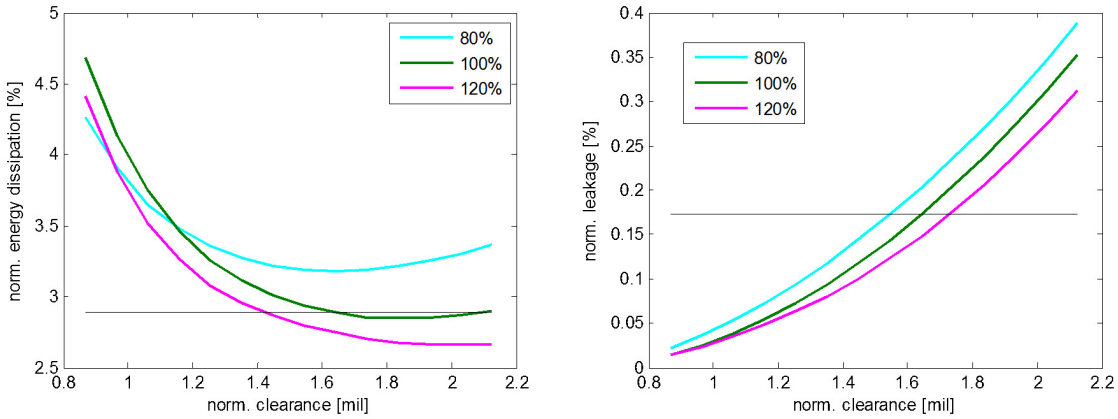

Fig. 6.8. Piston guide length and clearance influence on piston/cylinder interface performance at OC #3.

comes opposite at OC #3, which is lower pressure and high speed, and unclear at OC #4, which is lower pressure low speed. At the high pressure operating conditions, the inclination of the piston is contributing to the sealing function of the piston/cylinder interface. The longer piston guide length helps to generate hydrodynamic pressure force and reduces the piston inclination, therefore, increases the leakage. At the low pressure operating conditions, the piston barely inclined due to the low side load.

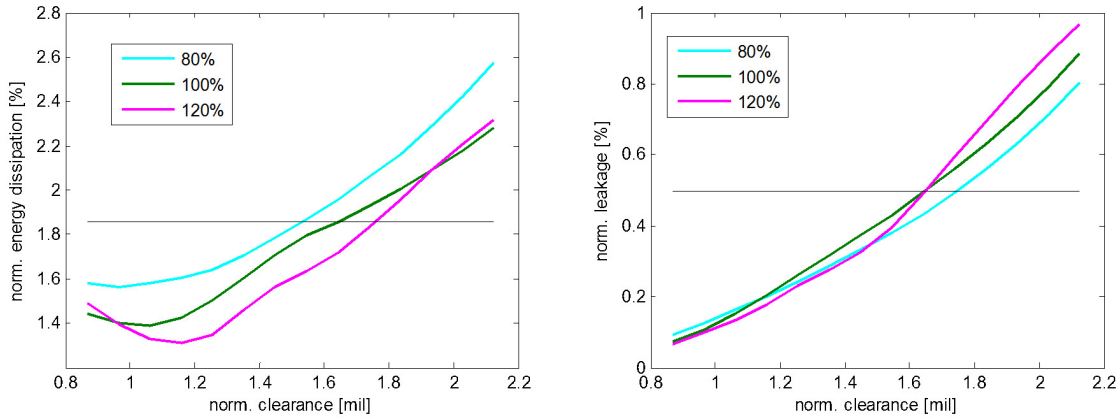

Fig. 6.9. Piston guide length and clearance influence on piston/cylinder interface performance at OC #4.

The longer piston guide length increases the sealing area, therefore, can reduce the leakage.

The leakage determines the energy dissipation in the piston/cylinder interface at high pressure and low speed operating point (OC #2). The trends of energy dissipation are very similar to the trends of leakage. In OC #3, due to the low pressure and high speed, the energy dissipation is dominated by the friction, therefore decreases with the increasing clearance. The shorter piston guide length results in more piston inclination, and therefore more viscous friction. The maximum power operating condition OC #1 is the combination of OC #2 and OC #3. The energy dissipation decreases with the increasing clearance at the beginning and then increases with the clearance when the leakage starts to dominate the power loss.

6.3 Piston material study (temperature adaptive piston design)

Besides the piston/cylinder interface geometry, the material also influences the lubricating fluid film behaviors. In this study, there are two piston designs have been investigated. One is a baseline piston design using steel as the material. As shown on the left side of Fig. 6.10, this baseline piston design features a hollow volume

inside of the piston body to reduce the piston mass while keep the dead volume of the displacement chamber low. The other one is a bi-material piston design, which uses the same steel piston body, but fills the hollow volume with aluminum. This study focuses on how aluminum thermal deformation influence the piston/cylinder interface performance at different operating temperatures.

Table 6.2.
Summary of operating conditions.

	#1	#2	#3	#4	#5	#6
T_{in} [°C]	100	100	52	52	-20	-20
T_{out} [°C]	106	106	58	58	-14	-14
T_{case} [°C]	121	121	77	77	34	34
$Speed$ [rpm]	3600	1800	3600	1800	3600	1800

Since this study is focusing on the thermal behaviors of the piston/cylinder interface, three sets of operating temperatures have been selected, as shown in Table. 6.3. Together with two speeds: full and half speed, totally six operating conditions have been studied in this case.

Fig. 6.11 shows how both the baseline piston and the bi-material piston deform under thermal load. On the left side, the thermal deformation comparison is shown between the baseline piston and the bi-material piston when operating at -20C inlet

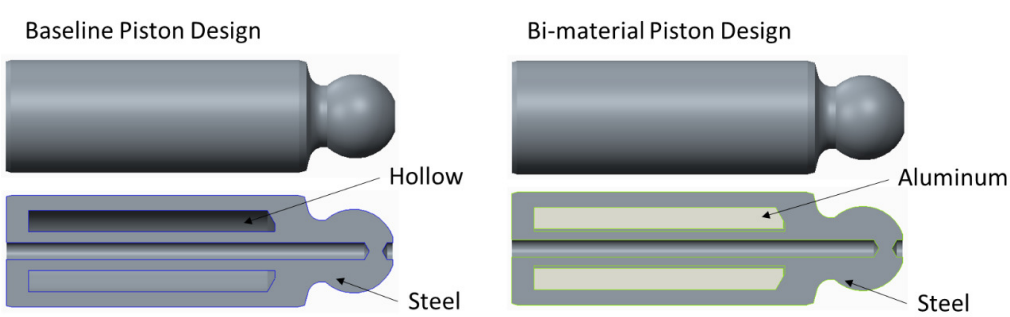

Fig. 6.10. Baseline piston design vs Bi-material piston design.

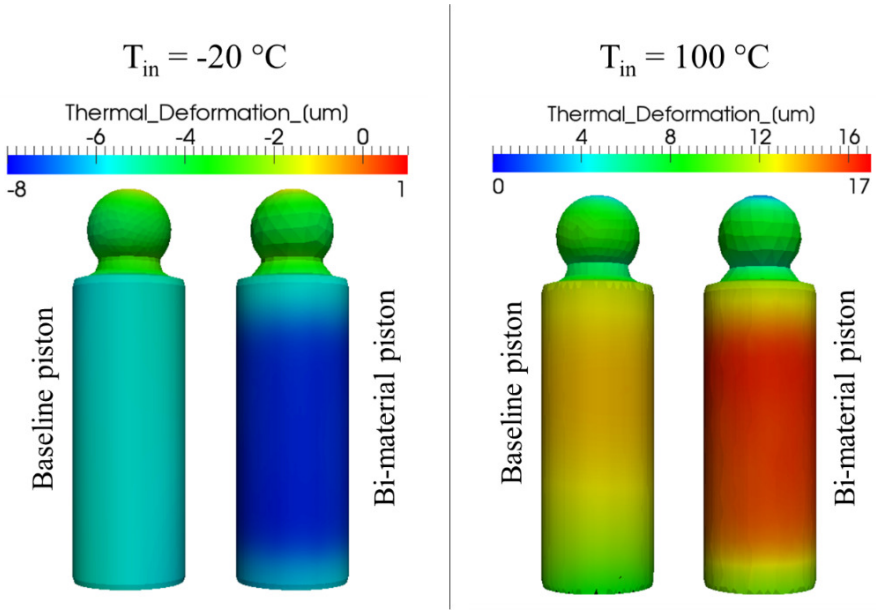

Fig. 6.11. Thermal deformation comparison between the baseline design and the bi-material design.

flow temperature. This figure shows that the bi-material piston shrinks 6 microns more than the baseline piston at low temperature operating condition. The right side of Fig. 6.11 shows the deformation comparison between the baseline piston and the bi-material piston when operating at 100C inlet flow temperature. This figure shows that the bi-material piston expands 4 microns more than the baseline piston at high temperature operating conditions.

Fig. 6.12 to Fig. 6.17 show the total energy dissipation Φ, the power loss due to leakage P_{SQ} and the power loss due to the axial friction P_{ST} of both the baseline design and the bi-material design for one of the nine piston/cylinder interfaces at the six operating conditions. The bi-material design shows the overall advantage over the baseline design due to the temperature adaptive gap height controlled by the piston thermal deformation. The bi-material piston utilizes the high thermal expansion property of aluminum, reduces the gap height at high temperature, when the leakage dominates the total power loss, and increases the gap height at low temperature,

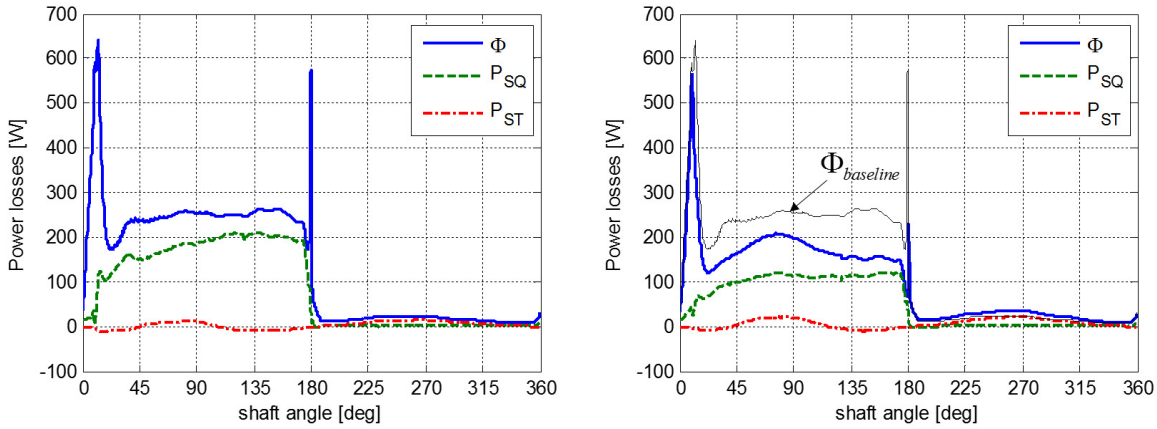

Fig. 6.12. baseline piston vs bi-material design at 100°C half speed.

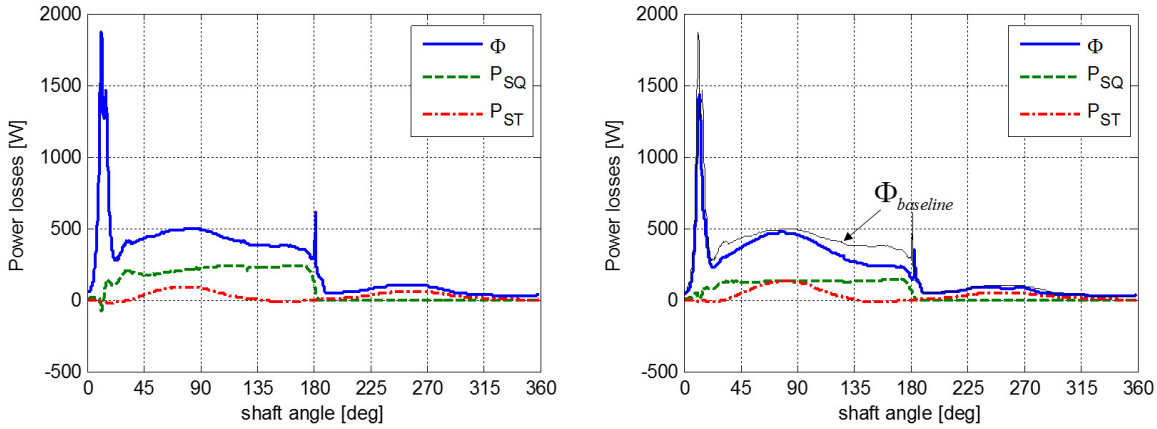

Fig. 6.13. baseline piston vs bi-material design at 100°C full speed.

when the friction dominates the total power loss. The temperature adaptive behavior of the bi-material piston is studies in more detail by Shang and Ivantysynova [47].

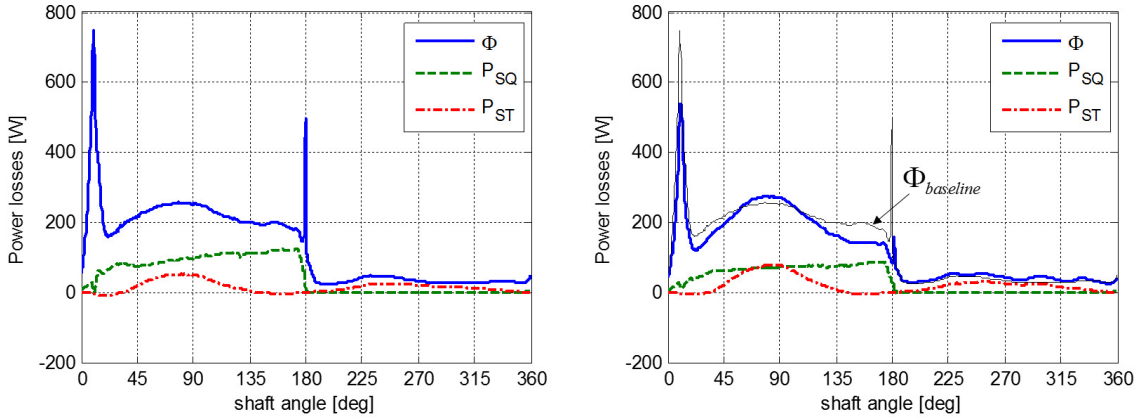

Fig. 6.14. baseline piston vs bi-material design at 52°C half speed.

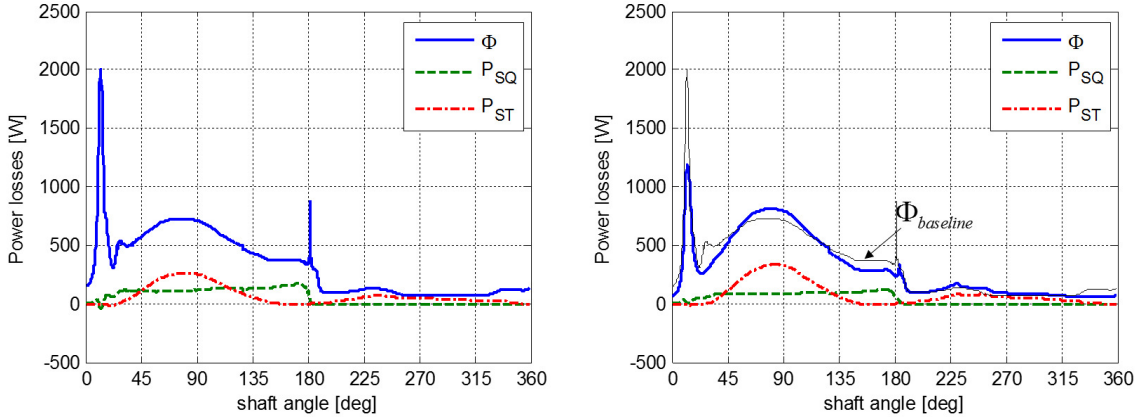

Fig. 6.15. baseline piston vs bi-material design at 52°C full speed.

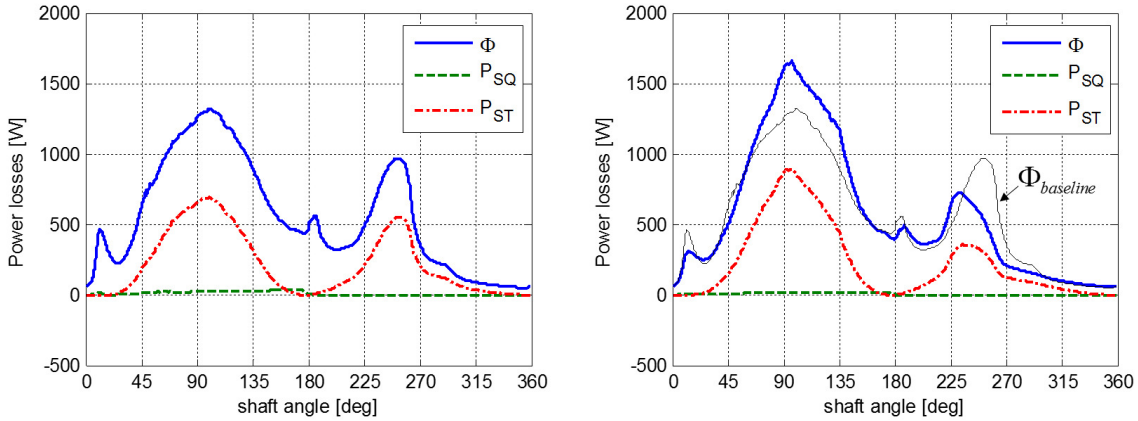

Fig. 6.16. baseline piston vs bi-material design at -20°C half speed.

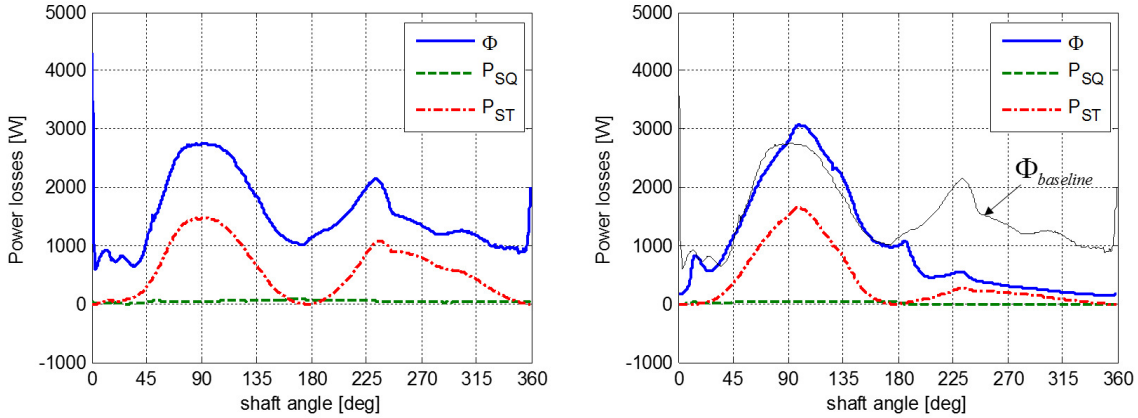

Fig. 6.17. baseline piston vs bi-material design at -20°C full speed.

6.4 Clearance-performance relationship at different sizes

Fig. 5.1 in previous chapter shows clearly that linearly scaled piston/cylinder interface is not able to achieve the same energy efficiency as the pre-scaled one. Further findings in chapter 5 indicate that the linearly up-scaled piston/cylinder interface will experience high leakage and low friction, while the linearly down-scaled piston/cylinder interface will experience low leakage and high friction. In the previous section of this chapter, the piston/cylinder clearance was found having a big impact on both the friction and leakage flow rate. In this section, the clearance influence on the piston/cylinder interface performance is discussed for three different sizes. Besides the original size, the bigger one was scaled according to the linear scaling factor $\lambda = 2$, and the smaller one was scaled down to $\lambda = 0.5$.

The operating conditions that is studied are listed in Table 6.2. Note that the maximum rotational speed scales with the reciprocal of the linear scaling factor . Therefore, for different sizes, the operating speed in the same operating condition has different absolute value.

Figure 7.18 to figure 7.21 show the clearance influence on the normalized energy dissipation and normalized leakage flow rate for the three sizes piston/cylinder interface at the four operating conditions.

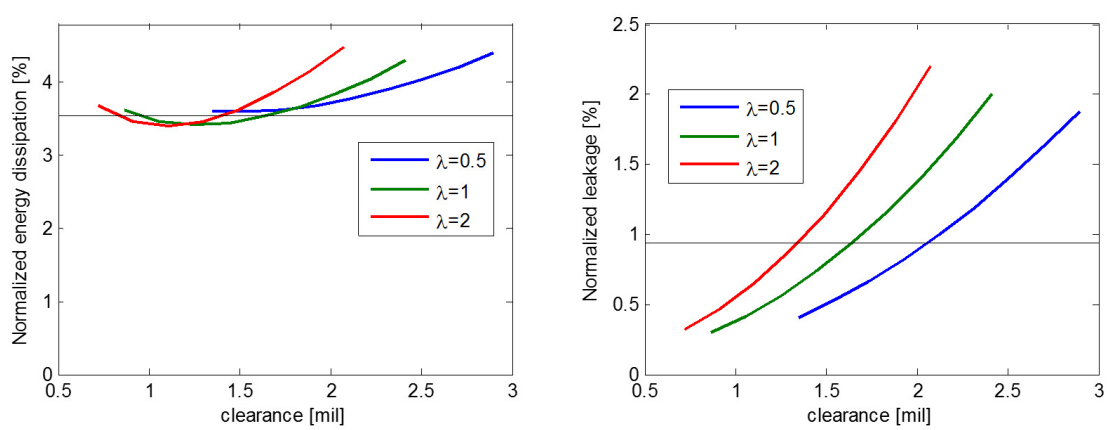

Fig. 6.18. Clearance influence on piston/cylinder interface performance at difference sizes at OC #1.

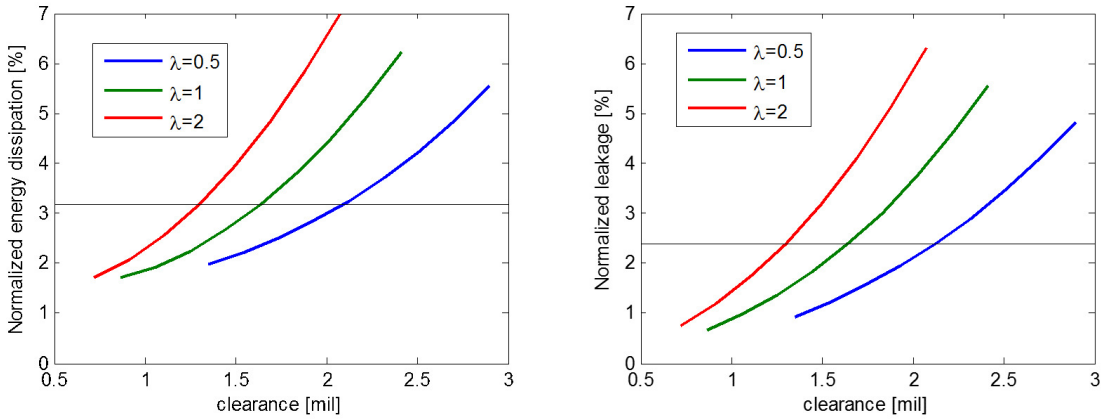

Fig. 6.19. Clearance influence on piston/cylinder interface performance at difference sizes at OC #2.

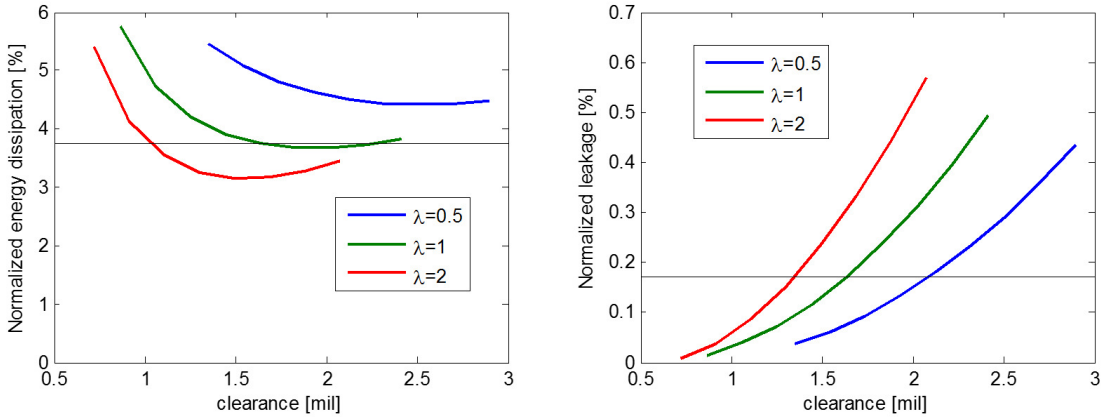

Fig. 6.20. Clearance influence on piston/cylinder interface performance at difference sizes at OC #3.

Again, in these figures, the normalized performance is contributed by all nine piston/cylinder interfaces. The performance reference, which is the normalized energy dissipation and the normalized leakage of the nominal design at original size, is marked using the thin horizontal black line in these figures. Fig. 6.18 to Fig. 6.21 show very similar normalized leakage flow rate trends. The curves suggest that, in order to achieve the reference normalized leakage flow rate, the up-scaled piston/cylinder interface should reduce the normalized clearance and the down-scaled piston/cylinder interface should increase the normalized clearance. The energy dissipation changes

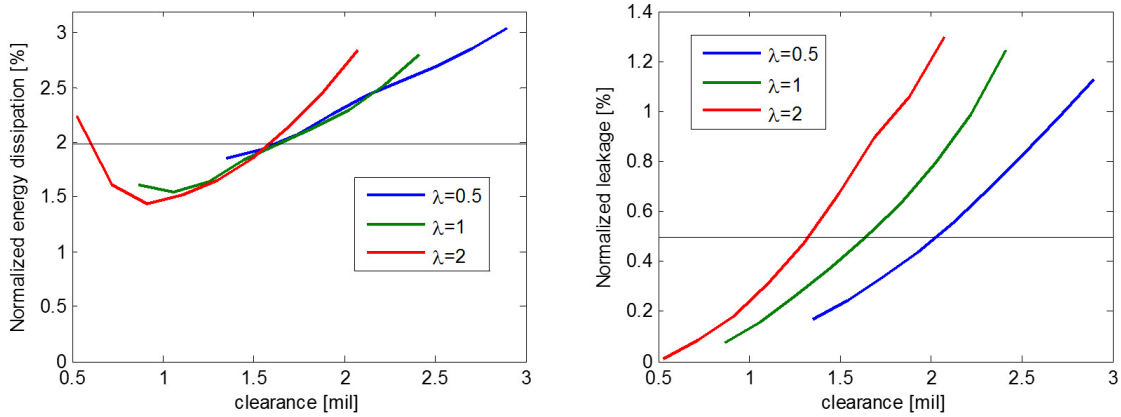

Fig. 6.21. Clearance influence on piston/cylinder interface performance at difference sizes at OC #4.

with normalized clearance differently at different operating conditions. At OC #2, due to the high operating pressure and low operating speed, the energy dissipation is dominated by the leakage flow rate, therefore, shows very similar trends as the leakage. At OC #3, due to the low operating pressure and high operating speed, the energy dissipation is dominated by the friction. In order to have the normalized energy dissipation closer to the reference, the up-scaled piston/cylinder interface should reduce the normalized clearance and the down-scaled piston/cylinder interface should increase the normalized clearance. However, at this operating condition, the down-scaled piston/cylinder interface always show higher normalized energy dissipation than the reference. At the maximum power operating condition OC #1, the energy dissipation curves are rather close to the reference. Again, the down-scaled piston/cylinder interface always have higher normalized energy dissipation than the reference at this operating condition. At the lowest power operating condition OC #4, all three curves cross the reference line at around the same location.

To conclude the findings in Fig. 6.18 to Fig. 6.21, by scaling the piston/cylinder clearance according to:

$$clearance = clearancee_0 \cdot \lambda^{-\frac{1}{3}} \tag{6.5}$$

The normalized leakage flow rate of the scaled piston/cylinder interface is very close to what the original size has. By using this scaling method, the up-scaled piston/cylinder interface will have the same or less normalized energy dissipation. However, the down-scaled piston/cylinder interface will still suffer from the high normalized energy dissipation.

6.5 Groove profile for down-scaled piston/cylinder interface

In order to achieve the same normalized energy dissipation of the down-scaled piston/cylinder interface as the pre-scaled level, the groove profile is introduced studied. The groove is defined as a ring-shaped groove profile on either piston running surface or cylinder bore (bushing) running surface that increase the gap height that the flow in the groove region is no longer laminar and the pressure in the groove region is uniform. Comparing the normal lubricating gap height which is the in the level of microns, the depth of the groove is in the level of micrometers.

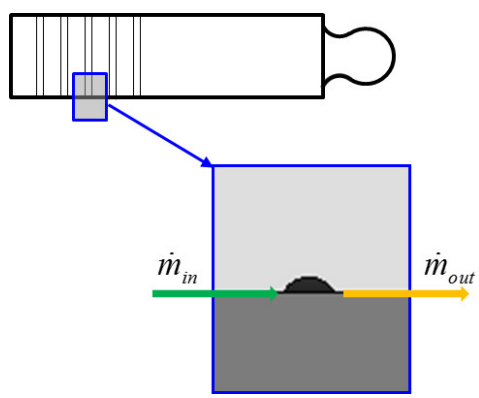

Fig. 6.22. Mass flow in and out of the groove control volume.

As shown in Fig. 6.22, the groove forms a control volume where the mass conservation can apply.

In the numerical model that calculates the gap pressure distribution, the mass flow rate in and out of the groove control volume can be calculated from the mass flow rate crossing the boundary cells. The boundary cells are shown in Fig. 6.23.

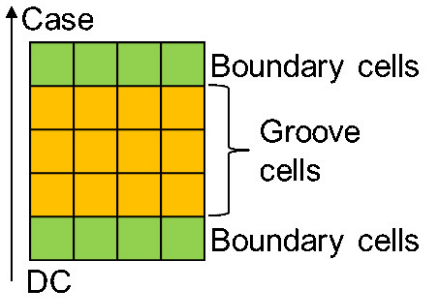

Fig. 6.23. Groove cells and boundary cells in the fluid domain grid.

The mass flow rate in the boundary cells can then be calculated from the pressure in the groove volume and the pressure distribution in the surrounding lubricating gap area. By applying the mass conservation in the groove volume, the pressure in the groove can be formulated as a function of the pressure, viscosity, density, and boundary surface sliding velocity of the boundary cells.

This relationship is added into the diffusive coefficients of the linear system that calculates the lubricating gap pressure distribution in the numerical model and updated every time when the Reynolds equation was solved in the non-grooved region as shown in Fig. 6.24.

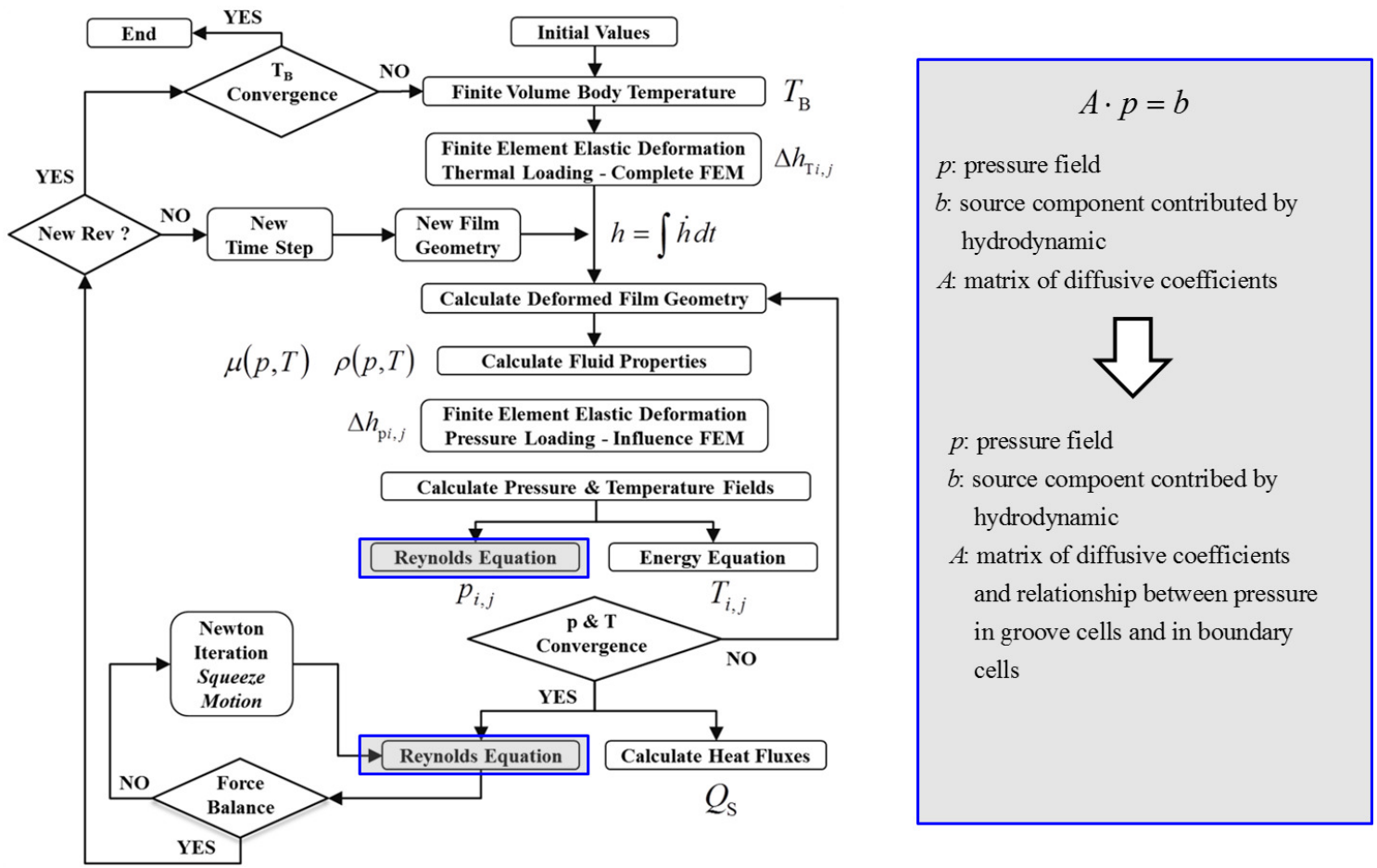

Fig. 6.24. Pressure distribution calculation scheme with groove profile.

In this case study, two groove profiles are investigated. As shown in Fig. 6.25, both grooves are on the cylinder bore running surface. One profile places the groove at one-third of the total piston guide length from the displacement chamber end, labeled groove 1/3, another profile has the groove located at one-eighth of the total piston guide length from the displacement chamber end, labeled groove 1/8. Both groove profiles and the baseline cylindrical piston/cylinder interface are simulated with different clearances at the four operating conditions. Note that all three designs were studied for the smaller piston/cylinder interface, which has $\lambda = 0.5$.

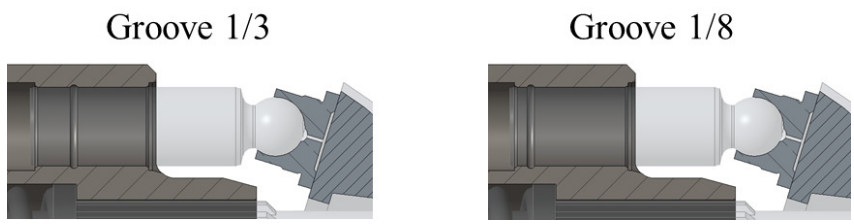

Fig. 6.25. Two types of groove profiles.

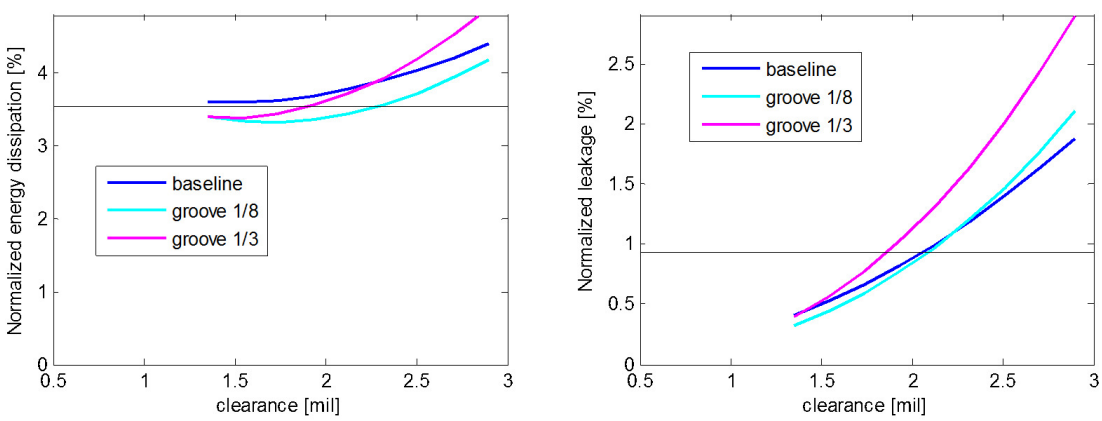

Fig. 6.26. Grooved piston/cylinder interface performance comparing to the baseline design for the small size with different clearance at OC #1.

Fig. 6.26 to Fig. 6.29 show the normalized energy dissipation and normalized leakage flow rate changes with the clearance for the cylindrical piston/cylinder interface

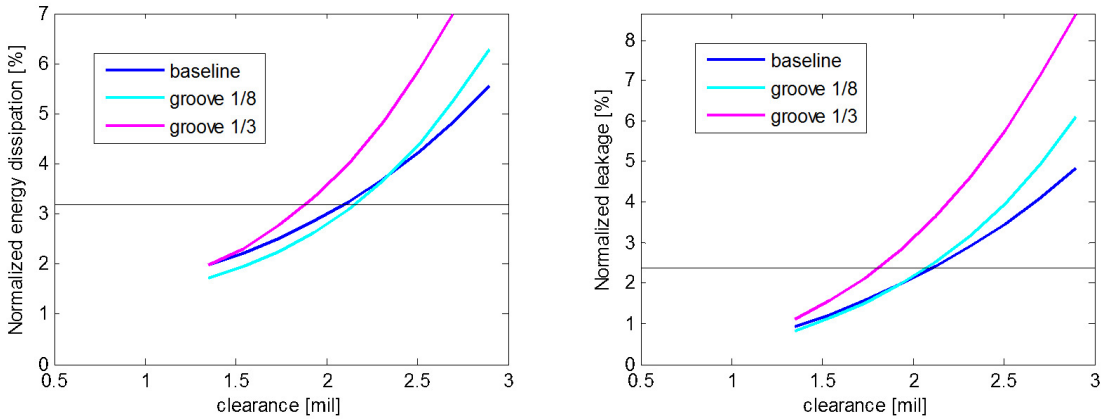

Fig. 6.27. Grooved piston/cylinder interface performance comparing to the baseline design for the small size with different clearance at OC #2.

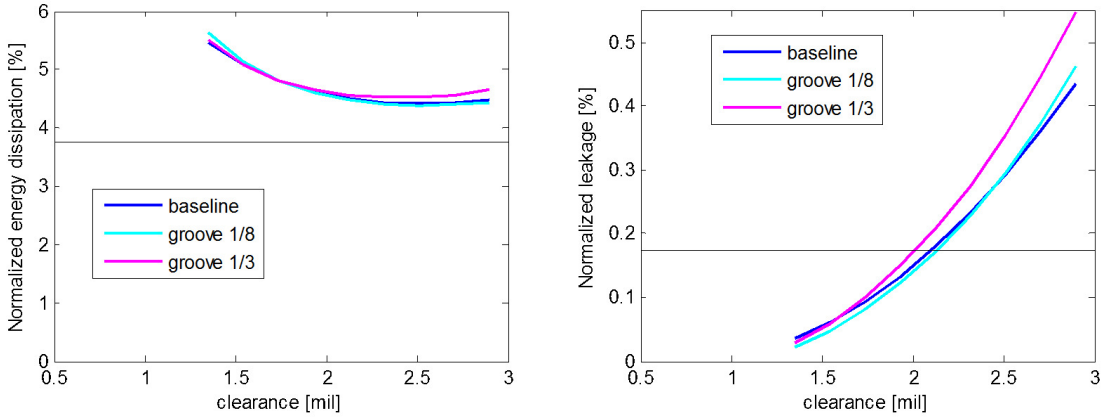

Fig. 6.28. Grooved piston/cylinder interface performance comparing to the baseline design for the small size with different clearance at OC #3.

and the two piston/cylinder interfaces that have a groove on the cylinder bore running surface. In general, the groove 1/3 design has more leakage and energy dissipation than the baseline for the same clearance. However; the curves of groove 1/8 design crossing the reference line at almost the same clearance as the baseline at OC #1, OC #2 and OC #3. At OC #1 which has the maximum power and the OC #4, the groove 1/8 design is able to bring the normalized energy dissipation of the down-scaled

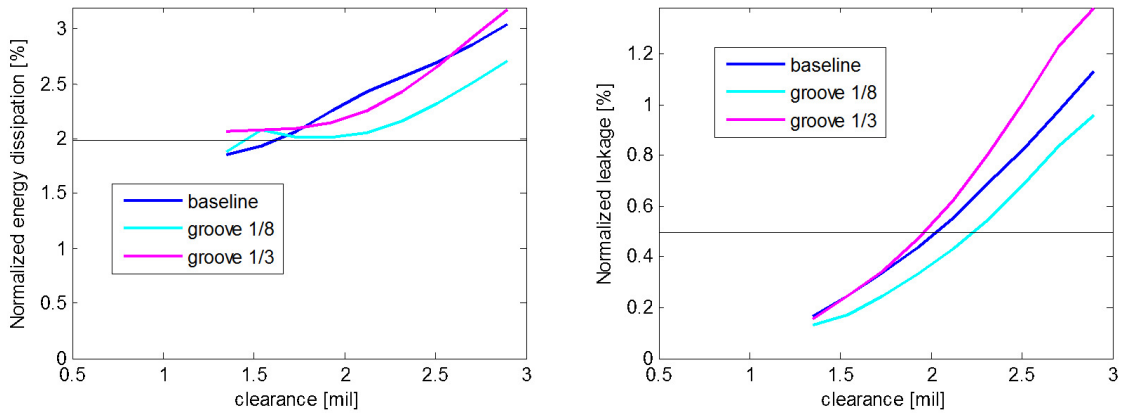

Fig. 6.29. Grooved piston/cylinder interface performance comparing to the baseline design for the small size with different clearance at OC #4.

piston/cylinder interface to the level of the original size. The energy dissipation of groove 1/8 is almost the same as the baseline at OC #2 and OC #3.

6.6 Conclusion

Both clearance and piston guide length have been found having significant impacts on the energy dissipation and leakage of the piston/cylinder interface.

The material used in piston/cylinder interface also has a notable influence on the energy dissipation and leakage.

The bi-material piston design is able to reduce the energy dissipation of the piston/cylinder interface, especially at high and low operating temperatures. This is because that the thermal expansion of the bi-material piston reduces the gap height when leakage dominates the total power loss and increases the gap height when friction dominates the power loss.

A general clearance scaling method has been found as shown in Eq. 6.5 that brings the normalized leakage flow rate of the scaled interface very close to the original size, and bring normalized energy dissipation of the up-scaled interface close to or less than the original size.

The groove profile on the cylinder bore surface located one-eighth of the piston guide length from the displacement chamber end is able to bring the normalized energy dissipation of the down-scaled piston/cylinder interface to the value of the original size at maximum and minimum power operating conditions.

7. A PATH TOWARD AN EFFECTIVE CYLINDER BLOCK/VALVE PLATE INTERFACE SCALING

In this chapter, the scaling characteristics and the methodology of the cylinder block/valve plate interface in swashplate type axial piston machines are studied in more detail. The design parameters which define the fluid film geometry and control the structural stiffness are investigated for three different sizes (9.375 cc, 75 cc, and 600 cc) at multiple operating conditions. A nonlinear scaling method for cylinder block/valve plate interface is proposed which show much better effectiveness than the linear scaling law.

7.1 Fluid film in cylinder block/valve plate interface

Fig. 7.2 presents an exaggerated fluid film in the lubricating gap between the cylinder block and the valve plate. The fluid film in the gap is defined by the width of the sealing land formed at the cylinder block bottom surface or the valve plate top (running) surface. In this chapter, the width of the sealing land of the cylinder block/valve plate interface is always designed to be controlled by the cylinder block running surface.

Fig. 7.2 shows a geometry of the lubricating gap area controlled by the geometry of the bottom surface of the cylinder block, more specifically, the width of the sealing land edge b1, b2, and the width of the kidney shape opening c which are also shown in the figure.

Besides the dimensions of the running surface, the fluid film behavior in the cylinder block/valve plate interface is also significantly influenced by the elastic deformation of the solid bodies. Therefore, even with the same running surface dimensions, different solid body geometry, such as the structure of the inlet and outlet port in

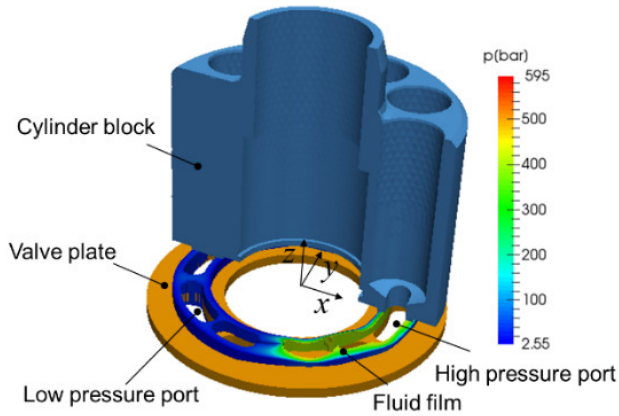

Fig. 7.1. Fluid film in cylinder block/valve plate interface.

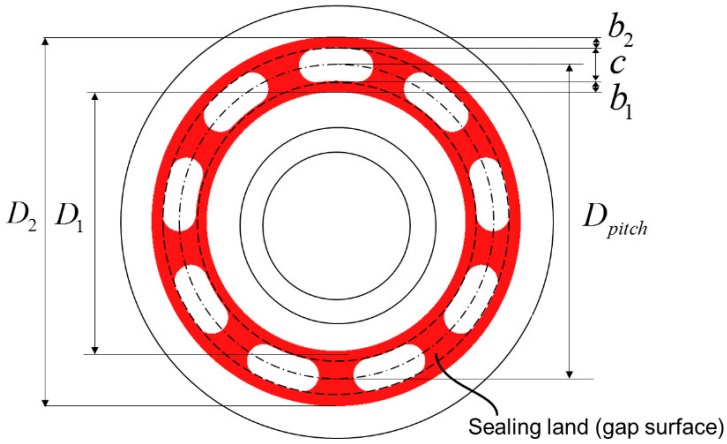

Fig. 7.2. Cylinder block gap dimensions.

the end case, will result in a different lubricating interface surface deflection, hence a different sealing and bearing performance.

The analytical analysis presented in chapter 5 proved the proportionally scaled cylinder block/valve plate interface could not achieve the same energy efficiency as the pre-scaled interface by the nature of the fundamental physics. Therefore, in order to scale the cylinder block/valve plate interface more effectively, some of the design parameters have to be scaled nonlinearly. A study of the relationship between the

design parameters and the cylinder block/valve plate interface performance is the essential first step toward the aiming effective scaling approach.

7.2 Cylinder block/valve plate interface design parameters

The width of the sealing land edge b_1 and b_2 of the running surface on the bottom of the cylinder block as shown in Fig. 7.2 controls the sealing function of the cylinder block/valve plate interface as well as the pressure distribution in the fluid film due to both hydrodynamic effect and hydrostatic effect. The width of the outer and inner sealing land edge can be either the same or different. In this study, a nominal design has been selected which has the same inner and outer sealing land edge width: $b = b_1 = b_2$. The width of the sealing land edge b as shown in Fig. 7.3 is the first design parameter to be investigated. The range of the width of the sealing land edge has been studied from -35% to 70% of the nominal value.

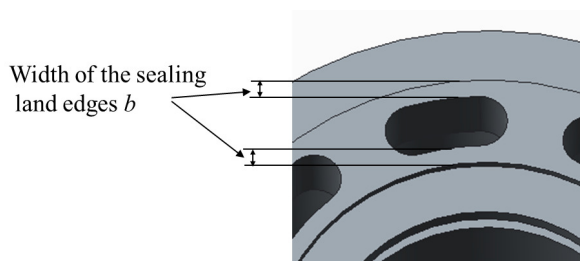

Fig. 7.3. Width of the sealing land edges b.

Table 7.2 lists four selected operating conditions to study the influence of the width of the sealing land edge on the cylinder block/valve plate interface sealing and bearing functions. The OC #1 is the maximum power operating condition of the selected unit, which results in also the maximum power loss. The OC #2 is low speed and maximum pressure operating condition, examining the sealing function of the cylinder block/valve plate interface. The OC #3 is low pressure and maximum speed operating condition, emphasizing the friction loss of the interface. Finally, the OC #4 is low pressure and low speed operating condition.

Table 7.1.
Summary of unit sizes and operating conditions.

operating conditions	pressure	speed	displacement
OC #1	max	max	full
OC #2	max	28% of max	full
OC #3	12.5% of max	max	full
OC #4	12.5% of max	28% of max	full

The viscous energy dissipation in the lubricating gap directly contributes to the power loss of the cylinder block/valve plate interface. The viscous shear is generated from the pressure difference across the gap area as well as the relative sliding motion between the cylinder block and valve plate. Besides the energy efficiency, another essential aspect of the cylinder block/valve plate interface performance is the load carrying capability. As described in chapte 2, as a free body, the cylinder block subjects to external forces and moments from the displacement chamber pressure forces and its reaction forces. These external loads must be balanced by the fluid pressure distribution in the cylinder block/valve plate lubricating gap. This pressure distribution is dependent on the operating conditions, the fluid properties, the surface deformations, the cylinder block position, and the micro motions. A detailed fluid-structure and thermal interaction model is used to study the energy efficiency and the load carrying capacity of the cylinder block/valve plate interface considering the complicated physics and their interactions, In the simulation, the pressure distribution in the lubricating gap is obtained from solving the Reynolds equation numerically in discretized finite volume fluid grid.

A contact algorithm is used to prevent the top surface to the lubricating gap from penetration into the bottom surface during the numerical micro motion calculation. The algorithm add an additional acceleration on the cylinder block to help it to stay on top of the valve plate when the fluid film thickness is approaching a critical level,

normally the level of the running surface roughness. Fig. 7.4 shows an example of a fluid film between the cylinder block and the valve plate that has a small area where the film thickness is approaching the critical level. This additional acceleration is multiplied by the weight of the cylinder block and presented as an unbalanced load in the following simulation results. The high unbalanced load is the indication of the insufficient load carrying capacity and unstable fluid film behavior.

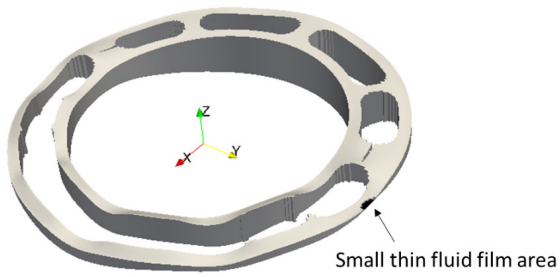

Fig. 7.4. Small thin fluid film area comparing to the whole fluid domain in cylinder block/valve plate interface.

In Fig. 7.5 and Fig. 7.6, the blue curves show the normalized energy dissipation for the cylinder block designs with different sealing land edge widths at the four operating conditions as Table 7.2. Similarly, the green curve shows the unsupported load for these different cylinder block/valve plate interface designs. At all of operating conditions, the normalized unsupported load has a negative correlation with the width of the sealing land edge. At operating conditions #1 and #2, the normalized energy dissipation increases with the width of the sealing land edge. There is no obvious changes in normalized energy dissipation at operating condition #3. At operating condition #4, the normalized energy dissipation slightly increases with the width of the sealing land edge.

Besides the running surface dimensions, the structure of the solid bodies is also investigated. As shown in figure 8.7, the investigated solid bodies structure includes the thickness of the material between valve plate surface and the port cavity d, and the length of the canal channel l are also investigated.

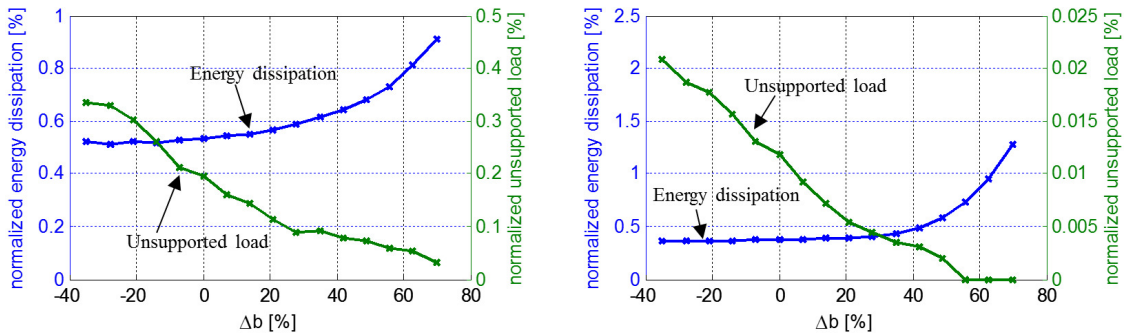

Fig. 7.5. Width of the sealing land impact on interface performance at OC #1 and #2.

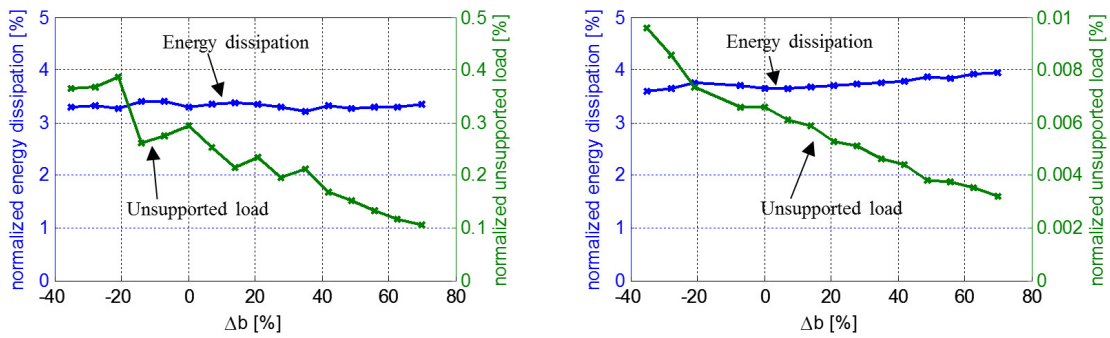

Fig. 7.6. Width of the sealing land impact on interface performance at OC #3 and #4.

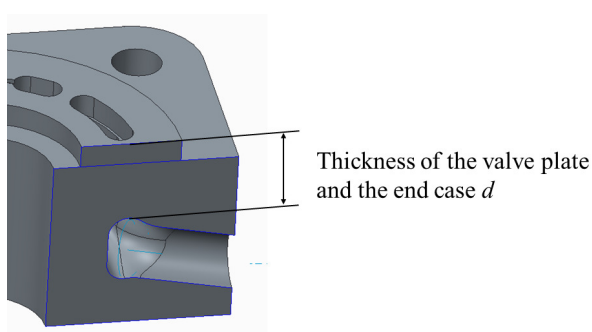

Fig. 7.7. Thickness of the valve plate and the end case d.

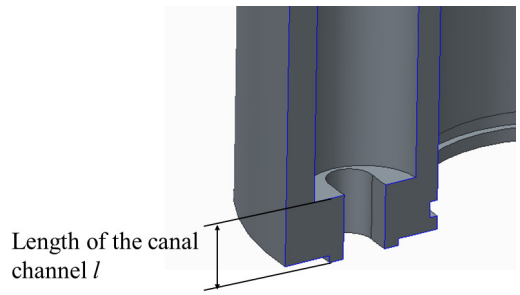

Fig. 7.8. Length of the cylinder block canal channel l.

The thickness of the material between the surface of the valve plate and the cavity of the ports determines the stiffness of the valve plate/end case assembly. Less material causes more deformation on the running surface due to the gap and port pressure. In the investigation, the thickness d as shown in Fig. 7.7 varies from 69% less than the original design to 38% more. Fig. 7.9 and Fig. 7.10 show the normalized energy dissipation and normalized unsupported load change with the thickness d at four operating conditions. In Fig. 7.9, the normalized energy dissipation and normalized unsupported load for both of the operating conditions #1 and #2 show a negative correlation with the thickness d. For operating condition #3 in Fig. 7.10, the normalized unsupported load decreases with increasing thickness d. The normalized energy dissipation is higher for the valve plate and end case assembly design that has more supporting material. The operating condition #4 in Fig. 7.10 shows opposite trends comparing to OC #3. But as shown in the figure, the unsupported load at OC #4 is very small.

The length of the canal channel determines the stiffness of the cylinder block running surface. Shorter canal channel results in less material that support the cylinder block running surface from deforming under the gap and the displacement chamber pressure. In the investigation, the length l as shown in Fig. 7.8 varies from the original value to 70% less than the original value. Fig. 7.11 and Fig. 7.12 show the normalized energy dissipation and normalized unsupported load with the variation on canal channel length. As shown in the figures, the investigation indicates that the length of

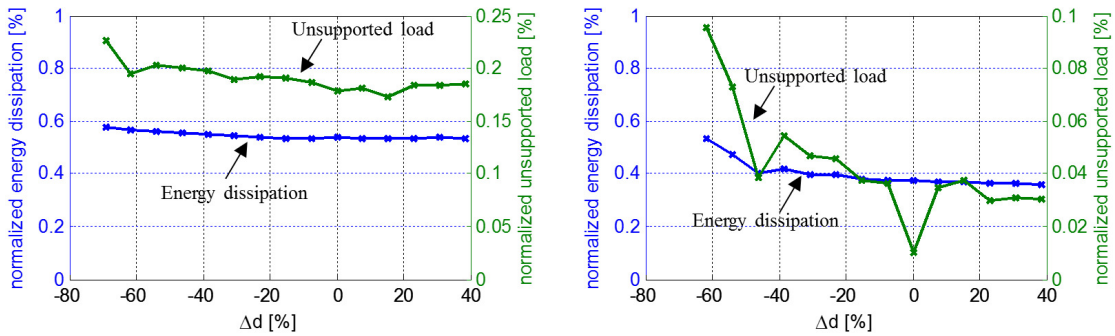

Fig. 7.9. Thickness of the valve plate and end case assembly impact on interface performance at OC #1 and #2.

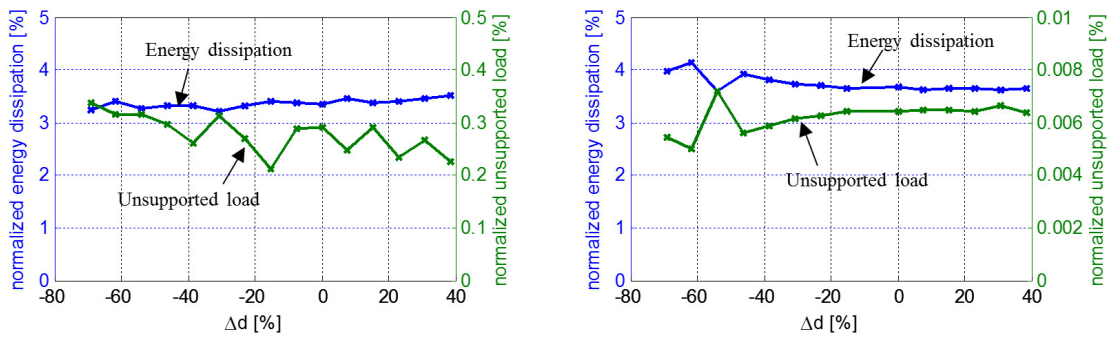

Fig. 7.10. Thickness of the valve plate and end case assembly impact on interface performance at OC #3 and #4.

the canal channel has no obvious impact on both the energy efficiency and the load carrying capacity.

In this section, an investigation of the influence of the design parameters on the cylinder block/valve plate interface performance is presented. Along the three selected parameters, in term of the width of the sealing land edge b, the thickness of the valve plate and end case assembly d, and the cylinder block canal channel length l, the width of the sealing land has the most significant impact on the energy efficiency and the load carrying capacity of the cylinder block/valve plate interface. The cylinder block/valve plate interface with thicker valve plate and end case assembly generate

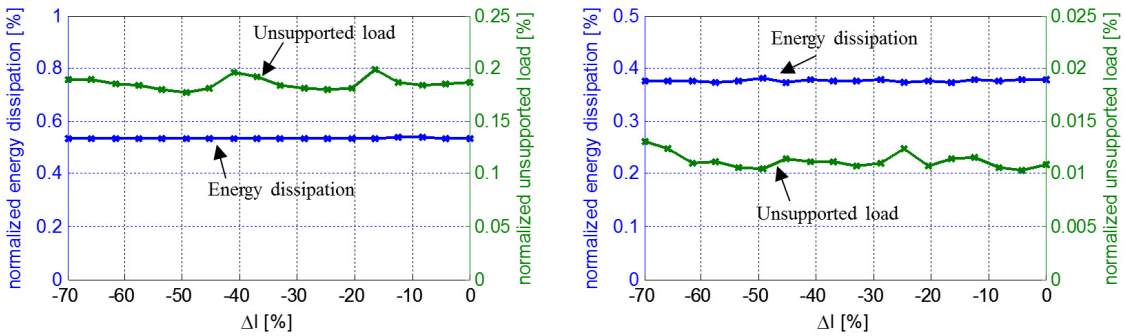

Fig. 7.11. Length of the canal channel impact on interface performance at OC #1 and #2.

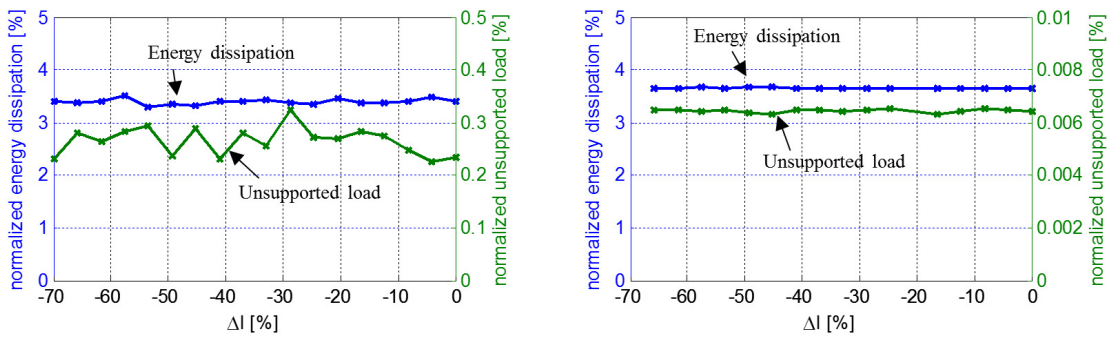

Fig. 7.12. Length of the canal channel impact on interface performance at OC #3 and #4.

a lower energy dissipation and capable to support a higher load. However, a thicker design will results in a larger machine, therefore, not ideal when the compactness of the machine is emphasized. The investigation shows that the canal channel length has a limited impact on the cylinder block/valve plate interface performance.

7.3 The width of the sealing land for different sizes

According to the investigation from the previous section, the width of the sealing land has been further investigated for different sizes. The nominal cylinder

block/valve plate interface has been linearly scaled into two different sizes. The bigger one was scaled according to the linear scaling factor $\lambda = 2$, and the smaller one was scaled down to $\lambda = 0.5$. Together with the original size, three sizes have been studied. The operating conditions under investigation are the OC #1 OC #4 shown in Table 7.2. Note that the maximum rotational speed scales with the reciprocal of the linear scaling factor λ. Therefore, for different sizes, the absolute operating speeds of the comparable operating conditions are different. Fig. 7.13 to Fig. 7.16 show the simulation results for the normalized power loss, the normalized leakage, and the normalized unsupported load change with the sealing land edge width for different sizes at four different operating conditions.

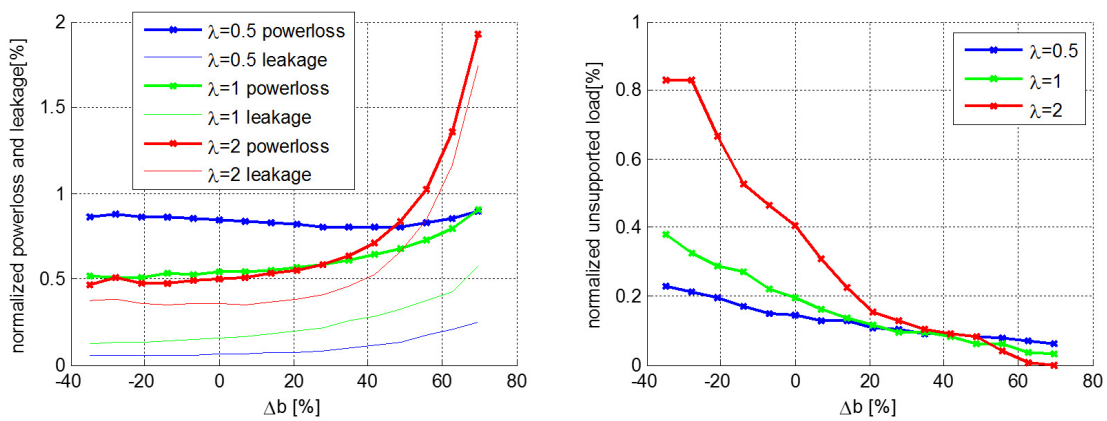

Fig. 7.13. The normalized power loss, the normalized leakage, and the normalized unsupported load change with the sealing land edge width for different sizes at OC #1.

The findings in the investigation of the width of the sealing land influence on the cylinder block/valve plate interface performance can be summarized as:

- The up-scaled cylinder block/valve plate interface has less normalized energy dissipation than the original size where the width of the sealing land changes less than positive 40%, however, the down-scaled cylinder block/valve plate interface always generates more normalized energy dissipation than the original size within the range of the width of the sealing land that is studied.

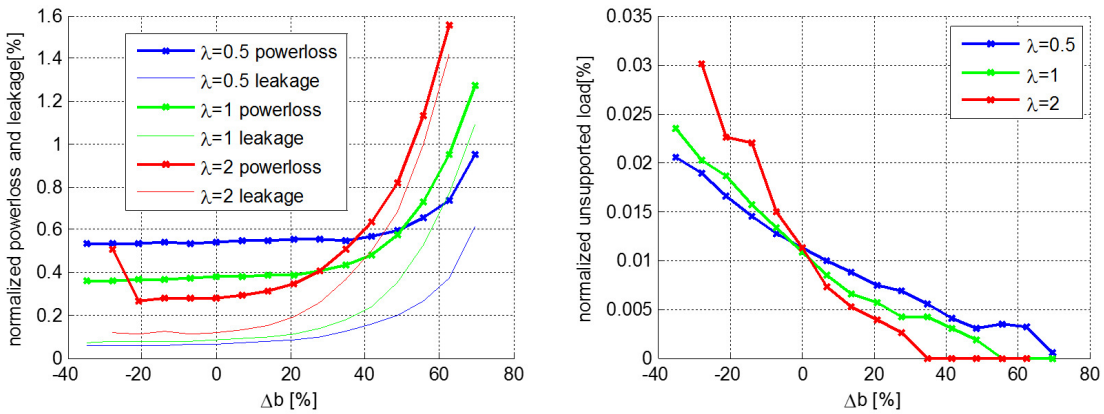

Fig. 7.14. The normalized power loss, the normalized leakage, and the normalized unsupported load change with the sealing land edge width for different sizes at OC #2.

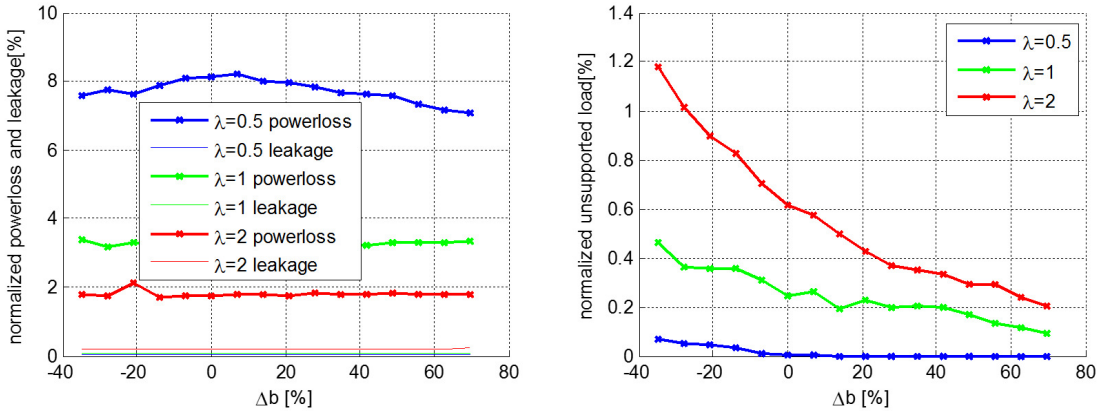

Fig. 7.15. The normalized power loss, the normalized leakage, and the normalized unsupported load change with the sealing land edge width for different sizes at OC #3.

- The normalized unsupported load decreases with the width of the sealing land for all three unit sizes and all operating conditions. At high speed (OC #1 and OC #3), the up-scaled cylinder block/valve plate interface shows higher normalized unsupported load when scaled linearly without design modification

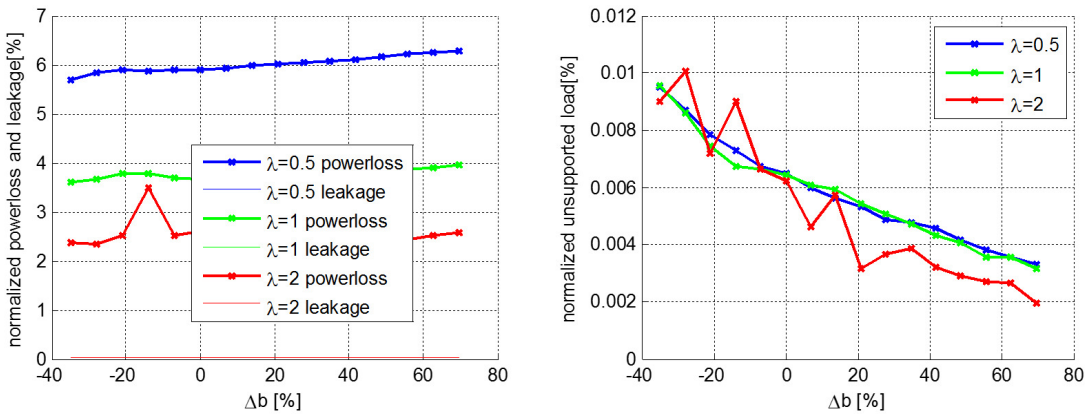

Fig. 7.16. The normalized power loss, the normalized leakage, and the normalized unsupported load change with the sealing land edge width for different sizes at OC #4.

($\Delta b = 0\%$). In order to achieve the same load carrying ability as the original size has, the width of the sealing land needs to be increased accordingly.

- The difference between the energy dissipation and the leakage loss is the friction torque loss. As concluded at the end of chapter 5, these figures confirmed that the larger interface has lower friction torque loss and higher volumetric loss. The smaller interface has higher friction torque loss and lower volumetric loss.

7.4 A nonlinear scaling approach

Both the analytical analysis results in chapter 5 and the numerical simulation results in the previous section reflected that the down-scaled cylinder block/valve plate interface generates higher friction loss and the up-scaled cylinder block/valve plate interface has low volumetric efficiency and lower load carrying capability. A nonlinear scaling study is conducted focusing on the volumetric efficiency and the load carrying capability of the up-scaled cylinder block/valve plate interface and the energy dissipation of the down-scaled cylinder block/valve plate interface.

In order to reduce the normalized leakage flow rate of the up-scaled cylinder block/valve plate interface, the width of the sealing land edges shown in Fig. 7.2 has to be further increased from the linearly scaled value. This enlarged sealing land area improves the sealing function of the cylinder block/valve plate interface, but, overly balances the external load on the cylinder block. The overly balanced cylinder block lifts away from the valve plate, results in higher gap height and higher leakage. That is why the normalized leakage curve for the up-scaled cylinder block/valve plate interface $\lambda = 2$ shown in Fig. 7.13 descends slightly but climbs back up very quickly after the width of the sealing land edge been increased too much.

The geometry of the running surface on the cylinder block bottom is controlled by the width of the sealing land edge b, and the width of the kidney shape opening c (see Fig. 7.2). A series of simulation studies are conducted to investigate not only the width of the sealing land b, but also the width of the kidney shape opening c. Instead of scaled linearly, in this study, the width of the kidney shape opening is scaled nonlinearly as shown in Fig. 7.17.

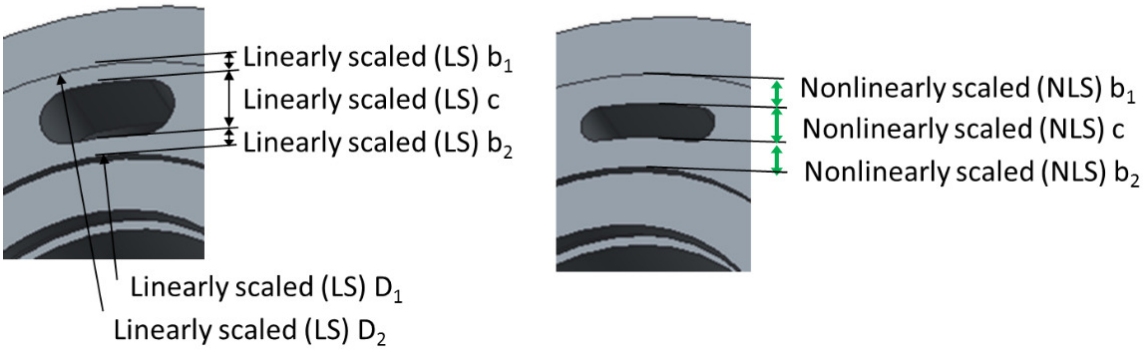

Fig. 7.17. An example of a nonlinearly scaled cylinder block running surface.

Fig. 7.18 to Fig. 7.21 show the simulation results of the nonlinearly up-scaled ($\lambda = 2$) cylinder block/valve plate interface together with the nominal design at original size (the black horizontal line). The simulation results in red color represent the cylinder block that has linearly scaled kidney shape opening, the simulation results in cyan color represent the cylinder block that has nonlinearly scaled kidney shape

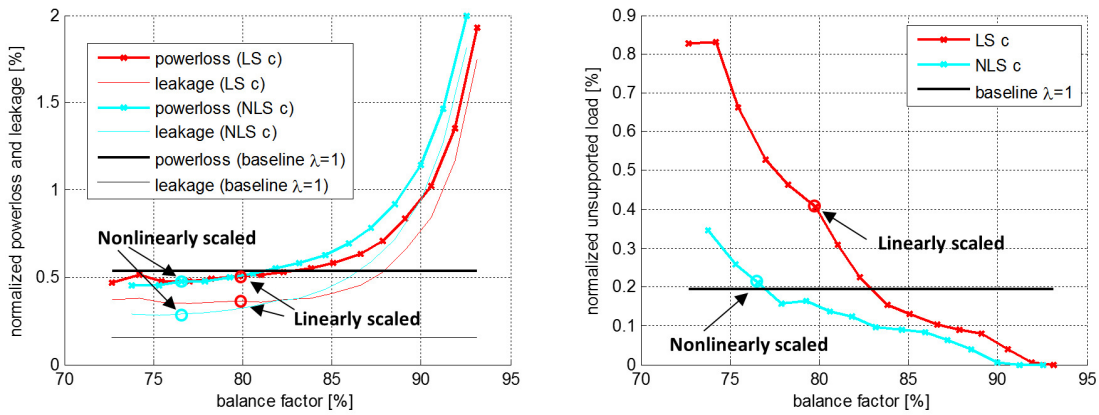

Fig. 7.18. Simulated performances of nonlinearly up-scaled cylinder block/valve plate interface OC #1.

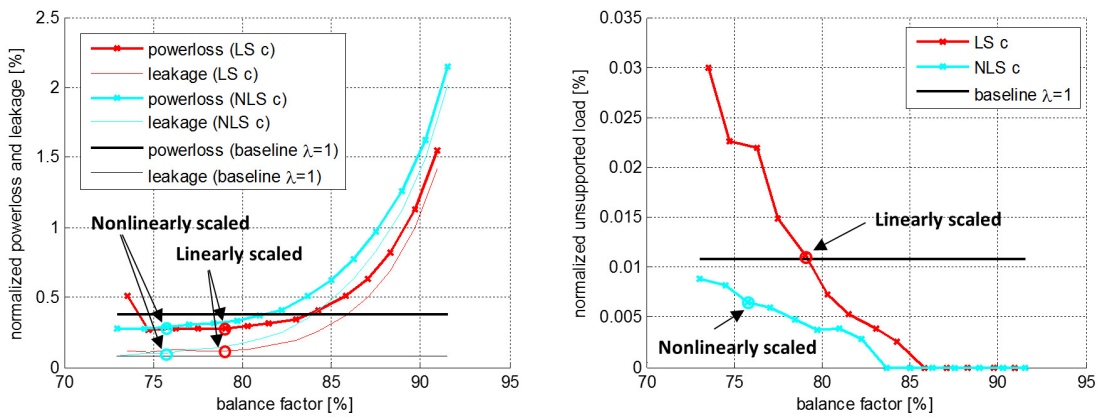

Fig. 7.19. Simulated performances of nonlinearly up-scaled cylinder block/valve plate interface OC #2.

opening. In this case, the width of the nonlinearly scaled kidney shape opening follows:

$$c = \lambda^{0.25} \cdot c_0 \tag{7.1}$$

The width of the sealing land edge b varies in Fig. 7.18 to Fig. 7.21, results in different balance factors. For each design, a balance factor can be calculated from the hydrostatic fluid force divided by the external force. The balance factor should

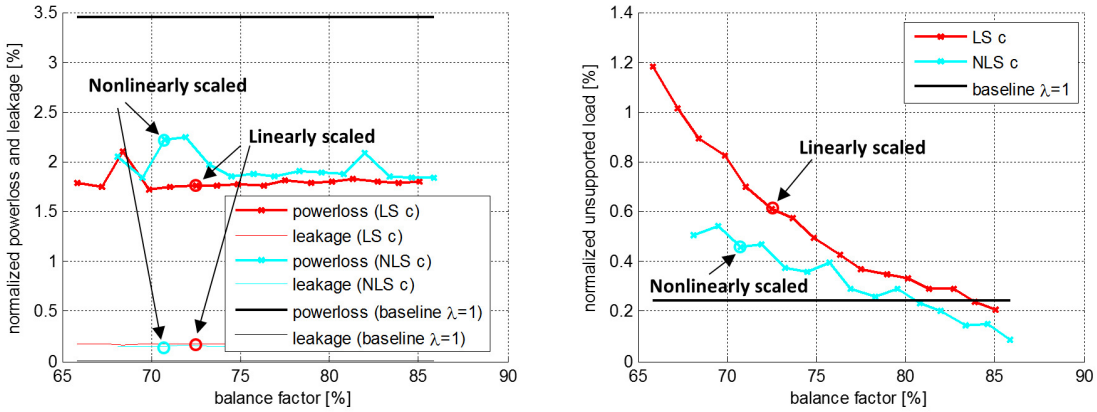

Fig. 7.20. Simulated performances of nonlinearly up-scaled cylinder block/valve plate interface OC #3.

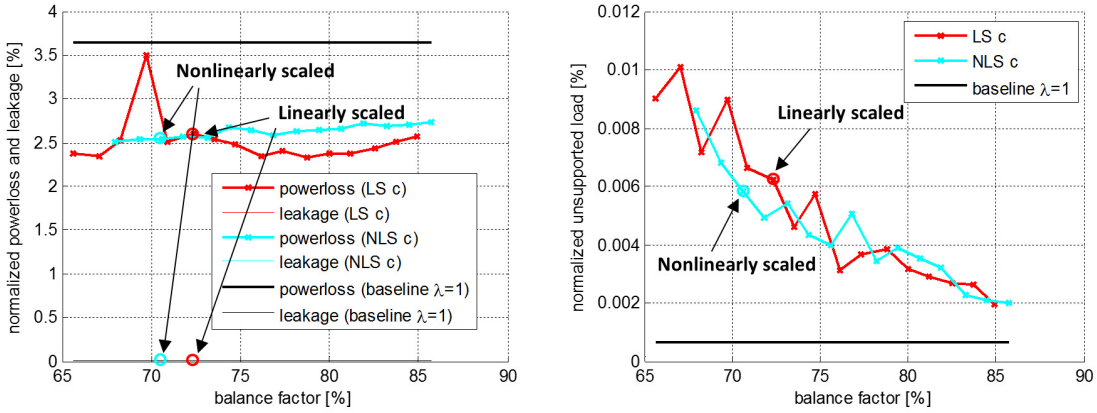

Fig. 7.21. Simulated performances of nonlinearly up-scaled cylinder block/valve plate interface OC #4.

be less than 100% and the rest of the external load is balanced by the hydrodynamic pressure forc

In Fig 7.18 to Fig 7.21, the red circles indicate the performance of the cylinder block/valve plate interface linearly up-scaled from the original size. The cyan circles indicate the performance of an example of the cylinder block/valve plate interface nonlinearly up-scaled from the original size. In this example, the width of the kidney

shape opening is scaled according to Eq. 7.1, and the width of the sealing land edge is scaled according to:

$$\begin{aligned} b_1 &= \lambda^{1.5} \cdot b_{1\_0} \\ b_2 &= \lambda^{1.5} \cdot b_{2\_0} \end{aligned} \tag{7.2}$$

Comparing to the linearly up-scaled cylinder block/valve plate interface, the example of the nonlinearly scaled interface reduces the normalized leakage at OC #1, bring the volumetric efficiency of the up-scaled interface closer to what the original size has. More importantly, by up-scaling the interface according to Eq. 7.1 and Eq. 7.2, the load carrying capability is maintained at the same level as the original size at OC #1, improved at OC #2, and closer to the original size comparing to the linearly scaled counterpart at OC #3.

Similar studies are also conducted for the down-scaled cylinder block/valve plate interface. The linearly down-scaled cylinder block/valve plate interface generates higher normalized energy dissipation and lower normalized leakage than the original size. According to the findings in the sensitivity study in chapter 4, the combination of high energy dissipation and low leakage faces the danger of high port and case temperature. The axial piston machine that generates high energy dissipation and low leakage subjects to many disadvantages such as more thermal deflection, or even piston seizing. Fig. 7.22 to Fig. 7.25 show the simulation results of the nonlinearly down-scaled ($\lambda = 0.5$) cylinder block/valve plate interface together with the target nominal design at original size (the black horizontal line). The simulation results in blue color represent the cylinder block with linearly scaled kidney shape openings, the simulation results in cyan color represent the cylinder block with nonlinearly scaled kidney shape openings. In this case, the width of the nonlinearly scaled kidney shape opening follows:

$$c = \lambda^{0.7} \cdot c_0 \tag{7.3}$$

The width of the sealing land edge b varies in Fig. 7.22 to Fig. 7.25, results in different balance factor. In these figures, the blue circles indicate the performance of the

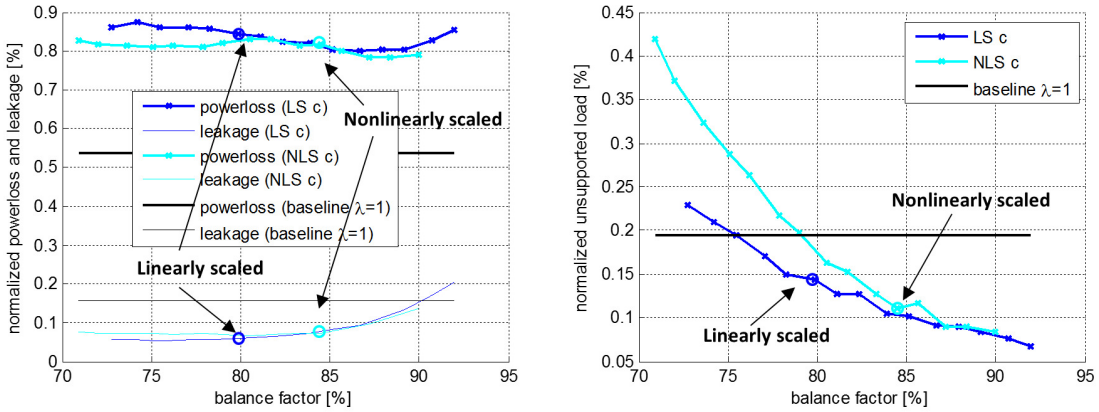

Fig. 7.22. Simulated performances of nonlinearly down-scaled cylinder block/valve plate interface OC #1.

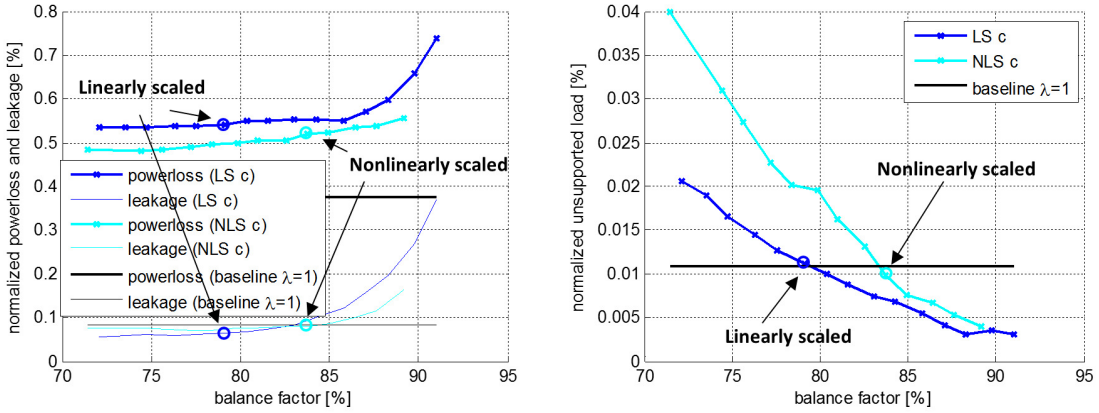

Fig. 7.23. Simulated performances of nonlinearly down-scaled cylinder block/valve plate interface OC #2.

cylinder block/valve plate interface linearly down-scaled from the original size. The cyan circles indicate the performance of an example of the cylinder block/valve plate interface nonlinearly down-scaled from the original size. In this example, the width of

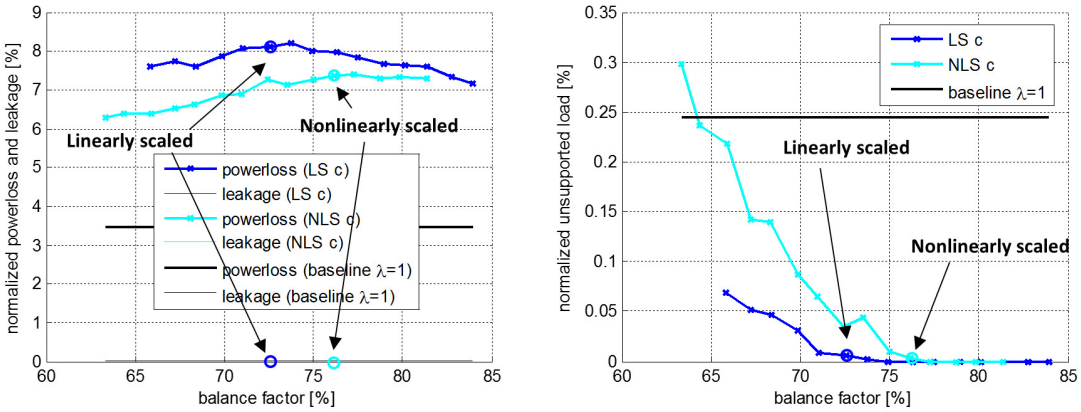

Fig. 7.24. Simulated performances of nonlinearly down-scaled cylinder block/valve plate interface OC #3.

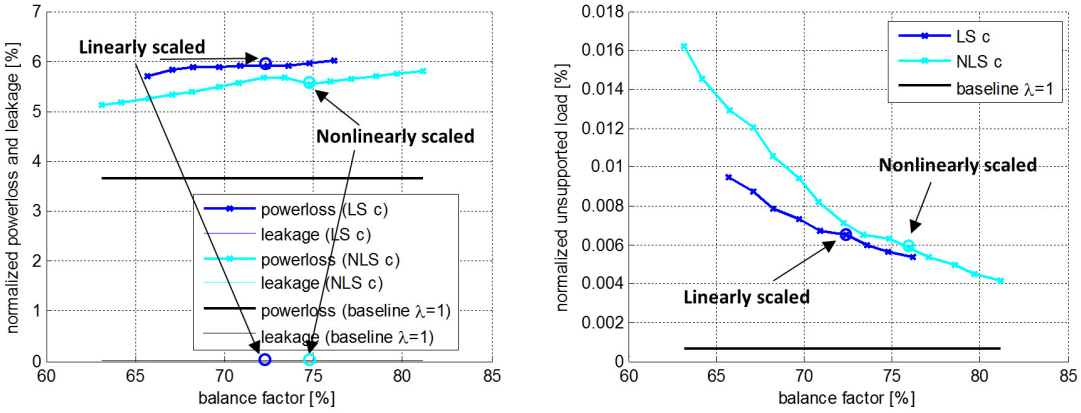

Fig. 7.25. Simulated performances of nonlinearly down-scaled cylinder block/valve plate interface OC #4.

the kidney shape opening is scaled according to Eq. 7.3, and the width of the sealing land edge is scaled according to:

$$\begin{aligned} b_1 &= \lambda^{1.4} \cdot b_{1\_0} \\ b_2 &= \lambda^{1.4} \cdot b_{2\_0} \end{aligned} \tag{7.4}$$

Comparing this example of the nonlinearly down-scaled cylinder block/valve plate interface to its linearly scaled counterpart, the nonlinearly scaled one have always

better load carrying capability. At all the operating conditions, the normalized energy dissipation of the nonlinearly scaled cylinder block/valve plate interface is lower than the linearly scaled one. At operating conditions #1 and #2, the nonlinearly scaled interface also has the normalized leakage flow rate closer to the value of the reference.

7.5 Conclusion

The findings in this chapter can be summarized as:

- Both the width of the sealing land b and the thickness of the valve plate and end case assembly d have significant impact on the performance of the cylinder block/valve plate interface.
- Linearly scaled cylinder block/valve plate interface is not able to achieve the energy efficiency and load carrying capacity as the pre-scaled interface.
- The proposed nonlinear scaling method is able to bring the performance and the efficiency of the scaled interface closer to the original size.

8. A PATH TOWARD AN EFFECTIVE SLIPPER/SWASHPLATE INTERFACE SCALING

In this chapter, the slipper/swashplate interface is studied for different sizes (9.375 cc, 75 cc, and 600 cc) at multiple operating conditions. The case study findings show that, the balance factor, which defined as the ratio between the hydrostatic pressure force and the external load, need to be varied by nonlinearly scale the inner diameter of the sealing land to compensate the non-scalable viscous friction.

8.1 slipper/swashplate interface balance factor

The thin fluid film between the slipper and the swashplate supports the slipper under the external load from the pressure in the displacement chamber. The slipper/swashplate interface behaves close to a hydrostatic bearing, which relies mostly on the hydrostatic pressure to bear the load. The homeostatic pressure force of the slipper/swashplate interface can be calculated as:

$$F_{st} = \frac{1}{8} \cdot p_G \cdot \pi \cdot \frac{d_{outG}^2 - d_{inG}^2}{ln(d_{outG}) - ln(d_{inG})} \tag{8.1}$$

where p_G is the pressure in the slipper pocket and d_{outG} and d_{inG} are the diameters of the outer and inner edge of the slipper sealing land as shown in Fig. 8.1.

The balance factor then determines how much the hydrostatic pressure force contribute to balance the external load:

$$C_{balance} = \frac{F_{st}}{F_{load}} \tag{8.2}$$

According to the findings in chapter 5, slipper swashplate interface does not suffer from the non-scalable thermal behavior significantly (see Fig. 5.10). Therefore, the scaling study of the slipper/swashplate interface focuses on the non-scalable viscous friction and leakage.

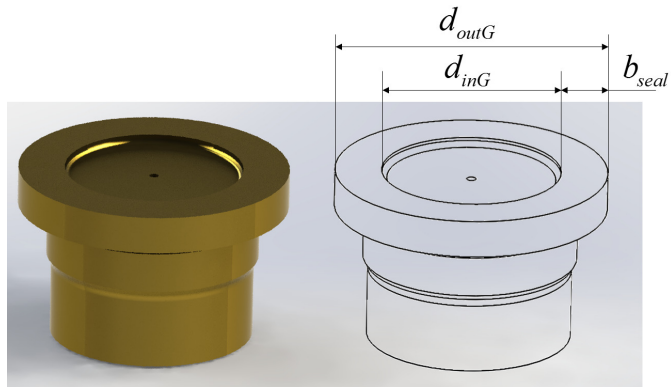

Fig. 8.1. Design parameters of the slipper/swashplate interface.

8.2 The width of the slipper sealing land

As shown Fig. 8.1, the width of the slipper sealing land b_{seal} is the difference between the radius of the outer and inner edge of the sealing land. According to Eq. 8.1 and Eq. 8.2, one can change the width of the sealing land b_{seal} while keeping the balance factor of the slipper/swashplate interface. Different slipper sealing land widths are studied for different sizes at multiple operating conditions as listed in Table. 8.2. The width of the sealing land is changed by varying the inner and outer sealing land diameter d_{inG} and d_{outG} while keeping the balance factor $C_{balance}$.

Table 8.1.
Summary of unit sizes and operating conditions.

operating conditions	pressure	speed	displacement
OC #1	max	max	full
OC #2	max	28% of max	full
OC #3	12.5% of max	max	full
OC #4	12.5% of max	28% of max	full

Fig. 8.2 to Fig. 8.5 show the normalized leakage and normalized power loss from a single slipper/swashplate interface with different slipper sealing land width for three

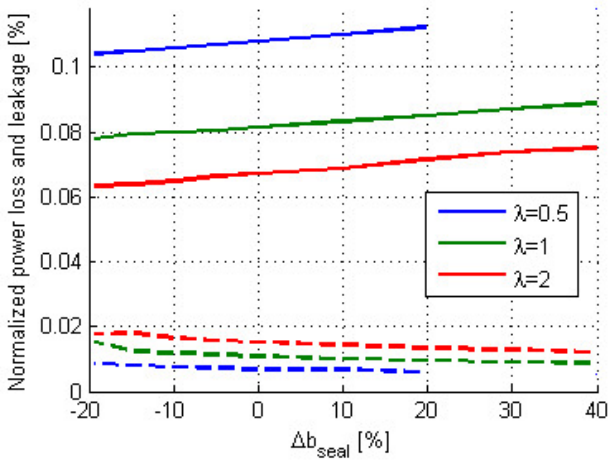

Fig. 8.2. Normalized power loss and leakage change with the width of the slipper sealing land at OC #1.

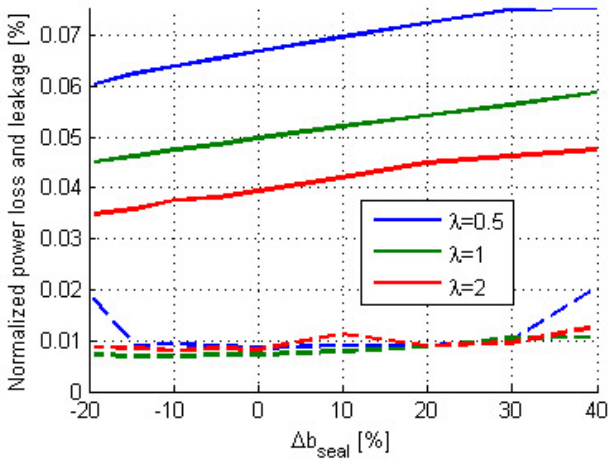

Fig. 8.3. Normalized power loss and leakage change with the width of the slipper sealing land at OC #2.

different sizes at each operating condition. The normalized leakage uses the theoretical outlet flow rate as the reference; the normalized power loss uses the theoretical output power as the reference. Therefore, even for different sizes, the normalized power loss and leakage are comparable.

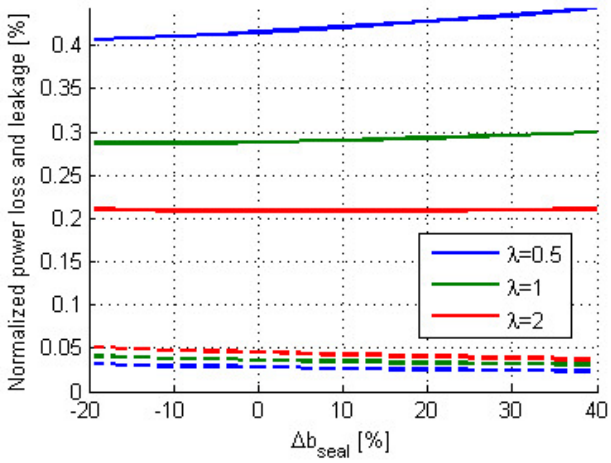

Fig. 8.4. Normalized power loss and leakage change with the width of the slipper sealing land at OC #3.

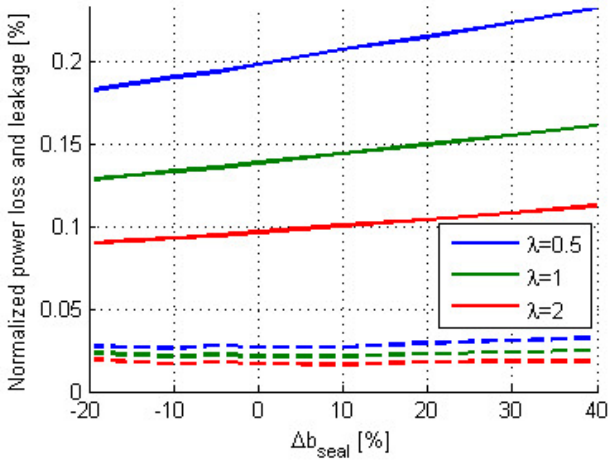

Fig. 8.5. Normalized power loss and leakage change with the width of the slipper sealing land at OC #4.

As it can be observed from Fig. 8.2 to Fig. 8.5, the leakage of slipper/swashplate interface is much lower than the power loss. Therefore, the study of the scaling performance of the slipper/swashplate interface emphasis the energy efficiency.

For all four operating conditions, the power losses of all three different size slipper/swashplate interfaces have positive correlations with the width of the slipper

sealing land. This is because the viscous friction loss dominates the power loss in the slipper/swashplate interface. When increasing the width of the sealing land, the sealing area is enlarged, therefore the friction becomes greater. Comparing the three different sizes, the largest one ($\lambda = 2$) shows the best energy efficiency, while the smallest one ($\lambda = 0.5$) shows the worst energy efficiency. This can be explained as the non-scalable viscosity according to the findings in chapter 5.

In order to compensate the non-scalable viscosity, according to the results in Fig. 8.2 to Fig. 8.5, one should increase the width of the slipper sealing land for the up-scaled slipper/swashplate interface and decrease the width for the down-scaled one. By doing this, the energy efficiency of the scaled slipper/swashplate interface becomes closer to the pre-scaled baseline. However, as the figure shows, the width of the sealing land has limited influence on energy efficiency. Therefore, in order to maintain the slipper/swashplate energy efficiency, more investigations are needed.

8.3 The inner diameter of the slipper sealing land

As discussed in the previous section, change on the width of the sealing land while keeping the balance factor has limited influence on the energy efficiency of the slipper/swashplate interface, therefore, is not enough to improve the effectiveness of the slipper/swashplate interface scaling.

In this section, instead of changing both the inner and outer diameter of the slipper sealing land d_{inG} and d_{outG} together to keep the balance factor $C_{balance}$, only the sealing land inner diameter is changed while leaving the balance factor changes with the dimension of the pocket.

Fig. 8.6 to Fig. 8.9 show the normalized leakage and normalized power loss of the slipper/swashplate interface with different slipper sealing land inner diameter for three different sizes at each operating condition. Note that the range of the change on the sealing land inner diameter is the same as for the results shown in Fig. 8.2 to Fig. 8.5 while the outer diameter is maintained the same.

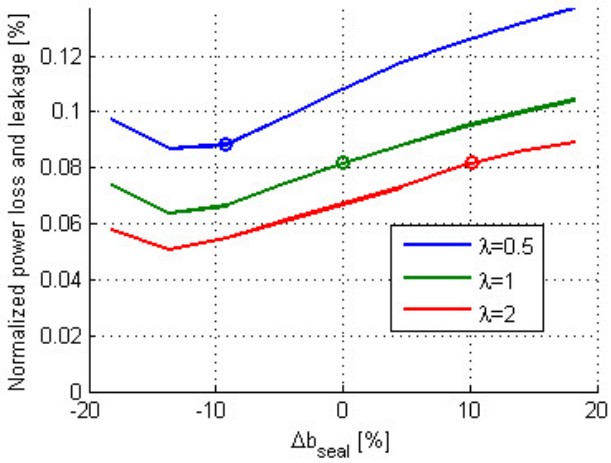

Fig. 8.6. Normalized power loss and leakage change with the slipper sealing land inner diameter at OC #1.

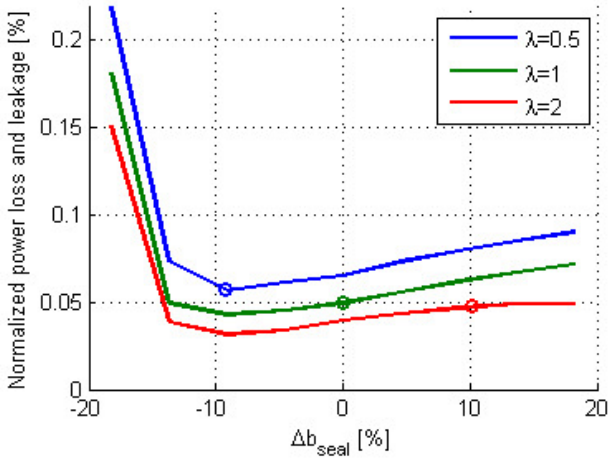

Fig. 8.7. Normalized power loss and leakage change with the slipper sealing land inner diameter at OC #2.

As shown in Fig. 8.6 to Fig. 8.9, the inclinations of the normalized power loss curves are higher than the ones in the previous chapter. That is because that the balance factor is change with the inner diameter of the sealing land, and the different hydrostatic pressure force results in different gap height between the slipper and the swashplate. This effect can be used to generate a more effective slipper/swashplate

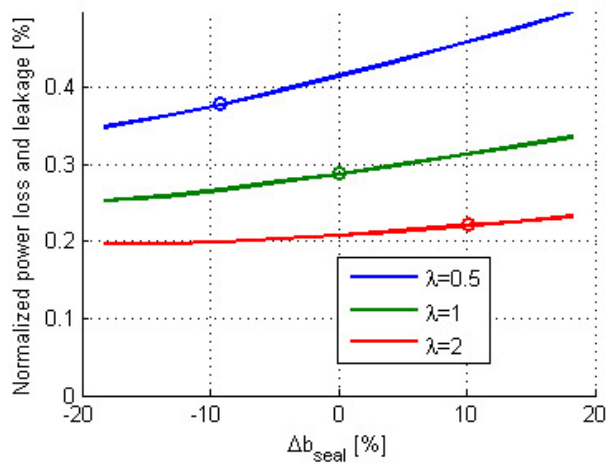

Fig. 8.8. Normalized power loss and leakage change with the slipper sealing land inner diameter at OC #3.

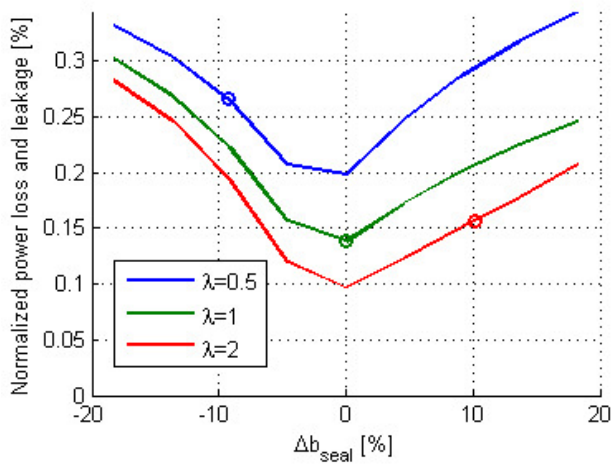

Fig. 8.9. Normalized power loss and leakage change with the slipper sealing land inner diameter at OC #4.

scaling rule. The proposed nonlinear scaling rule for the slipper/swashplate interface is:

$$\begin{aligned} d_{outG} &= \lambda \cdot d_{outG0} \\ b_{seal} &= \lambda^{1.14} \cdot b_{seal0} \end{aligned} \tag{8.3}$$

In Fig. 8.6 to Fig. 8.9, the green circle in each figure indicates the normalized power loss from the unmodified slipper/swashplate ($\Delta b_{seal} = 0$). The blue circle and the red circle in each figure indicate the normalized power loss from the nonlinearly scaled slipper/swashplate interface according to Eq. 8.3. Fig. 8.10 shows the energy efficiency difference between the linearly scaled and pre-scaled slipper/swashplate interface, and the energy efficiency difference between the nonlinearly scaled and pre-scaled one.

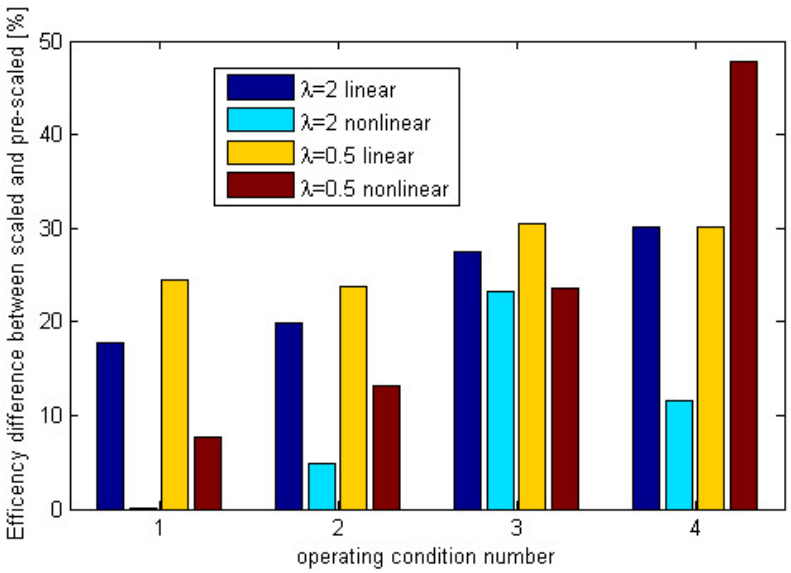

Fig. 8.10. Energy efficiency difference of linearly scaled and nonlinearly scaled slipper/swashplate interface from the baseline.

As Fig. 8.6 and Fig. 8.10 show, The nonlinear scaling rule vastly improves the scaling effectiveness from the linear scaling rule for operating condition # 1. The around 20 percents difference in energy efficiency between the up-scaled and pre-scaled slipper/swashplate interface using the linear scaling rule can be reduced to almost 0 percents by using the proposed nonlinear scaling rule. The over 20 percents difference in energy efficiency between the down-scaled and pre-scaled slipper/swashplate interface using the linear scaling rule can be reduced to less than ten percents by using the proposed nonlinear scaling rule.

The similar improvement can be found for operating condition #2, as shown in Fig. 8.7 and Fig. 8.10. The nonlinear scaling rule can reduce the scaled/pre-scaled efficiency difference from over 20 percents to 5 percents for up-scaling and 12 percents for down-scaling.

For operating condition #3, as shown in Fig. 8.8 and Fig. 8.10, the nonlinear scaling rule is able to improve the scaling effectiveness but not as significant as the previous two operating conditions. This is because, as shown in Fig. 8.8, the change on the inner diameter of the slipper sealing land has limited influence on the slipper/swashplate interface efficiency at operating condition #3.

The nonlinear scaling rule improves the scaling effectiveness for up-scaling at operating condition #4, however, worsen the scaling effectiveness for down-scaling. As Fig. 8.9 show, unlike the OC #1 and OC #3, the energy dissipation increase when reducing the width of the sealing land and increase the balance factor. The positive correlation between the energy dissipation and the balance factor indicates that the slipper is overbalanced and lift away from the swashplate. The greatly increase leakage start to determine the energy dissipation of the slipper/swashplate interface.

8.4 Conclusion

In this chapter, the scaling characteristic of the slipper/swashplate interface is investigated. Three different sizes of slipper/swashplate interface are studied at four different operating conditions as shown in Table. 8.2.

The width of the slipper sealing land b_{seal} is first studied while the balance factor $C_{balance}$ reminds the same. The simulation results show that the width of the sealing land has limited impact on the performance of the slipper/swashplate, therefore, is not enough for an effective slipper/swashplate interface scaling rule. The reason is that the slipper/swashplate interface performance is determined by the friction loss, which controlled by the gap height. The change on the width of the sealing land affects the sealing function of the slipper, but not the friction loss.

In order to compensate the non-scalable viscosity, as found in chapter 5, the gap height of the slipper/swashplate interface has to be controlled according to the size. For this reason, the balance factor must not be kept the same. The second study varies the inner diameter of slipper sealing land only, leave the balance factor changing with the size of the slipper pocket. The simulation results show that a more effective scaling rule for the slipper/swashplate interface can be found by nonlinearly scale the inner diameter of the slipper sealing land as described in Eq. 8.3.

The proposed nonlinear scaling rule for the slipper/swashplate interface is able to improve the scaling effectiveness significantly according to the simulation study as shown in Fig. 8.10.

9. CONCLUSION AND OUTLOOK

For the first time, a path toward an effective scaling approach for swashplate type axial piston machines is proposed. In this work, the scaling characteristics of the three lubricating interfaces of swashplate type axial piston machines are investigated and explained through the fundamental physics including the non-isothermal elasto-hydrodynamic effects in the fluid domain and heat transfer and thermal elastic deflection in the solid domain. Base on the obtained knowledge, a guide for effectively scale the critical lubricating interfaces is explored using a multi-domain multi-physics axial piston machine performance prediction model proposed in this work.

The major contributions along the path toward an effective scaling approach for axial piston machine can be summarized as:

- Pump and motor modeling.
- Approach for scaling analysis.
- Scaling Guidelines.

Pump and motor modeling A multi-physics multi-domain swashplate type axial piston machine performance prediction model as shown in Fig. 4.8 is proposed in this work. Thanks to its thermal boundaries prediction model described in Chapter 4, this multi-physics multi-domain model can be used to study the performance of the scaled lubricating interface without the steady-state measurements. The proposed thermal boundaries prediction model calculates the flow temperature in the outlet port volume and case volume based on the inlet flow temperature and the temperature variation due to compression, expansion, heat transfer and heat generation in the fluid domain and solid domain. The accuracy of this temperature prediction model is validated comparing to

over three hundred measured outlet and case temperature for two different fluid types, four different units, at many different speeds, operating pressures, and swashplate angles. The proposed multi-physics multi-domain model includes also a next-generation piston/cylinder lubricating interface model with vastly improved accuracy and robustness as described in Chapter 3. The pressure distribution in the fluid domain and the temperature distribution in the fluid domain and the solid domain are calculated considering more completed physics such as the squeezing effect of the elastic deformation and the compressibility of the fluid. The physics are implemented in the model using more robust and accurate numerical schemes. A elasto-hydrodynammic (EHD) pump was used to measure the temperature distribution of the cylinder bore running surface by using temperature sensors at 1620 different locations on the lubricating interface. The simulation-measurement comparison demonstrated that the proposed piston/cylinder interface model is able to predict the fluid film behavior with much high accuracy as shown in Fig. 3.26 to Fig. 3.35.

Approach for scaling analysis In order to analyze the problem of the axial piston machine scaling, an analytical study of the size-dependence of thermoelasto-hydrodynamic tribological interfaces is conducted in this work. The physical phenomena that were studied include the hydrostatic and hydrodynamic pressure distributions, the heat transfer and the heat generation in the fluid film, the heat transfer in the solid domain, and the solid body deformation due to both the pressure loading and the thermal load. The analysis indicates that the pressure distribution in the lubricating gap and the heat transfer in the fluid and in the solid bodies are the only size-dependent physical phenomena; therefore, they are the only contributors to the performance change of the lubricating interface in response to scaling. These findings allow for the creation of a general guide to scale aiming at maintaining the efficiency of the original unit. The guide suggests that different fluid, different working conditions, and different designs can be used to compensates the non-scalable pressure distri-

bution and heat transfer. The scaling guide enables pump manufacturers to apply the developed scaling laws, and efficiently generate scaled pump designs of much higher efficiency than the traditional approach of linear scaling allows for.

Scaling Guidelines With the proposed scaling guide, all three lubricating interfaces of swashplate type axial piston machine are studied for different sizes (9.375 cc, 75 cc, and 600 cc) at multiple operating conditions, and a more effective scaling rule is proposed for each interface:

- Nonlinearly scaled piston/cylinder clearance with proposed groove profile allows to maintain the volumetric efficiency of the scaled interface very close to the original size, and to keep energy efficiency of the up-scaled interface above the value for the original size.
- Nonlinearly scaled cylinder block/valve plate interface sealing land and kidney shape opening show much better effectiveness than the linear scaling law.
- Nonlinearly scaled slipper balance factor, which defined as the ratio between the hydrostatic pressure force and the external load, by nonlinearly scale the inner diameter of the sealing land, is able to compensate the non-scalable viscous friction and achieve more effective slipper/swashplate interface scaling.

This work describes a path toward the effective scaling approach for the swashplate type axial piston machine. With continued effort, the scaling process can be less monetary and temporal expensive. A highly efficient unit design can be used as a baseline to create a series of high quality pumps and motors across a wide range of unit size with minimum effort.

Beyond the scope of this work, future works on this topic include improving the fidelity of the lubricating interface fluid film behavior simulation tool by using a

finer fluid grid with possibly adaptive grid refining algorithm to further improve the accuracy of the model. The more advanced tribological effect can be considered in the lubricating interfaces model in the future, such as mixed friction and the slip boundary. More advanced technologies can be implemented in the simulation to accelerate the converging process, such as multi-core, multi-thread, and general purpose graphic processing unit (GPU) computing.

Other future works can be done on the scaling study includes more productive case study practice. A more effective scaling rule can be found using advanced optimization algorithm and the artificial intelligent technology such as neural network and machine learning.

Since as mentioned in Chapter 5, the findings of the analysis of the size-dependence of the lubricating interfaces is not limited to swashplate type axial piston machines, the scaling study for other types of lubricating interfaces in axial piston machines, radial piston machines, internal and external gear pumps and motors, gerotors, vane pumps, bearings and seals can be conducted based on this work.

Back to the swashplate type axial piston machine, the tolerance and surface roughness should also be considered in the future scaling study. The performance of the swashplate type axial piston machine other than the energy efficiency should also be investigated in the future such as noise and vibration.

REFERENCES

REFERENCES

[1] J. Ivantysyn and M. Ivantysynova, *Hydrostatic pumps and motors: principles, design, performance, modelling, analysis, control and testing.* Tech Books International, 2003.

[2] N. D. Manring, C. L. Wray, and Z. Dong, "Experimental studies on the performance of slipper bearings within axial-piston pumps," *Journal of tribology*, vol. 126, no. 3, pp. 511–518, 2004.

[3] N. D. Manring, "Tipping the cylinder block of an axial-piston swash-plate type hydrostatic machine," *Journal of dynamic systems, measurement, and control*, vol. 122, no. 1, pp. 216–221, 2000.

[4] ——, "Friction forces within the cylinder bores of swash-plate type axial-piston pumps and motors," *Journal of dynamic systems, measurement, and control*, vol. 121, no. 3, pp. 531–537, 1999.

[5] J. S. Sartchenko, "Force balance condition of the valve plate and rotor of an axial piston pump," British Hydromechanics Research Association, Tech. Rep. T750, 1950.

[6] N. Franco, "Pump design by force balance," *Hydraulics & Pneumatics*, vol. 14, no. 11, pp. 101–107, 1961.

[7] A. Yamaguchi, "Formation of a fluid film between a valve plate and a cylinder block of piston pumps and motors: 2nd report, a valve plate with hydrostatic pads: heat transfer, combustion, power, thermophysical properties," *JSME international journal*, vol. 30, no. 259, pp. 87–92, 1987.

[8] ——, "Formation of a fluid film between a valve plate and a cylinder block of piston pumps and motors: 1st report, a valve plate with hydrodynamic pads," *Bulletin of JSME*, vol. 29, no. 251, pp. 1494–1498, 1986.

[9] A. Yamaguchi, H. Sekine, S. Shimizu, and S. Ishida, "Bearing/seal characteristics of the film between a valve plate and a cylinder block of axial piston pumps. Effects of fluid types and theoretical discussion," *Journal of Fluid Control*, vol. 20, no. 4, pp. 7–29, May 1990.

[10] H. Merritt, *Hydraulic control systems.* John Wiley & Sons, 1967.

[11] N. D. Manring, R. E. Johnson, and H. P. Cherukuri, "The impact of linear deformations on stationary hydrostatic thrust bearings," *Journal of Tribology*, vol. 124, no. 4, pp. 874–877, 2002.

[12] N. D. Manring, "Valve-plate design for an axial piston pump operating at low displacements," *Journal of mechanical design*, vol. 125, no. 1, pp. 200–205, 2003.

[13] O. Reynolds, "Iv. on the Theory of Lubrication and Its Application to Mr. Beauchamp Towers Experiments, Including an Experimental Determination of the Viscosity of Olive Oil," *Philosophical Transactions of the Royal Society of London*, vol. 177, pp. 157–234, 1886.

[14] M. Pelosi, "An investigation of the fluid-structure interaction of piston/cylinder interface," Ph.D. dissertation, Purdue University, 2012.

[15] H.-J. van der Kolk, "Beitrag zur Bestimmung der Tragfhigkeit des stark verkanteten Gleitlagers Kolben/Zylinder an Axialkolbenpumpen der Schrgscheibenbauart," Ph.D. dissertation, Verlag nicht ermittelbar, 1972.

[16] A. Yamaguchi and Y. Tanioka, "Motion of pistons in piston-type hydraulic machines: 1st. report: theoretical analysis," *Bulletin of JSME*, vol. 19, no. 130, pp. 402–407, 1976.

[17] M. Ivantysynova, "An investigation of viscous flow in lubricating gaps," Ph.D. dissertation, SVST Bratislava, Czechoslovakia, 1983.

[18] Y. Fang and M. Shirakashi, "Mixed lubrication characteristics between the piston and cylinder in hydraulic piston pump-motor," *Journal of tribology*, vol. 117, no. 1, pp. 80–85, 1995.

[19] L. Olems, "Investigations of the temperature behaviour of the piston cylinder assembly in axial piston pumps," *International Journal of Fluid Power*, vol. 1, no. 1, pp. 27–39, 2000.

[20] M. Ivantysynova and C. Huang, "Investigation of the gap flow in displacement machines considering elastohydrodynamic effect," in *Proceedings of the JFPS International Symposium on Fluid Power*, vol. 2002. The Japan Fluid Power System Society, 2002, pp. 219–229.

[21] M. Pelosi and M. Ivantysynova, "A novel thermal model for the piston/cylinder interface of piston machines," in *ASME 2009 Dynamic Systems and Control Conference*. American Society of Mechanical Engineers, 2009, pp. 37–44.

[22] ——, "Heat transfer and thermal elastic deformation analysis on the piston/cylinder interface of axial piston machines," *Journal of tribology*, vol. 134, no. 4, p. 041101, 2012.

[23] M. Zecchi, "A novel fluid structure interaction and thermal model to predict the cylinder block/valve plate interface performance in swash plate type axial piston machines," Ph.D. dissertation, Purdue University, 2013.

[24] U. Wieczorek and M. Ivantysynova, "Computer aided optimization of bearing and sealing gaps in hydrostatic machinesthe simulation tool CASPAR," *International Journal of Fluid Power*, vol. 3, no. 1, pp. 7–20, 2002.

[25] C. Huang, "A new approach to predict the load carrying ability of the gap between valve plate and cylinder block," in *Bath Workshop of Power Transmission and Motion Control PTMC 2003, Bath, UK*, 2003, pp. 225–239.

[26] M. Zecchi and M. Ivantysynova, "A novel fluid structure interaction model for the cylinder block/valve plate interface of axial piston machines," *Proceedings of the IFPE*, 2011.

[27] ——, "A novel approach to predict the cylinder block/valve plate interface performance in swash plate type axial piston machines," in *ASME/Bath Symposium on Fluid Power and Motion Control*, 2012, pp. 13–28.

[28] A. T. Schenk, "Predicting lubrication performance between the slipper and swashplate in axial piston hydraulic machines," Ph.D. dissertation, Purdue University, 2014.

[29] N. A. Shute and D. E. Turnbull, "The losses of hydrostatic slipper bearings under various operating conditions," British Hydromechanics Research Association, Tech. Rep. RR743, Oct. 1962.

[30] ——, "The minimum power loss of hydrostatic slipper berrings," BHRA, Tech. Rep. SP721, 1962.

[31] C. J. Hooke and K. Y. Li, "The lubrication of overclamped slippers in axial piston pumpscentrally loaded behaviour," *Proceedings of the institution of mechanical engineers, part c: journal of mechanical engineering science*, vol. 202, no. 4, pp. 287–293, 1988.

[32] ——, "The lubrication of slippers in axial piston pumps and motorsthe effect of tilting couples," *Proceedings of the institution of mechanical engineers, part c: journal of mechanical engineering science*, vol. 203, no. 5, pp. 343–350, 1989.

[33] A. Schenk, M. Zecchi, and M. Ivantysynova, "Accurate prediction of axial piston machines performance through a thermo-elasto-hydrodynamic simulation model," in *ASME/BATH 2013 Symposium on Fluid Power and Motion Control*. American Society of Mechanical Engineers, 2013, pp. V001T01A034–V001T01A034.

[34] A. Schenk and M. Ivantysynova, "A transient thermoelastohydrodynamic lubrication model for the slipper/swashplate in axial piston machines," *Journal of Tribology*, vol. 137, no. 3, p. 031701, 2015.

[35] K. T. Renius, *Untersuchungen zur Reibung zwischen Kolben und Zylinder bei Schrgscheiben-Axialkolbenmaschinen*. VDI-Verlag, 1974.

[36] R. Lasaar, *Eine Untersuchung zur mikro-und makrogeometrischen Gestaltung der Kolben-, Zylinderbaugruppe von Schrgscheibenmaschinen*. VDI-Verlag, 2003.

[37] R. A. Burton, "Paper 5: The Thermodynamics of a Viscoelastic Film under Shear and Compression," in *Proceedings of the Institution of Mechanical Engineers, Conference Proceedings*, vol. 180. SAGE Publications Sage UK: London, England, 1965, pp. 72–84.

[38] G. Xu and F. Sadeghi, "Thermal EHL analysis of circular contacts with measured surface roughness," *Journal of tribology*, vol. 118, no. 3, pp. 473–482, 1996.

[39] H. Everth, "Konstruktion einer Modellpumpe zur Messung des Druck-und Temperaturfeldes im Spalt zwischen Kolben und Zylinder einer Schragscheiben-Axialkolbenmaschine," Ph.D. dissertation, TUHH, 2003.

[40] L. Shang and M. Ivantysynova, "Advanced heat transfer model for piston/cylinder interface," in *Proceedings of the 11th IFK International Fluid Power Conference*, vol. 1, Aachen, Germany, Mar. 2018, pp. 587–595.

[41] ——, "Thermodynamic analysis on compressible viscous flow and numerical modeling study on piston/cylinder interface in axial piston machine," in *Proceedings of the 10th JFPS International Symposium on Fluid Power*, Fukuoka, Japan, 2017, pp. 475–581.

[42] D. Grnberg, "Prediction of case temperature of axial piston pumps," Master's thesis, Chalmers University of Technology, Sweden, 2011.

[43] M. Zecchi, A. Mehdizadeh, and M. Ivantysynova, "A novel approach to predict the steady state temperature in ports and case of swash plate type axial piston machines," in *13th Scandinavian International Conference on Fluid Power; June 3-5; 2013; Linkping; Sweden*. Linkping University Electronic Press, 2013, pp. 177–187.

[44] L. Shang and M. Ivantysynova, "Port and case flow temperature prediction for axial piston machines," *International Journal of Fluid Power*, vol. 16, no. 1, pp. 35–51, 2015.

[45] ——, "An investigation of design parameters influencing the fluid film behavior in scaled cylinder block/valve plate interface," in *9th FPNI Ph. D. Symposium on Fluid Power*. American Society of Mechanical Engineers, 2016, pp. V001T01A027–V001T01A027.

[46] ——, "A path toward effective piston/cylinder interface scaling approach," in *ASME/BATH 2017 Symposium on Fluid Power and Motion Control*. American Society of Mechanical Engineers, 2017, pp. V001T01A072–V001T01A072.

[47] ——, "A temperature adaptive piston design for swash plate type axial piston machines," *International Journal of Fluid Power*, vol. 18, no. 1, pp. 38–48, 2017.

APPENDICES

VITA

VITA

Lizhi Shang was born on March 25th, 1989 in Tianjin, China. He received this B.S. from Huazhong University of science and technology in June 2011. In fall of 2011, he began as a master student in New Jersey Institute of technology. In Summer of 2012, he joined Maha fluid power research center for two months as a visiting student. He officially became a graduate student at Maha fluid power research center at Purdue University since January 2013 under the supervision of Dr. Monika Ivantysynova. His research focus was studying the scaling of axial piston pumps and motors. He successfully defended his Ph.D. in November 2018.